Model Predictive Control for Energy Efficient Cooling and Dehumidification

by

Tea Zakula

Diploma Engineer in Mechanical Engineering
Faculty of Mechanical Engineering and Naval Architecture, University of Zagreb, 2007

Master of Science in Building Technology
Massachusetts Institute of Technology, 2010

Submitted to the Department of Architecture
in Partial Fulfillment of the Requirements for the Degree of

Doctor of Philosophy in Building Technology

at the

Massachusetts Institute of Technology

June, 2013

Signature of Author:

Department of Architecture
May 3rd, 2013

Certified by:

Leslie K. Norford
Professor of Building Technology
Thesis Supervisor

Accepted by:

Takehiko Nagakura
Associate Professor of Design and Computation
Chair of the Department Committee on Graduate Students

Thesis Committee

Leslie K. Norford
Thesis Supervisor
Professor of Building Technology
Department of Architecture
Massachusetts Institute of Technology

Peter R. Armstrong
Associate Professor of Mechanical Engineering
Mechanical Engineering Program
Masdar Institute of Science and Technology

Leon R. Glicksman
Professor of Building Technology
Department of Architecture
Massachusetts Institute of Technology

Model Predictive Control for Energy Efficient Cooling and Dehumidification

by

Tea Zakula

Submitted to the Department of Architecture on May 3rd, 2013
in Partial Fulfillment of the Requirements for the Degree of
Doctor of Philosophy in Building Technology

Abstract

Energy has become a primary concern in countries worldwide, and is a focus of debates on national security, climate change, global economy, and the developing world. With more people in developing countries adopting the lifestyle of western countries as rapidly as possible, limited only by economic means, a tremendous increase in world's energy consumption in the next few decades seems difficult to avoid. The building sector is of particular interest, since it accounts for a large portion of the total energy market: currently in the U.S. forty percent of the total energy and seventy percent of electricity is consumed by residential and commercial buildings. Within commercial buildings, cooling equipment represents the second largest consumer of electricity.

This research analyzes one option for reducing space cooling energy consumption, an advanced cooling system termed low-lift cooling system (LLCS). The system comprises thermally activated building surfaces (TABS) with water running through pipes embedded in a building's construction to serve both as cool storage and as a means of delivering the cooling effect. The LLCS utilizes model predictive control (MPC) algorithm that, based on weather and load predictions, determines the cooling strategy over next 24 hours that minimizes energy consumption. Different objectives, such as minimizing the total cost of electricity, can be achieved by modifying the objective function. Currently there is no commercially or publicly available software that allows the analysis of systems that employ MPC. The first goal of this research was to develop a computer algorithm that can simulate the LLCS performance, but also the performance of other cooling systems that employ MPC. The second goal was to analyze the LLCS performance across different U.S. climates relative to a conventional cooling system and to explore different dehumidification strategies that can be used in combination with the LLCS.

This research significantly advances the knowledge of simulation and performance of the LLCS. The developed MPC algorithm enables a systematic study of primary factors influencing dynamic controls and the savings potential for an individual building. The algorithm is highly modular, enabling easy future expansion, and is sufficiently fast and robust for an implementation real buildings. The results of the analysis suggest that the electricity savings using the LLCS are up to 50% relative to an all-air system under conventional control and up to 23% relative to an all-air system under MPC. The savings were achieved through lower fan and pump transport energy and better utilization of part-load efficiencies inherent in inverter-compressor equipment, a result of the TABS technology and the optimal control.

Thesis Supervisor: Leslie K. Norford
Title: Professor of Building Technology

Acknowledgements

I would like to acknowledge people and organizations that were tremendously helpful in this process. First, I would like to thank MIT Energy Initiative, Masdar Institute of Science and Technology (Abu Dhabi, UAE), Martin Family Society and National Science Foundation for believing in me and in my research. Without your financial support none of this would be possible.

I want to thank my incredible advisor, Professor Norford. Les, you are truly one of the most special people I have ever met in my life. They say the best teacher lets you find your own truth. Thank you for letting me finding my own truth and being there for guidance and support every step of the way. Your technical knowledge and care for your students are attributes I hope to emulate.

Professor Glicksman, I remember vividly sitting in your office before coming to MIT and feeling so honored just by having a chance to meet you. Over the past few years you have influenced my development tremendously, especially as a teacher. That is very special to me and I am very thankful for that.

Professor Armstrong, thank you for allowing me to contribute to the project that was so important to you. Your passion and dedication instilled the same importance in me. Your desire for perfection is priceless and my efforts to not disappoint somebody I have incredible respect for made my work so much more complete and meaningful.

Thanks to my advisor in Croatia, Igor Balen, for being always on my side and helping me when I needed it the most. To the Building Technology group, all of the BT faculty, Kathleen, Ale, Dave, and other lab-mates, thank you for being my family in Boston.

To all of my friends, on both sides of the Atlantic, thank you for being so loving and for accepting me the way I am. Special thanks to my two best friends who I love so much. Ana, you know you are like a sister to me. As far or as close as we are from each other, I always feel we are together. Grga, you are a big reason I came to MIT, something that ended up being the best decision in my life. I am so proud to have such a special friend like you, none of this would be possible without your unconditional support.

At the end, I dedicate this work to my biggest role models in my life, my family. They taught me that life is about fighting for what you believe in, no matter how hard it is, or what other people think. Everything I have achieved in life has been because of their love and support and I could never thank them enough.

Table of Contents

List of Figures

List of Tables

Nomenclature

Symbol	**Description**	**Unit**
D	compressor displacement	m^3
E	energy	J
f	compressor frequency	Hz
h	enthalpy	J/kg
L	latent load	kg$_w/s$
P	power	W
Q	heating or cooling rate	W
T	temperature	°C
V	flow	m^3/s
w	absolute humidity	kg$_w/kg_{air}$
y	condenser area percentage	-
ρ	density	kg/m^3

Subscripts	
adj	adjacent room
avg	average
c	condensing
conv	convective
e	evaporating
i	internal
inf	infiltration
lg	refers to change from saturated liquid to saturated vapor
llim	lower limit
m	measured
max	maximal
o	operative
opt	optimal
rad	radiative
sc	subcooling region of condenser
ulim	upper limit
vent	ventilation
x	ambient
z	zone

Chapter 1

Introduction

Energy has become a primary concern in countries worldwide and is a focus of debates on national safety, climate change, global economy, developing world, and many more. In addition to global climate change, in the recent decade the concerns have particularly shifted to the energy consumption of developing countries, mainly China and India. As a consequence of very high prices of electricity, energy was historically more of a concern in Europe than in the U.S. With a very similar life standard, the member countries of the European Union have approximately half the energy consumption of the U.S. (Figure 1.1). The building sector accounts for a large portion of the total energy market. In effort to reduce energy consumption, energy efficiency of buildings is slowly being promoted through different policies. In 2002, the EU adopted the Energy Performance of Buildings Directive (EPBD), required to be implemented by all member states by January 2009 (European Parliament, 2002). The Directive set minimum efficiency standards for both residential and commercial buildings. Setting even stricter rules, the amendment to the Directive from 2009 stated that all European Union Member States need to ensure that all buildings built after December 31 2018 are net zero energy buildings, which means that they produce as much energy as they consume on site (European Parliament, 2009). Similar action was proposed by The California Public Utilities Commission, with the plan to achieve net zero energy for all new residential construction by 2020, and for all new commercial construction by 2030 (California Public Utilities Commission, 2007). More on net zero energy buildings and policies can be found in Crawley et al. (2009).

Looking more closely into the U.S. energy market, 40% of the total energy (Figure 1.2) and 70% of electricity is consumed by the building sector (EIA, 2012). Current projections suggest that growing trends in the building sector will continue, and at a somewhat faster rate for commercial than residential buildings (Figure 1.3). From 1980 until today, the electricity consumption in buildings doubled, and it is predicted that buildings will account for 77% in the total electricity consumption in 2035 (DOE). That fact that buildings consume such a large portion of electricity is worrisome considering very low efficiency for electricity generation, where only about 30% of primary energy gets delivered to buildings. On the other hand, it also represents a tremendous opportunity for the building sector to have a positive impact on the renewable energy market, and pollution reduction. By utilizing technologies that convert sun/wind/wave energy directly to electricity without carbon emissions, buildings can have a crucial role in transforming the energy market and reducing carbon emissions.

Numerous manuals and codes give valuable recommendations for an improved building envelope, building air tightness, equipment efficiency, and similar improvements for existing solutions. However, the building industry in general seems very conservative when it comes to implementation of advanced technologies, necessary for the design of low energy buildings and their scaling to a larger market. Commercial buildings are in general dominated by internal loads rather than climate, due to a small surface-to-volume ratio, and high internal loads from people and equipment. Therefore, the building envelope improvements can help to a certain extent, but the majority of energy reduction needs to come through better lightning control and advances in cooling and ventilation technology (Figure 1.4). Talking about net zero energy buildings, the current solution is the use of small-scale renewables (mainly photovoltaics) for on-site production . However, a simple calculation for a typical office building in Boston, with a typical energy consumption, photovoltaic efficiency of 15%, and assuming that the the whole building is covered in photovoltaics, can quickly reveal that only around 25% of the annual electricity can be produced on site. Achieving net zero energy buildings, therefore, seems very difficult for buildings that are among the largest consumers of electricity (Figure 1.5) and it is apparent that the solution can only come through improved energy efficiency.

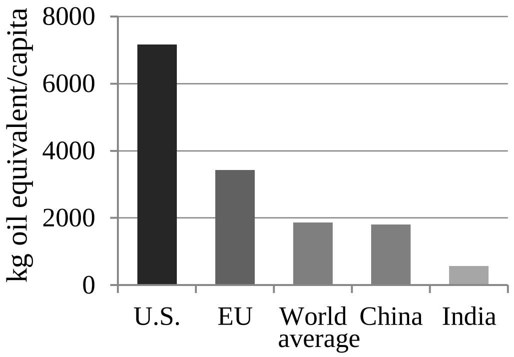

Figure 1.1 – Primary energy use, 2010 (The World Bank),2013

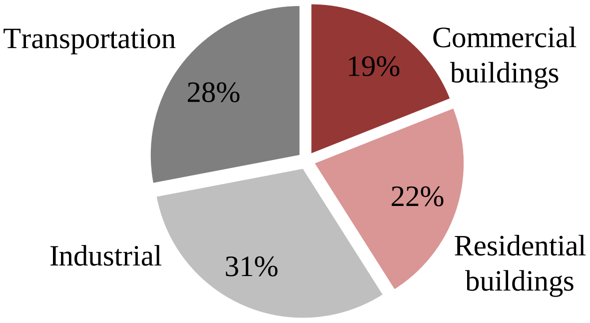

Figure 1.2 – End-use sector shares of total energy consumption, U.S. 2011 (EIA, 2012)

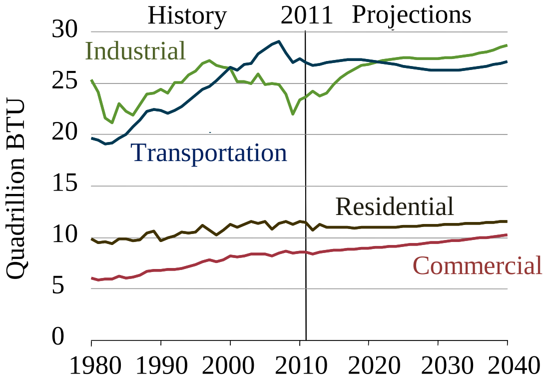

Figure 1.3 – History and projections for delivered energy consumption by sector, U.S. 1980–2040 (EIA, 2013)

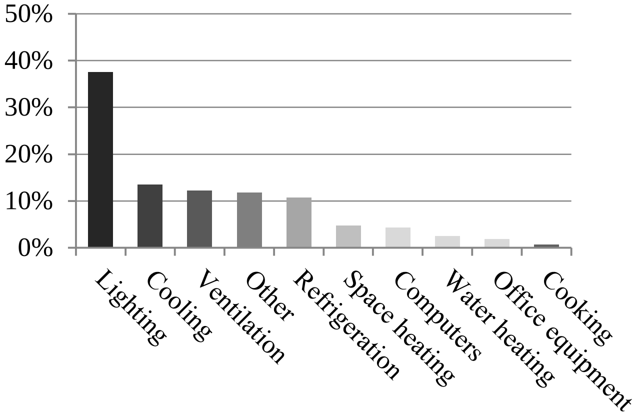

Figure 1.4 – Percentage of commercial buildings electricity consumption by end use, U.S. 2011 (EIA, 2012)

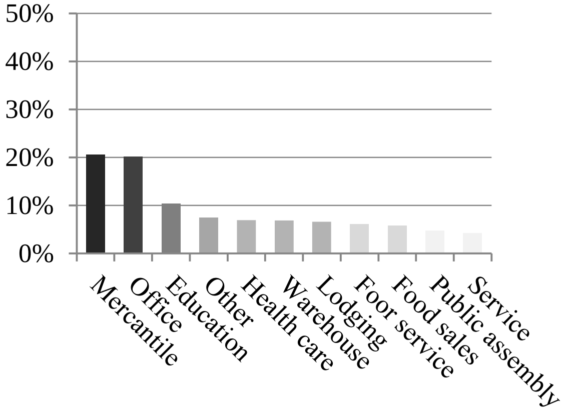

Figure 1.5 – Percentage of commercial buildings electricity consumption by principal building activity, U.S. 2011 (EIA, 2012)

One promising technology for energy reduction is the use of thermally activated building surfaces (TABS), mainly floors and/or ceilings. Sensible heating or cooling is achieved by running hot/cold water through pipes embedded in a building's construction. Compared to conventional systems, TABS systems deliver higher water temperatures for cooling, and lower water temperatures for heating due to large heat exchange areas. This improves the efficiency of a cooling/heating equipment, and feasibility of combining other promising technologies, such as ground source heat pumps or cooling towers. Furthermore, water systems have notably less transport energy and ductwork compared to air systems, due to high thermal capacitance of water (mass × specific heat). There are numerous papers found in the literature describing TABS systems, their energy saving potential, improved thermal comfort, and improved humidity control. Some known challenges are more complex system control and possible condensation issues. Having a large thermal lag, TABS systems cannot respond as quickly as air systems to sudden changes in building thermal needs. Their inertness can also often cause shifts between heating and cooling modes if the control strategy is not carefully designed. Furthermore, possible condensation can occur on cold surfaces in cooling mode when the surface temperature drops below the zone's dew point temperatures. This issue can be resolved by adding a ventilation and dehumidification system and maintaining the TABS surface temperature above the zone's dew point temperature. The additional system could also respond more quickly to sudden changes in internal loads, delivering additional sensible heating/cooling. TABS are more popular in Europe, where high prices of electricity act as the best incentive for energy efficient technologies. Due to relatively mild and dry European climate, they are most often used for heating, and even when used for cooling, the possibility for condensation problems is not as pronounced as in hot and humid climates.

Another promising technology is predictive control, an advanced control algorithm that optimizes the operation of mechanical equipment based on weather and load predictions. The predictive control enables a shift of cooling loads to night time, when the outside temperatures are lower and, therefore, the efficiency of cooling equipment is considerably higher. Furthermore, it can result in lower cooling cost in case of utility rates that favor night operation, as well as reduction in peak loads and equipment size. The shifting can be done through the use of active thermal storage, such as ice or water storage, or the use of building mass acting as passive storage. The use of building mass for passive temperature control is one of the oldest techniques, found in many examples of vernacular architecture worldwide. For example, adobe communities used the building mass to increase building's time constant and mitigate daily temperature swings. Figure 1.6 shows the ancient city of Bam in Iran, which is the biggest structure entirely built from adobe, and Mesa Verde cliff dwellings in Colorado, both on the UNESCO World Heritage Site list. Predictive control is becoming an increasingly popular research topic, demonstrating the benefits for building energy consumption and electricity cost. However, important challenges that still remain are the lack of tools for the system analysis and practical challenges facing real building implementation. Findings in the literature on potential energy and cost savings are highly dependent on a variety of factors, such as the building type, internal load, climate, equipment characteristic, and controls. The use of a computer model would allow for a systematic study of primary factors influencing the dynamic control and saving potential for an individual building. However, currently there are no commercially available tools for this type of analysis, and the modification of the existing building simulation programs has been shown to be challenging, as will be described in Chapter 3. Furthermore, the implementation in real buildings is somewhat inhibited by control complexity compared to conventional systems. There are examples found in the literature on simplified control strategies that would result in a near-optimal control, but those strategies were still obtained by using more detailed computer models.

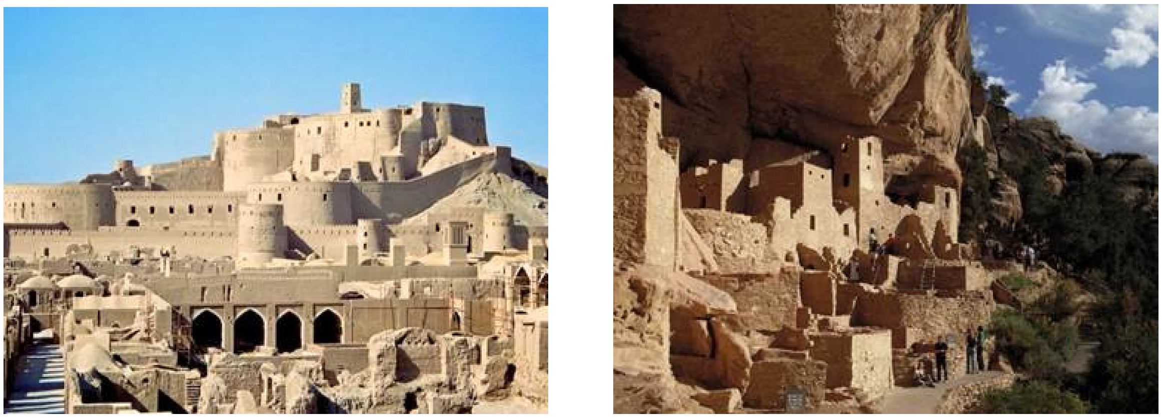
(a) **(b)**

Figure 1.6 – Vernacular architecture – adobe communities (a) ancient city of Bam, Iran (6–4 century BC), (b) Mesa Verde cliff dwellings, Colorado U.S. (6–12 century)

A novel concept of combining TABS, predictive control, thermal storage, and high-efficiency cooling plant was proposed by Jiang et al. (2007) and Armstrong et al. (2009). The combination of lowering the condensing temperature through the use of night precooling and raising the evaporating temperature through the use of TABS and higher water temperatures reduces the the pressure rise across the compressor and is, therefore, termed a low-lift cooling system (LLCS). In simulations with idealized active thermal energy storage, annual cooling system energy savings of up to 75% were found compared to a baseline ASHRAE 90.1-2004 VAV system, as shown in Figure 1.7 (Armstrong et al., 2009). The subsequent analysts confirmed the saving potential across 16 U.S. climates (Katipamula et al., 2010). The market assessment done by the independent agency showed that this system represents an attractive option for the current market, with two possible barriers being the advanced control and the use of active thermal storage. The advanced control of the novel technology would need to be user-friendly and adapted for building facility personnel. The second concern for potential customers was the use of active thermal storage, which in general takes useful space, and has shown in practice to be challenging to control. The cost estimate revealed that office buildings represent ideal first candidates for the implementation of the novel system. Compared to a conventional system, an estimated incremental cost for a large office building was approximately 7.5 $\$/m^2$, while a medium office building had a negative incremental cost of -6 $\$/m^2$. The experimental verification of the energy saving potential was provided by Gayeski et al. (2012) for a typical summer week for Atlanta and Phoenix. The tests were performed in the experimental room at MIT equipped with both the low-lift and baseline configurations. The results for a typical summer week in Atlanta and Phoenix showed sensible cooling savings of 25 and 19% respectively, relative to the standard split-system. The savings potential of the proposed system could be improved even further by advancements in the heat pump industry. A prototype of the chiller for a small temperature lift was recently developed by Wyssen et al. (2010). The prototype included a specially sized expansion valve and the use of a reciprocating compressor to avoid high internal pressure ratios. It was suggested, based on the example of an office building, that for the same operating conditions the new prototype would result in an approximately 6°C smaller lift, and therefore the resulting COP would be 1.6 times higher than the existing chiller.

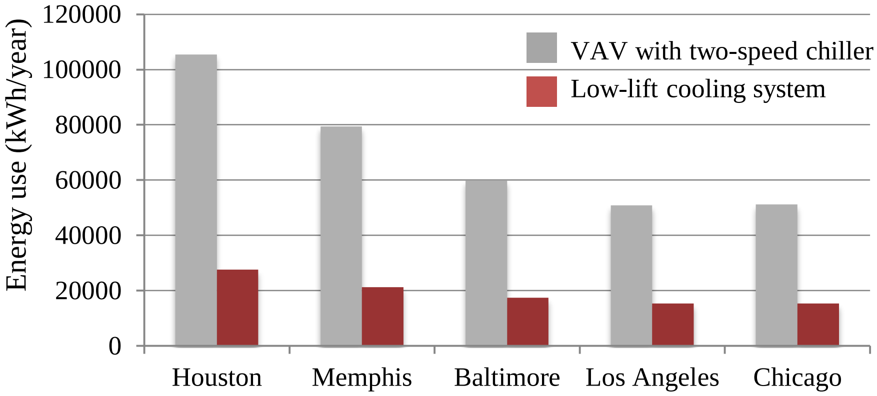

Figure 1.7 – Annual energy use for a typical VAV system and low-lift cooling system for a standard performance building according to Standard ASHRAE 90.1-2004 (Armstrong et al., 2009)

1.1 Thesis objectives and structure

Promising results for the low-lift cooling system shown both using simulations and experimental measurements, as well as great potential for further improvements, were the motivation for a more detailed analysis of the system. The objectives of this thesis are:

- Develop a computer model for the model predictive control of buildings with TABS and/or variable air volume (VAV) systems. The model should enable systematic study of primary factors influencing the dynamic control and savings potential for an individual building, such as building thermal mass, TABS pipe spacing, temperature limits, and control. The model should also be highly modular for future expansion to other promising technologies (e.g. cooling tower or ground heat exchanger), and sufficiently fast and robust for implementation in real buildings.
- Develop a model for the heat pump static optimization, which allows for detailed analysis of the heat pump performance and possible performance enhancements. The optimization should be implemented in the model predictive control (MPC) algorithm, but decoupled from the building optimization so it does not compromise computational speed. Since the main consumer of energy for cooling is a heat pump, these result will have considerable impact on predictive controller decisions and energy savings.
- Develop a model that captures building thermal and hygric response with sufficient accuracy. The model should be able to predict building loads, humidity and temperatures, primarily air temperature, operative temperature, floor temperature, and water return temperature.
- Analyze dehumidification and ventilation strategies that could be used in combination with the proposed energy efficient cooling system. All strategies should be analyzed for different climates and latent loads for better understanding of their impact on possible energy savings.
- Analyze potential savings of the proposed cooling system across different climates, with and without dehumidification. Also, analyze both VAV and TABS system with and without a predictive

control to determine savings achieved through the use of the TABS system alone and savings achieved through the use of the MPC.

The dissertation has the following structure:

Chapter 2 describes the heat pump static optimization model and results. The grid search optimization function uses the heat pump model that was previously developed from first principles and validated using the experimental measurements. The parameters optimized for the lowest heat pump energy consumption are the evaporator and condenser air flow rates and the amount of subcooling on the condenser. The results of static optimization will be compared against non-optimized values. Furthermore, the model will be used to demonstrate the effect of switching to different refrigerants, as well as to understand the importance of the heat pump external sizing.

Chapter 3 describes a structure and validation of two building models that are implemented in the MPC algorithm. The first model is a simple and fast model used in the optimization function. The second model is a more complex model developed with one of the commercially available building modeling programs. It represents a "virtual" building and gives more accurate post-optimization predictions.

Chapter 4 describes the MPC algorithm developed for a building with TABS and VAV systems. Although three different configurations will be considered, only one will be chosen based on its robustness and computational speed. The objective function is formulated for the lowest energy consumption, taking into account both cooling and transport power. Thermal comfort is ensured by introducing a cost penalty for cases when the controlled temperature is outside the given limits.

Chapter 5 proposes several dehumidification strategies with the goal of improving the performance of the associated heat pump. All strategies will be analyzed in Chapter 6 across different climates, for better understanding of their feasibility and limitations. In addition to a typical ventilation and dehumidification system found in the literature, other strategies include a condenser placed in the supply stream, parallel condensers placed in the supply and exhaust stream, parallel condensers placed in the supply stream and outside, and finally the use of a heat pipe around the cooling coil.

Chapter 6 explains the assumptions used in the analysis of the LLCS and VAV system, and analyzes the system across different climates. To test the model accuracy, the analysis is first performed for sensible cooling only and compared with the experimental measurements for Atlanta and Phoenix done by Gayeski et al. (2012). Next, the influence of changes in the pipe spacing and heat pump optimization on the system performance is analyzed. Finally, the analysis includes ventilation and dehumidification needs. Both the VAV system and the LLCS system are tested with and without MPC for better understanding of how much energy saving comes thought the use of TABS and how much through the use of precooling.

Chapter 7 gives an overview of the original contributions, concluding remarks regarding the system analysis and possibilities for future research.

Chapter 2

Heat pump static optimization

The heat pump is the main consumer of energy in the cooling systems and will, therefore, significantly influence the performance of the combined system analyzed in Chapter 6. As a part of the model predictive control, it is desirable to use optimized plant-specific control laws to match compressor, fan and pump speeds to required capacity. This process is known in the HVAC literature as static optimization (ASHRAE,2011, Chapter 42). Although heat pump performance can be characterized by the use of engineering models (Gayeski et al., 2011; Verhelst et al., 2012), heat pump manufacturers data are often only available for a limited range of operating conditions and capacity. This makes it nearly impossible to analyze systems that operate outside those conditions or systems that are still commercially unavailable. The objective here is to use optimization to better understand the extent to which heat pump design and control improvements can impact the annual energy use of advanced cooling systems. This chapter is based on the paper by Zakula et al. (2012).

2.1 Literature review

To perform static optimization, a heat pump model that is accurate, yet computationally inexpensive, is required. The most detailed physics-based heat pump model found in the static optimization literature is that developed by Armstrong (Jiang et al., 2007; Armstrong et al., 2009). The two optimization variables were the evaporating and condensing temperatures, which were then related to the optimal evaporator fan, condenser fan and compressor speeds. The model assumed constant evaporating and condensing temperatures without evaporator superheating, condenser subcooling, or heat pump pressure drops. It also assumed constant conductance (U-value) for the evaporator and condenser, independent of refrigerant and air/water flow rates. Zakula et al. (2011) showed that even neglecting pressure drops can lead to serious errors in power consumption predictions and, therefore, this model would need to be extended for more accurate performance predictions. There are numerous physical models found in the literature that do not perform optimization, but do calculate steady state heat pump performance and, hence, could potentially be adopted for optimization purposes. Probably the best known and most widely used steady-state heat pump model today, developed from Ellison's model (Ellison and Creswick, 1978), is the DOE/ORNL model (Rice, 2006). However, the models found in literature vary from complex models that are computationally expensive and require a large number of input parameters, to models that are similar to Armstrong's model, in that they are relatively simple and fast, but do not take into account certain important phenomena. A detail literature review on heat pump modeling is given in Zakula (2010).

Though they do not describe the optimization of a heat pump's performance, related works on the optimization of large chiller plants can be found in the literature. Lau et al. (1985) developed a TRNSYS (Transient System Simulation Program, Klein et al. 2010) model to analyze different control strategies for an existing chiller plant with four centrifugal chillers, a cooling tower and chilled water tanks. For a given cooling load and wet-bulb temperature, the cooling tower fan speed, condenser pump flow and number of operating chillers were optimized for minimal power consumption. The power consumption of each chiller was characterized as a function of the cooling load, leaving chilled water temperature and leaving condenser water temperature using curve fits to manufacturer's data.

Braun et al. (1987b) investigated the performance and optimal control of a large chiller plant equipped with a cooling tower. A simplified model was used to find near-optimal control with the cooling tower airflow and condenser water flow rates as the control variables. For an individual chiller, measured data from the existing plant were fit to curves that define the chiller power as a function of the cooling load and temperature difference between the leaving condenser and chilled water flows. In subsequent work (Braun et al., 1989), the system was extended to include the chilled water loop and the air handlers with the five independent control variables of supply air set point temperature, chilled water set point temperature, cooling tower airflow, condenser water flow and the number of operating chillers. Braun's more recent work on chiller plant optimization (Braun, 2007) analyzed near-optimal control strategies for a hybrid cooling plant powered by electricity and natural gas. The optimization objective function was the operating cost, which included the electrical and gas energy cost, electrical demand cost, and maintenance cost.

For a given cooling load, return air (zone) temperature, wet bulb temperature and state of charge of thermal storage, the model of King and Potter (1998) optimized chilled-water and supply-air temperature set points for the lowest system power consumption, including the chiller, pumps, cooling-tower fan and supply- and return-air fans. Similar to the previous chiller plant optimization models, performance of an individual chiller was captured using curve fits to manufacturers data.

Jiang and Reddy (2007) developed a general methodology for optimization of HVAC plants and showed its application to a cooling plant that consists of three chillers (one was an absorption chiller) and three variable-speed cooling towers. Semi-empirical Gordon-Ng and effectiveness-NTU models were used to represent chillers and cooling towers. Given total cooling load and required supply temperature and flow rate, the load allocated to each chiller and cooling tower outlet water temperature of each chiller were used as optimization variables.

2.2 Model description

Optimization is performed using the steady state heat pump model developed by Zakula et al. (2011) that can simulate the performance of different heat pump types, such as air-to-air heat pumps and air- and water-cooled chillers. Two evaporator sub-models that describe finned-tube air-to-refrigerant and brazed-plate water-to-refrigerant heat exchangers with defined geometry are modeled using the heat balance equations and ε-NTU method for evaporating and superheating regions. The condenser is modeled in a similar manner, except it consists of desuperheating, condensing and subcooling regions. The heat transfer coefficients are calculated separately for the air/water stream and two-phase and single-phase refrigerant flows. The compressor sub-model calculates the compressor speed, compressor power and discharge temperature for a given mass flow rate, compressor inlet state and outlet pressure. The shaft speed is calculated using a volumetric efficiency model, and the compressor power is calculated as the power required for isentropic work, corrected by the combined efficiency that takes into account losses in the compressor and motor. Coefficients required to calculate volumetric and combined efficiency are found using linear regression to measured data. The compressor outlet temperature is calculated from the compressor heat balance, through which the lubricating oil is assumed to pass in a constant mass fraction. A liquid receiver is assumed to maintain the necessary charge balance, which is not modeled. The heat pump model takes into account pressure drops in refrigerant piping and heat exchangers, the dependence of heat transfer coefficients on flow rates, superheating in the evaporator and desuperheating and subcooling in the condenser.

A modular approach offers the possibility of choosing between different simulation options (level of complexity) and makes the model easy to expand and customize. The model can be used for a single- two- or variable-speed compressor, single compressor, multiple parallel compressors, evaporators or condensers, as well as for different refrigerants. The inverse heat pump model with compressor frequency as an input has also been developed and is used to optimize a heat pump with a two-speed compressor. The two-speed heat pump serves as a base case for annual energy consumption assessments presented later.

The optimization input parameters are a cooling load (Q_e), zone temperature (dry-bulb room's temperature) (T_z) and outside temperature (T_x), and the optimization variables are the evaporator airflow rate (V_e), condenser airflow rate (V_c) and condenser area fraction devoted to subcooling (y_{sc}). If one wants to optimize only one or two variables, the other variables need to be given as an input, e.g. one may want to know the performance impact of the optimal subcooling as opposed to zero subcooling, in which case zero subcooling area is specified and the condenser and evaporator air or water flow rates are optimization variables. All other heat pump operating variables are functions of the optimization variables; in particular, for optimal control, one is mainly interested in the optimal evaporator fan speed, condenser fan speed and compressor speed. One may also be interested in the related refrigerant mass flow rate, evaporating temperatures and pressures, condensing temperatures and pressures, suction and discharge state, subcooling temperature difference and total power consumption.

The optimization algorithm, using the grid search method shown in Figure 2.1, has the advantage of avoiding gradient calculations. Gradient calculations can be computationally expensive and challenging for this type of problem due to nonlinearities and possible convergence issues. Furthermore, if a grid step is appropriately chosen, the grid search is more reliable in finding the global minima than the gradient search method. For each set of conditions (Q_e, T_z, T_x) there are two loops, the outer loop for the optimal subcooling area ratio search, and the inner loop for the optimal flow rates search. The initial 3 by 1 grid (A-grid) and 3 by 3 grid (B-grid) are created for the outer and inner loops respectively. First, the total power consumption is calculated for each of the nine B-grid points and y_{sc}=$y_{sc}\{1\}$. If the lowest power is anywhere on the B-grid boundaries, the grid is extended according to Figure 2.2, and total powers are evaluated for new points. The process continues until the lowest power is in the middle B-grid point (B{2,2}), in which case the algorithm moves to the second A-grid point ($y_{sc}\{2\}$). Similar to the B-grid, if the sub-optimization finishes for all three A-grid points, and the lowest power is on the A-grid boundaries, the A-grid extends until the optimum is at the middle A-grid point (A{2}).

The optimization process is further accelerated with the step adaptation: after finding the optimal variables with a larger step, a new 5 by 5 B-grid is created using a smaller step (half the large step) and $V_{e,opt}$ and $V_{c,opt}$ as the central grid point (Figure 2.3). The point with the lowest power is assigned as the final optimal point (new $V_{e,opt}$ and $V_{c,opt}$). The same grid adaptation is applied for the optimal subcooling.

2.3 Performance map results

For a given cooling rate, outside and zone temperature, the result of the static optimization provides the optimal set of the evaporator and condenser airflow rates, compressor speed and subcooling for which the power consumption will be the lowest. The optimization is performed for a specific heat pump geometry, but the performance of different heat pumps could be optimized by changing geometry of individual components. To show the broad utility and potential benefits of optimization using a component-based model the optimization is performed for several different scenarios:

- air-to-air heat pump with a single compressor (variable-speed rolling-piston compressor) and R410A as a refrigerant
- air-to-air heat pump with two parallel compressors, evaporators and condensers (two variable-speed rolling-piston compressors) and R410A as a refrigerant
- air-to-air heat pump with a single compressor (variable-speed rolling-piston compressor) and ammonia (R717) as a refrigerant
- air-to-air heat pump with a single compressor (variable-speed rolling-piston compressor) and propane (R600) as a refrigerant

The optimization is performed with a 0.025 m^3/s step for the airflows (0–0.3 m^3/s and 0–0.7 m^3/s airflow range for the evaporator and condenser fan respectively) and a 0.001 step for the condenser area ratio devoted to subcooling. For the heat pump with a variable-speed compressor and R410A as a working fluid, the optimal set of evaporator and condenser airflow rates (Figure 2.4), compressor speed (Figure 2.5) and subcooling (Figure 2.6), for which the power consumption for cooling (Figure 2.7) will be the lowest, is shown for the outside temperature $T_x = 30°C$. Figure 2.4 shows that the evaporator and condenser airflows are a strong function of part-load ratios. Furthermore, it was noticed that when optimizing the airflows, the parameter indirectly being optimized is the temperature difference (Figure 2.8). For a given cooling rate, the optimizer tries to maintain the optimal temperature difference on the evaporator (between the evaporating and air temperature) and the condenser (between the condensing and air temperature), regardless of the zone or ambient temperature. From Figure 2.7, which shows the specific power as a function of part-load ratios, it can be seen that the heat pump efficiency increases with lower part-load ratios. For very low part-load ratios the efficiency starts to decrease due to inverter losses that become predominant at low capacities. This raises the question of the appropriate heat pump "external sizing," since with modest oversizing, the heat pump will run at higher efficiencies. However, because there is a cost penalty associated with a size increase, both size and initial cost need to be

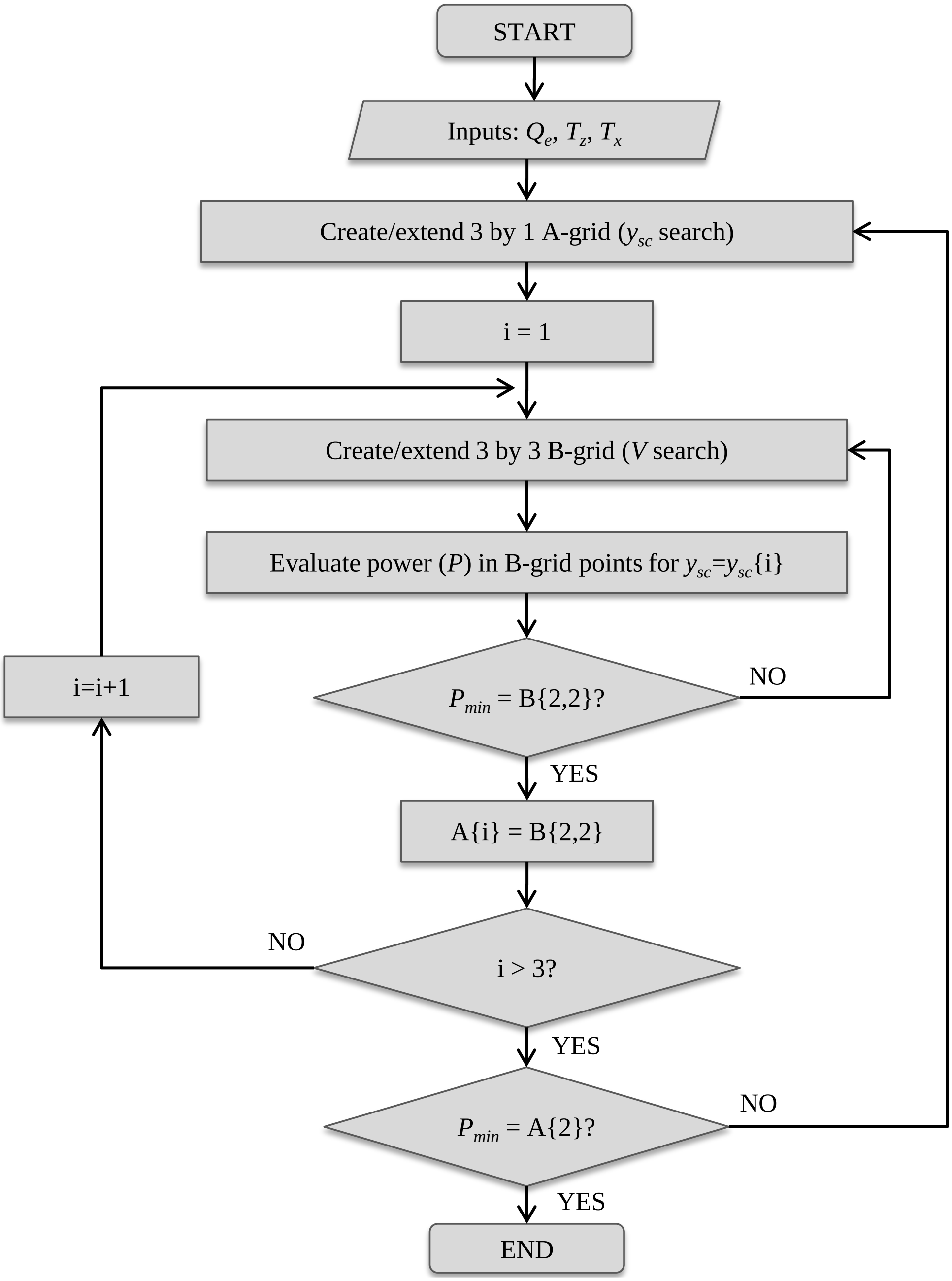

Figure 2.1 – Flow chart for grid search optimization algorithm

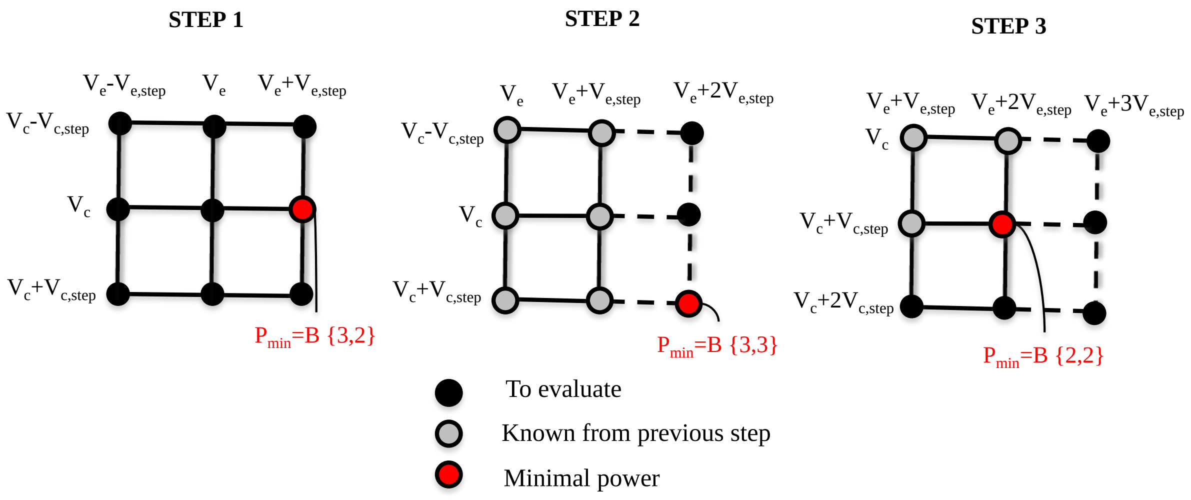

Figure 2.2 – Search loop for the optimal airflows (B-grid)

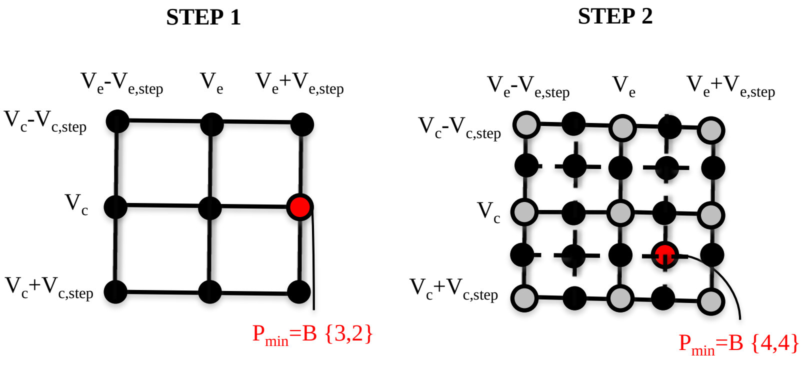

Figure 2.3 – Grid search step adaptation

carefully balanced. The optimal "external sizing" for the lowest energy consumption is discussed later in the chapter. Besides "external sizing," which refers to selecting a heat pump capacity appropriate for the load, another interesting topic to be addressed is "internal sizing:" the sizing of each heat pump component, primarily the evaporator, condenser and compressor. Although not included as a part of this analysis, the presented heat pump optimization algorithm could be extended to the component-sizing problem given a joint distribution of cooling load and operating conditions.

The optimal results are presented here over a wide range of loads (0.1–1 part-load ratio) and temperature differences (0–30°C difference between the zone and ambient). Although Figure 2.4 indicates nearly linear trends for the evaporator and condenser airflows, it can be seen from Figure 2.9 that the same is not true for the optimal airflow-to-compressor-frequency ratio. Similar to optimal airflows, Figure 2.10 shows a strong dependence of the optimal subcooling on the part-load ratio. Finally, it can be seen from Figure 2.11 that the optimal specific power is almost solely a function of a part-load ratio and (for moderate range of evaporating temperature) of temperature differences between the zone and outside. This is in agreement with the study done by Braun et al. (1987a), which concluded that the chiller power consumption was primarily a function of cooling load and the temperature difference between the leaving condenser and chilled water streams. It is important to point out that the optimal evaporator airflows at high part-load ratios are significantly higher than the maximum feasible for the specific heat pump (the airflow rate at the maximum evaporator fan speed was about 0.15 m^3/s for the real heat pump). Because manufacturers primarily optimize this type of a heat pump for simultaneous sensible cooling and dehumidification, in which the heat pump would run with much lower evaporator fan speeds, their use for only sensible cooling results in fan speeds that are far from optimal. The consequence of this for the total energy consumption is described later in an example.

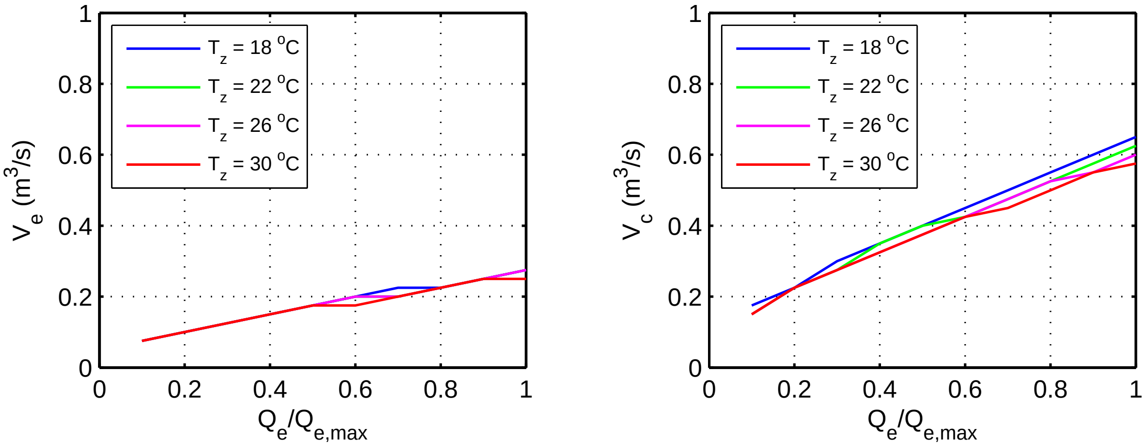

(a) **(b)**

Figure 2.4 – Optimal (a) evaporator and (b) condenser airflow as a function of part-load ratio and zone temperature for outside temperature T_x = 30°C

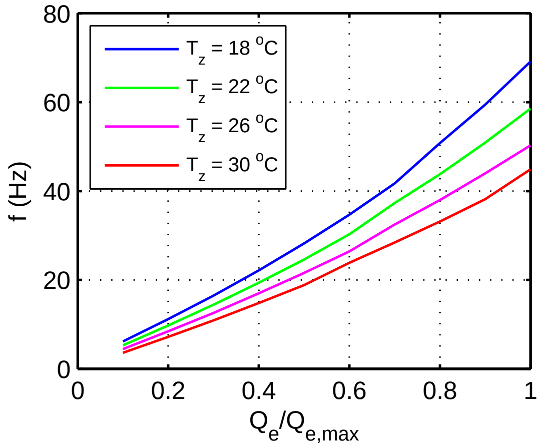

Figure 2.5 – Optimal compressor frequency as a function of part-load ratio and zone temperature for outside temperature $T_x = 30°C$

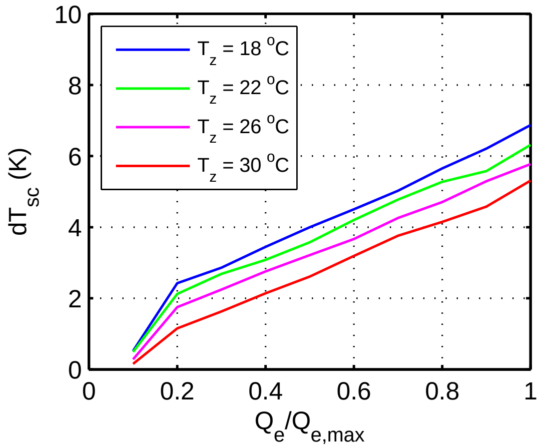

Figure 2.6 – Optimal subcooling as a function of part-load ratio and zone temperature for outside temperature for $T_x = 30°C$

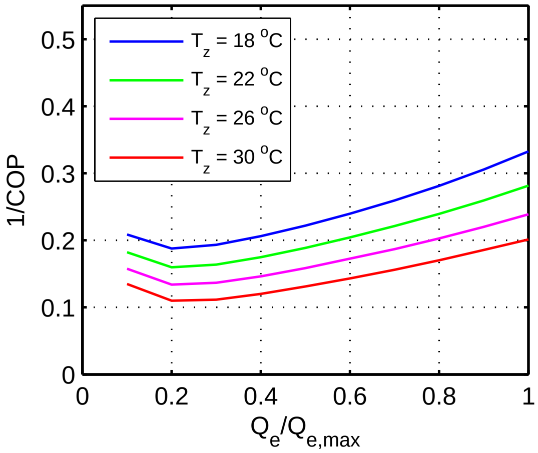

Figure 2.7 – Specific power as a function of part-load ratio and zone temperature for outside temperature for T_x = 30°C

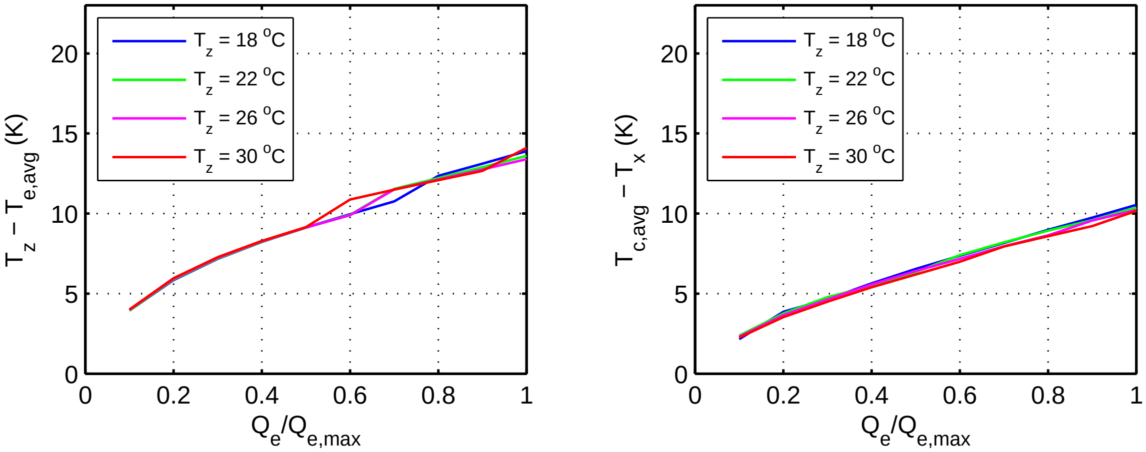

(a) **(b)**

Figure 2.8 – Optimal (a) zone and evaporating temperature difference, and (b) condensing and ambient temperature difference as a function of part-load ratio and zone temperature for outside temperature for T_x = 30°C

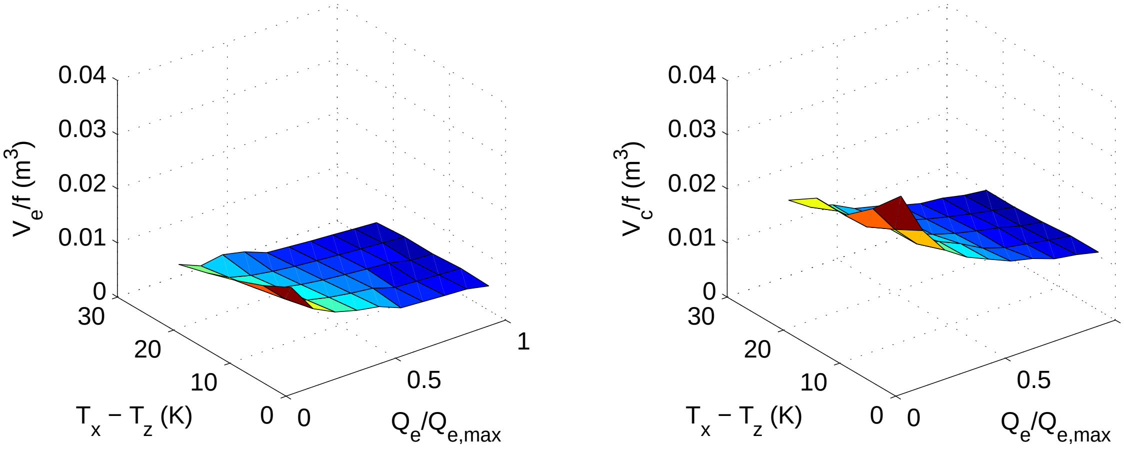

(a) **(b)**

Figure 2.9 – Optimal (a) evaporator and (b) condenser airflow-to-compressor-frequency ratio over a wide range of conditions and loads

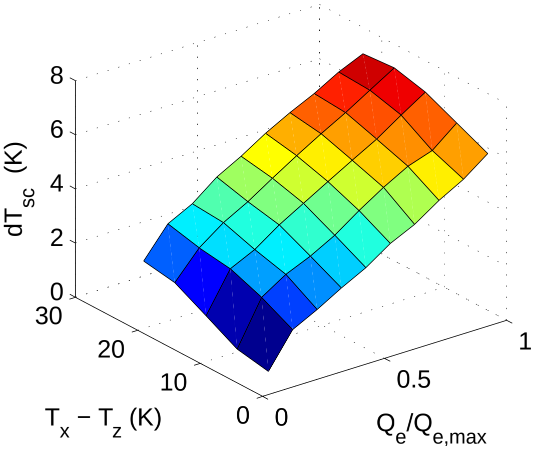

Figure 2.10 – Optimal subcooling over a wide range of conditions and loads

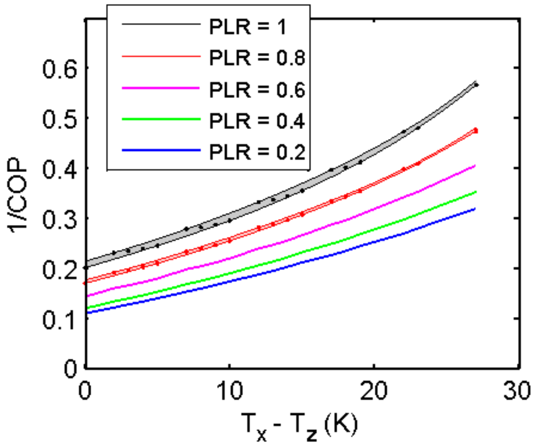

Figure 2.11 – Specific power over a wide range of conditions and loads

2.3.1 Effect of optimization

Subcooling has been used as one of the optimization variables, considering that some heat pump manufacturers already do control subcooling by placing an additional valve between the condenser and liquid receiver. The impact of optimal subcooling with respect to zero subcooling is assessed. Figure 2.12a shows that the COP differences, although relatively small, increase for higher part-load ratios and temperature differences. As a result, the average annual COP of a system that operates at lower part-load ratios would be much less influenced by non-optimized subcooling compared to prevailing systems that deliver most of their annual cooling effect at high part-load ratios. The COP relative differences in Figure 2.12a are calculated as:

$$COP\ relative\ difference = \frac{(COP_{optimized} - COP_{zero\ subcooling})}{COP_{optimized}} \times 100 \tag{2.1}$$

An additional analysis was done to assess the impact of the optimized airflows with respect to fixed airflows. Fixed airflows were set to the maximum feasible for the specific heat pump (0.15 m^3/s and 0.77 m^3/s for the evaporator and condenser fan respectively), and the subcooling was set to zero. The results (Figure 2.12b) show significant differences in the specific power between the optimal and non-optimal cases. The coordination between fan and compressor speeds influences evaporating and condensing temperatures and the compressor power, which accounted for approximately 80% of the total heat pump electricity consumption. This leads to the conclusion that optimizing the airflows plays a significant role in the heat pump performance, and that heat pumps optimized for simultaneous sensible cooling and dehumidification can significantly underperform when used for sensible cooling only. The COP relative differences in Figure 2.12b are calculated as:

$$COP\ relative\ difference = \frac{(COP_{optimized} - COP_{non-optimized})}{COP_{optimized}} \times 100 \tag{2.2}$$

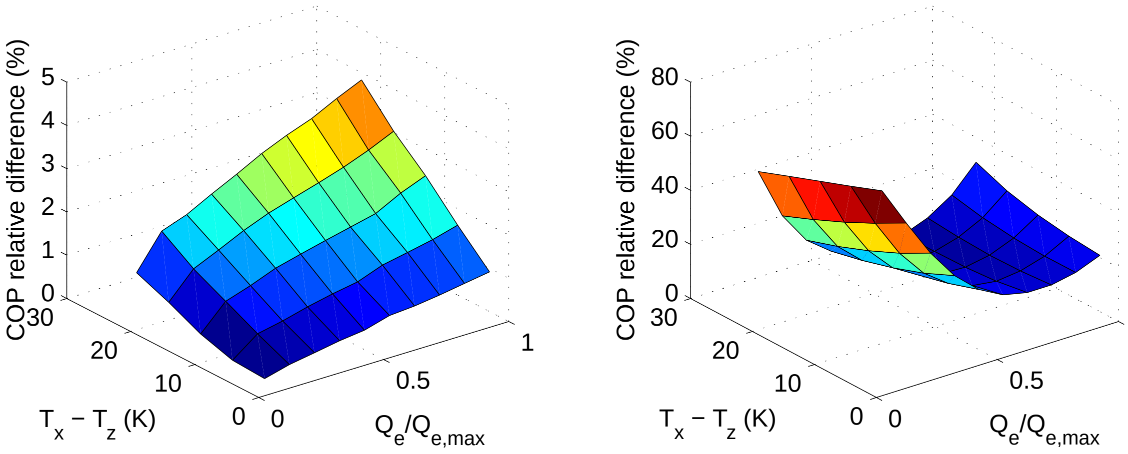

(a) **(b)**

Figure 2.12 – COP relative difference for (a) optimal versus zero subcooling case and (b) optimal versus fixed air flow and zero subcooling case, all for zone temperature T_z = 22°C

2.3.2 Effect of parallel compressors

It can be seen in Figure 2.7 that due to inverter losses, the specific power increases for part-load ratios less than 0.2. The inverter losses account for a small portion of the total power at higher part-load ratios, but become more important as the cooling load decreases. Recently, manufacturers have started to design heat pumps with two, rather than one, variable-speed compressors, which can help to avoid high inverter losses at lower part-load ratios and result in better overall heat pump performance. This case has been analyzed by optimizing the heat pump with 2X scaling of evaporators, condensers and piping, and assuming two variable-speed rolling-piston compressors. The optimization algorithm tests both cases and decides if it is more efficient to run both or just one of the compressors. The results of the analysis (Figure 2.13) show that the heat pump design with two parallel compressors can improve the performance at low part-load ratios by running only one of the two inverter-compressor subsystems.

2.3.3 Effect of refrigerant economizer mode

When the outside temperature is lower than the zone temperature, a heat pump can run in an economizer mode, in which only the evaporator and condenser fans are running, and the compressor is turned off. In some cases liquid may flow from the condenser to evaporator by gravity while in others the flow may be assisted by a small efficient hermetic pump (NTDP, 1994). Having a lower outside temperature, however, does not necessarily imply that running in the economizer mode is more energy efficient. For small temperature differences relative to a part-load ratio, the total sum of the fan and compressor power can be lower than the sum of fan powers when operating in the economizer mode due to high fan speeds. Therefore, without having detailed heat pump maps for both modes (Figure 2.14), it is difficult to develop an appropriate control algorithm that regulates switching between the two. Figure 2.14a illustrates the slope discontinuity where the optimal compressor-mode and economizer-mode performance surfaces intersect, and Figure 2.14b shows how the intersection moves for a different outside temperature. The combined heat pump map is created (Figure 2.15) using the optimization results and selection of the least power mode when $T_x < T_z$.

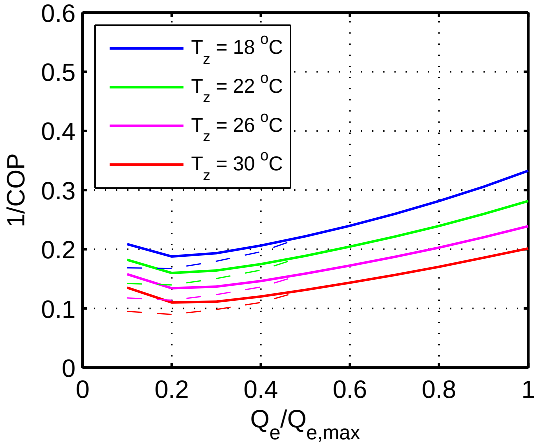

Figure 2.13 – Specific power as a function of part-load ratio for single-compressor machine (solid line) and two-compressor machine with each compressor sized for half $Q_{e,max}$ (dashed line), all for outside temperature T_x = 30°C. Specific power is the same for both machines above 50% part-load.

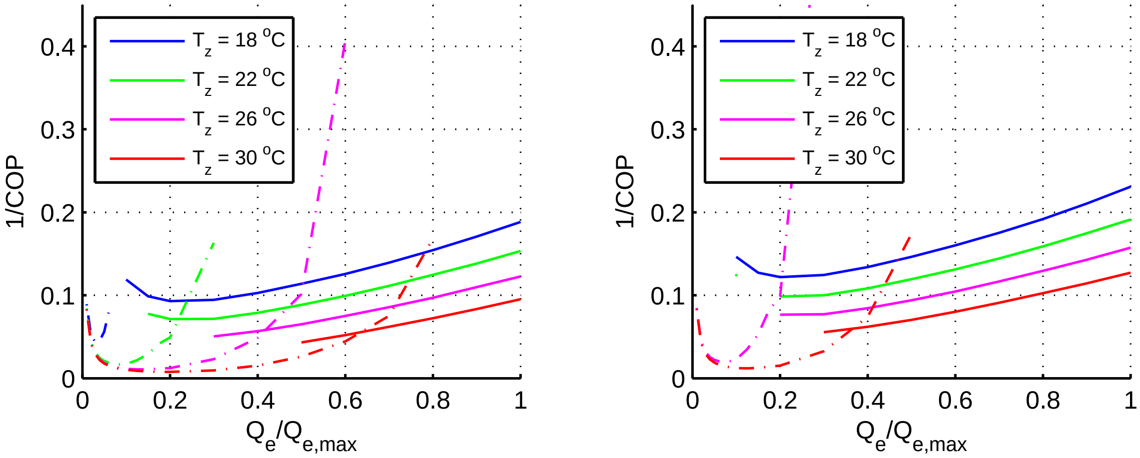

(a) **(b)**

Figure 2.14 – Economizer mode (dashed) and compressor mode (solid) for outside temperature (a) T_x = 15°C and (b) T_x = 20°C

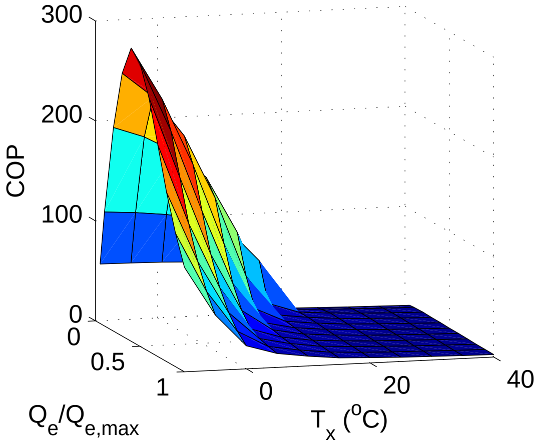

Figure 2.15 – Combined COP (compressor and economizer mode) for zone temperature T_z = 22°C

2.3.4 Effect of refrigerant

The heat pump model and the optimization algorithm can also be used to analyze how changing refrigerants might influence the heat pump performance. When switching to refrigerants other than R410A, the heat pump geometry (primarily the compressor displacement volume and refrigerant piping) was adapted to account for differences in density and heat of vaporization. The compressor displacement volume is scaled using:

$$D_{refrigerant} = D_{R410A} \times \frac{\rho_{R410A}}{\rho_{refrigerant}} \frac{h_{lg,410A}}{h_{lg,refrigerant}} \tag{2.3}$$

The largest pressure drop in the evaporator that corresponds to 4°C drop in the saturation temperature (at T_z = 18°C T_x = 45°C and $Q_e = Q_{e,max}$) for R410A was used to find the appropriate scaling factors for the refrigerant piping. The scaling factors found to give the pressure drops that correspond to the same 4°C drop in the saturation temperature are 0.90 for ammonia, and 1.37 for propane. The relative differences in the COP for different refrigerants are shown in Figure 2.16. The COP relative differences are calculated as:

$$COP\ relative\ difference = \frac{(COP_{refrigerant} - COP_{R410A})}{COP_{R410A}} \times 100 \tag{2.4}$$

The results show higher COP values for propane and ammonia compared to R410A, which is in agreement with the results of a theoretical performance analysis for different refrigerants (ASHRAE, 2009, Chapter 29, Table 9). Differences in the COP of theoretical Rankine cycle are caused by throttling-induced irreversibility and additional work required for the superheated-vapor-horn (Domanski, 1997). For refrigerants operating closer to the critical point, as in the case of R410A, these irreversibilities are higher. Differences due to suction density and enthalpy of vaporization have been largely eliminated by scaling the HX channels, compressor displacement, and interconnect piping.

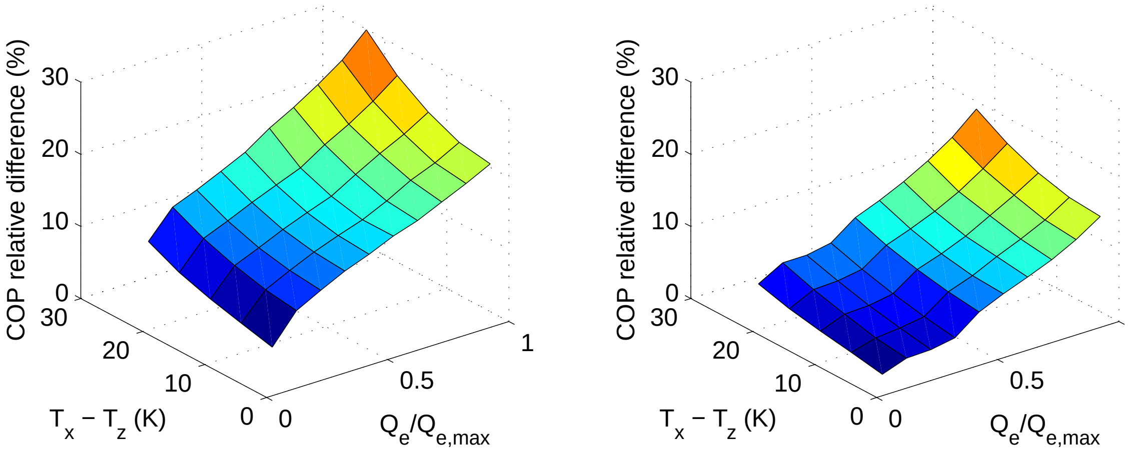

(a) **(b)**

Figure 2.16 – COP relative difference for (a) ammonia versus R410A case and (b) propane versus R410A case, all for T_z = 22°C

2.4 Annual performance results

This section will show how switching to a heat pump with a single two-speed compressor, two parallel compressors, different refrigerants, or a heat pump with non-optimal airflows or non-optimal subcooling can influence the annual energy consumption. Cooling loads used for this analysis are the results of the study done by Armstrong et al. (2009) for a typical office building in Chicago. The load scenarios are presented in terms of full-load-equivalent operating hours (FLEOH), as a function of part-load ratio and outside temperature. In Figure 2.17 load distribution A represents instantaneous loads for a building without thermal energy storage, while load distribution B represents loads that are shifted towards lower part-load ratios and lower outdoor temperatures using thermal energy storage and daily optimized precooling. Load distribution B assumes hydronic radiant cooling, ideal thermal storage, variable-speed chiller and a dedicated outdoor air system for ventilation. Although the shifted load distribution will be affected by the exact performance characteristic of the heat pump or chiller, it is assumed that the distribution presented here is representative of the class of static-optimized machines with high-turndown variable-speed compressors, pumps and fans.

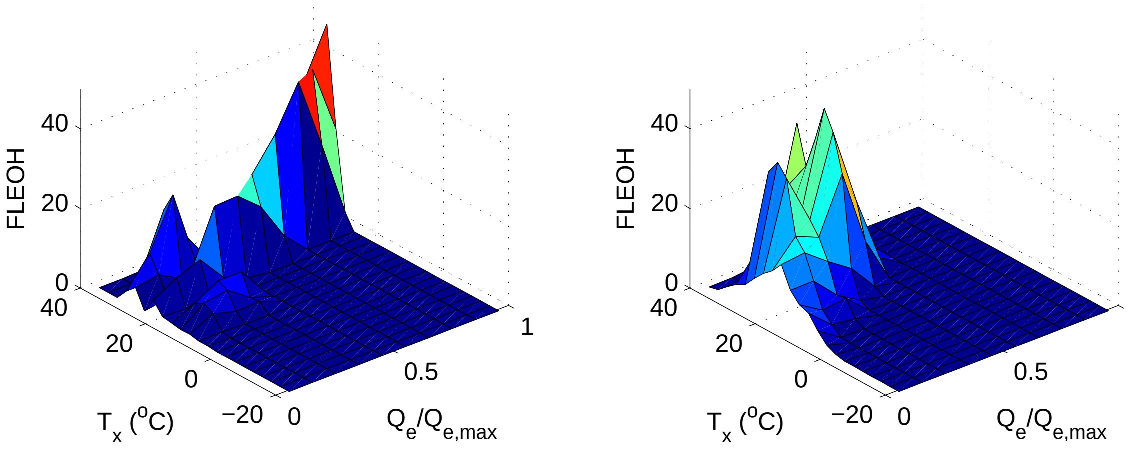

(a) **(b)**

Figure 2.17 – Sensible cooling load distribution for (a) load distribution A (without thermal energy storage) and (b) load distribution B (with thermal energy storage)

The two cooling load scenarios may be convolved with several different heat pump configurations to estimate the influence of heat pump design on the annual energy consumption. Performance maps are created for the following heat pumps:

1. variable-speed compressor heat pump with optimized airflows and subcooling
2. variable-speed compressor heat pump with optimized airflows and zero subcooling
3. variable-speed compressor heat pump with maximum airflows (V_e = 0.15 m^3/s, V_c = 0.77 m^3/s) and zero subcooling
4. two-speed compressor heat pump (assuming two-speed fans)
5. dual variable-speed compressors heat pump with optimized airflows and subcooling

For the heat pump with a two-speed compressor, subcooling is optimized for compressor speeds of $f = 0.5 f_{max}$ and $f = f_{max}$. For this case the fans were also assumed to be two-speed, with airflows set at the optimal values found for the variable-speed heat pump (case 1) at $0.5 Q_{e,max}$ (used at the low-frequency compressor speed) and $Q_{e,max}$ (used at the high-frequency speed). For part-load ratios other than $Q_e = 0.5 Q_{e,max}$ and $Q_e = Q_{e,max}$, it has been assumed that the compressor cycles between $f = 0$, $f = 0.5 f_{max}$, and $f = f_{max}$. The specific power (1/COP) for those cases is calculated using equations given in Armstrong et al. (2009):

$$t_H = 2 \times \frac{Q_e}{Q_{e,max}} - 1 \tag{2.5}$$

where t_H is a high-speed duty fraction.

if $t_H < 0$

$$\frac{1}{COP} = \frac{1}{COP(at\ T_x\ and\ f = 0.5 f_{max})} \tag{2.6}$$

else

$$\frac{1}{COP} = (1 - t_H) \times \frac{1}{COP(at\ T_x\ and\ f = 0.5 f_{max})} + t_H \times \frac{1}{COP(at\ T_x\ and\ f = f_{max})} \tag{2.7}$$

For cases 1 through 5, additional optimization was done for the refrigerant-side economizer mode. Combined heat pump maps, similar to the one in Figure 2.15 (compressor mode and economizer mode), were created using an algorithm that decides which mode uses less power for a given cooling load, zone and outside temperature.

The annual energy consumption is calculated by convolving FLEOH distributions (distribution A or B) with different heat pump performance maps (case 1 – case 5) as follows:

$$E = \sum_i \sum_j FLEOH_{i,j} \times \frac{1}{COP} \times Q_{e,max} \tag{2.8}$$

where i, j is the cell index in which i refers to the $Q_e/Q_{e,max}$ grid and j refers to the T_x-grid. Although FLEOH and COP are in general functions of the outside temperature, zone temperature and part-load ratio, this analysis assumes a fixed zone temperature T_z = 22°C.

Several of the most interesting cases are presented in Table 2.1, and introducing different refrigerants results in additional permutations. The results show that for the systems operating at lower part-load ratios (distribution B), the airflow optimization is considerably more important than subcooling optimization. The annual energy savings for the optimal case compared to the non-optimal case with fixed airflows and zero subcooling were around 50% (Table 2.1, second row). On the other hand, savings were marginally different (around 0.4%) when comparing the optimal case to the case with optimized airflows and zero subcooling (Table 2.1, first row). The results (Table 2.1, third row) also show that a heat pump with two parallel compressors saves a significant amount of energy, especially for systems that operate at lower part-load ratios most of the time (distribution B).

Table 2.1 – Annual energy savings for different cases with R410A

Optimized versus zero subcooling (B1 versus B2)	$(E_{zero,sc} - E_{optimized})/E_{zero,sc}$	0.4 %
Optimized versus non-optimized (B1 versus B3)	$(E_{non-optimized} - E_{optimized})/E_{non-optimized}$	49.6 %
Dual versus single compressor (B1 versus B5)	$(E_{single} - E_{dual})/E_{single}$	11.9%

Results in Table 2.2 show that a variable-speed compressor heat pump (case 1) achieves large energy savings compared to a two-speed compressor heat pump (case 4) whether one is mostly operating at higher (Table 2.2, column 2) or at lower (Table 2.2, column 3) part-load ratios. Armstrong's study assumed a two-speed compressor heat pump for distribution A, and a variable-speed compressor heat pump for distribution B. The results of this analysis (Table 2.2, column 4) show savings (around 20%) achieved by operating the heat pump at lower part-load ratios in addition to the variable-speed compressor savings (around 30%). However, as shown in Table 2.2, not all heat pumps benefit equally from the use of variable-speed compressor, or the operation at lower part-load ratios. For a better understanding of the heat pump power consumption when switching to different refrigerants (Table 2.3) the optimization algorithm presented here has shown to be extremely advantageous.

Table 2.2 – Annual energy savings for distribution A and distribution B using two-speed and variable-speed compressor heat pumps

	A1 versus A4 $(E_{A4} - E_{A1})/E_{A4})$	B1 versus B4 $(E_{B4} - E_{B1})/E_{B4})$	B1 versus A4 $(E_{A4} - E_{B1})/E_{A4})$
R410	29.4%	34.5%	48.6%
Ammonia	20.1%	21.6%	38.3%
Propane	7.4%	12.6%	28.6%

Table 2.3 – Annual energy savings for ammonia and propane with respect to R410A

	A1 scenario $(E_{R410A} - E_{refrigerant})/E_{R410A})$	B1 scenario $(E_{R410A} - E_{refrigerant})/E_{R410A})$
Ammonia versus R410A	14.0%	8.7%
Propane versus R410A	7.8%	2.4%

2.4.1 Heat pump sizing

Using the same annual FLEOH distributions (Figure 2.17), an optimization is performed to find the heat pump sizing factor that minimizes energy consumption for scenarios A1 (distribution A with variable-speed heat pump), A4 (distribution A with two-speed heat pump), and B1 (distribution B with variable-speed heat pump). Figure 2.18 shows how different sizing factors influence the total annual energy savings compared to the nominal size system. The gradient-based optimization algorithm in MATLAB determined for this particular case that the optimal sizing factor for the B1 would be 1.17, meaning that in this scenario the heat pump has near-optimal size. Furthermore, the additional energy savings of the optimally sized system were very small compared to the nominally sized system. The heat pumps for A1 and A4 scenarios, on the other hand, are far from the optimum. The optimum that would be achieved with 2.5 sizing factor for A1 and 1.9 sizing factor for A4 would result in energy saving of approximately 20% for A1 and 17% for A4 compared to the nominal size system. The heat pump capital cost is not considered in this analysis. However, the savings for an optimally sized heat pump are achieved almost entirely by increased evaporator and condenser size and hence, its capital cost can be reduced without much impact on annual energy consumption by using a much smaller compressor (ADL, 2000; Levins et al., 1997).

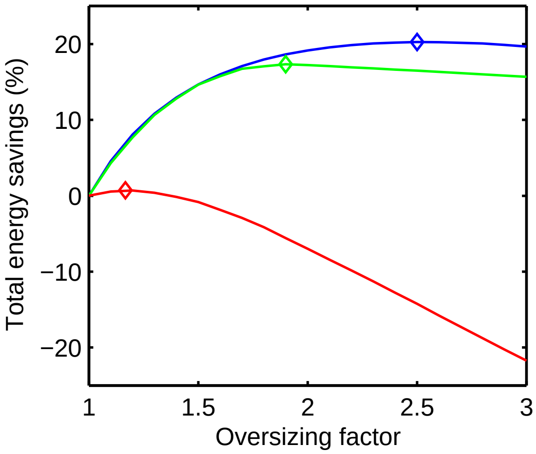

Figure 2.18 – Heat pump optimal sizing for FLEOH distribution A with variable-speed heat pump (blue diamond), distribution A with two-speed heat pump (green square) and distribution B with variable-speed heat pump (red circle)

2.5 Conclusion

This chapter described the adaptive grid search technique used to map the optimal heat pump performance as a function of the capacity and indoor and outdoor temperatures. The grid search algorithm was used to find optimal condenser and evaporator airflows and optimal subcooling at each operating point. It can also be used to optimize the heat pump performance in the economizer mode, when the outside temperature is lower than the water temperature. The optimized data for different heat pumps were used in the model predictive control by fitting polynomials to both compressor-on and economizer mode data, as described in more detail in Chapter 4. The optimization was performed for a specific heat pump geometry, but can also be done for other heat pumps by changing geometry of individual components.

The impact of zero subcooling with respect to optimal subcooling, and fixed airflows with respect to optimal airflows was assessed for the single compressor machines. The results showed that the optimization of airflows has more significance than the subcooling optimization. It was also shown that the the heat pump designed for both sensible and latent cooling can under-perform when used for sensible cooling only, due to a low designed evaporator airflow compared to the optimal. The specific power at optimal fan speeds, as a function of capacity and indoor-outdoor temperature, was compared for R410A-, propane-, and ammonia-charged machines. Finally, the question of optimal sizing of optimally controlled variable-speed heat pumps was explored, and it was shown that modest oversizing is desirable. These findings suggest that the relative sizing of heat pump components (compressor, compressor motor, condenser and evaporator), as well as the sizing of the heat pump itself relative to design load, may benefit from a thorough reassessment of current practice.

Chapter 3

Building Model

When predicting a cooling strategy that results in a cost function reduction (e.g. the price of electricity, or the total electricity consumption) the thermal comfort for the occupants needs to be ensured. Therefore, the important component when developing the model predictive control (MPC) of a building mechanical systems is a model suitable of capturing thermal and hygric response of a building. Besides being accurate and computationally inexpensive, this model should be convenient to use with some of the existing optimization tools.

Many commercially available Building Energy Simulation Programs (BESP) offer more or less detailed simulation of a building's dynamic behavior. EnergyPlus and TRNSYS are two widely used and comprehensive BESPs. However, both programs proved to be challenging for the MPC application, since not all variables can be explicitly initialized at the beginning of a simulation. Before a simulation starts, a user must define the initial zone temperature, also assumed to be the initial wall temperature. The inability to explicitly define different wall initial conditions represents a problem for thermally activated building surfaces (TABS) and night precooling analysis since at the beginning of the next day's optimization the thermal mass temperature can be significantly different than the room temperature.

To overcome the problem with initialization of variables, and also to reduce computational time, the alternative, data-driven (inverse) model was developed for dynamic optimization. TRNSYS model is still used to find appropriate coefficients for the inverse model and to represent a "virtual building". This chapter describes the TRNSYS model and the inverse model of the building zone, both implemented in the MPC algorithm described in Chapter 4. The models have been validated, the TRNSYS model using the experimental measurements and the inverse model using the TRNSYS model predictions. Although the TRNSYS model is more detailed and accurate, the inverse model is significantly faster and, therefore, more suitable for the optimization.

3.1 Literature review

There are numerous commercially available programs for whole building energy simulation such as DOE-2, DesignAdvisor, eQUEST, CAMSOL, SPARK etc. The complete list and overview of a program capabilities can be found in the Building Energy Software Tools Directory (EERE).

The two widely used programs developed to capture building's transient behavior are EnergyPlus (Crawley et al., 1999) and TRNSYS (Transient System Simulation Program, Klein et al. 2010). They are often used for academic research, since they enable detail analysis of complex building systems. Numerous research papers can be found in the literature on their use for variety of building analyses, with TRNSYS more often used in Europe, and EnergyPlus in the U.S.

EnergyPlus is a free, stand-alone simulation program that has its roots in the BLAST and DOE 2 programs. Although the program does not come with a "user friendly" graphical interface, there are many interfaces commercially available (CYPE-Building Services, Demand Response Quick Assessment Tool, DesignBuilder, Easy EnergyPlus, EFEN, AECOsim, Hevacomp, MC4 Suite, SMART ENERGY). The program is not originally designed for a detail analysis of building control systems, but can be linked to programs more suitable for system controls, such as MATLAB or Simulink. The connection can be done through Building Controls Virtual Test Bed (BCVTB) developed by Lawrence Berkeley National Laboratory. BCVTB is a software environment that allows expert users to couple different simulation programs for co-simulation. Some of available options include connections between EnergyPlus, MATLAB, Radiance (ray-tracing software for lighting analysis), and BACnet stack (allows data exchange with BACnet compliant Building Automation Systems).

BCVTB also enables the connection between EnergyPlus and the recently developed simulation environment Modelica (Fritzson et al., 2013). Modelica is an equation-based language with open source library, and is aimed to be used for system analysis in different industries (e.g. building industry or automotive companies). It is developed for large models and control systems, including mechanical, electrical, and hydraulic control. Systems can be described through differential, algebraic, and discrete equations, and no particular variable needs to be solved manually because the Modelica tool solves all equations in parallel.

TRNSYS is another comprehensive program developed to describe building's dynamic behavior. It has a "user friendly" graphical interface called Simulation Studio, and the library that consists of a variety of components, such as a multi-zone building, heat exchangers, pumps, controls etc. The program is very modular, allowing a user to write its own components, or modify the existing ones. To avoid the use of several programs, which would add to complexity and increase computational time, TRNSYS is chosen for the MPC simulation as the program that is highly modular and more suitable for the analysis of building system controls. This chapter will describe in more detail TRNSYS Type 56 for a multi-zone building, which will be implemented in the MPC algorithm. The type is used in combination with the inverse model and optimization function to capture thermal and hygric response of the room with TABS and VAV system.

Due to a lack of programs that combine airflow, heat transfer, and moisture transfer processes in buildings, Annex 41 of the International Energy Agency (IEA) had the goal of stimulating the development of information and analytical tools. Rode and Woloszyn (2007) gave a detailed overview of the IEA project, description of common exercises, advances in simulation programs, and papers published on the topic.

Abadie and Mendes (2006) analyzed both heat and moisture transfer problem with two distinct groups of BESPs and compared them to the known analytical solution. The first, BES 1, was a program that used the response factor method developed by Stephenson and Mitalas (1971). This method is used by both EnergyPlus and TRNSYS building model. The second, BES 2, was a program that used the finite volume method. BES 1 was shown to be 3 times faster than BES 2 for the heat transfer, and 80 times faster for the moisture transfer, even on a very simple problem. For thermal response they both gave relatively accurate predictions when compared to analytical data, while for moisture transfer BES 1 gave good predictions in cases where only a thin external surface layer was affected by the moisture variation of the surrounding air. In a case of sudden changes in indoor humidity, BES 1 underestimated the variations.

Most BESPs are focused on thermal calculations. They analyze moisture transfer using some of the simplified methods that do not account for a change of material properties with variations in temperature and humidity, nor do they account for a change in the moisture buffer effect due to a temperature gradient in a wall. The simplified method often used to describe moisture transfer between the air and solids is the effective moisture penetration depth (EMPD) theory proposed by Kerestecioglu et al. (1990). It assumes that only a very thin layer adjacent to a surface is participating in moisture transfer. The theory is applicable to problems where an inner material layer is not affected by vapor transfer, meaning, for the short periods where the cyclic integral of moisture adsorption and desorption is zero. The predicted results are highly sensitive to the value of the EMPD. Steeman et al. (2009) compared the EMPD model in TRNSYS with the TRNSYS-HAM (heat air moisture) model, in which the heat and mass transfer were coupled using the control volume method and a discretization of a porous material. Material properties depended on a moisture content and were updated each time step, enabling more accurate predictions of indoor humidity. The EMPD model showed a good agreement with the TRNSYS-HAM coupled model in a case of predicted dehumidification loads, while humidification load predictions were significantly lower using the EMPD model. The sensitivity analysis showed that the largest observed differences were caused by the isothermal calculation simplification in the EMPD method, which neglects the additional buffer effect due to a wall temperature gradient.

3.2 TRNSYS building model for MPC

3.2.1 TRNSYS multi-zone building module (Type 56) description

To predict the temperature and humidity response of a building, TRNSYS has been chosen as a comprehensive and modular, yet relatively fast simulation tool. TRNSYS Type 56 for a multi-zone building calculates heat balances for non-geometrical zones, assuming one air node per zone. Walls are modeled using the transfer function method developed by Stephenson and Mitalas (1971), in which the heat rate at each surface is calculated from instantaneous temperatures and the thermal history of a wall as:

$$q = \sum_{t=0}^{n} a^t T_x^t - \sum_{t=0}^{n} b^t T_z^t + \sum_{t=1}^{n} c^t q^t \tag{3.1}$$

Coefficients of the time series a, b and c are calculated at the beginning of a simulation and are dependent on the wall's thermal mass. More hours of the wall's thermal history are used for heavyweight walls compared to lightweight walls, while windows are modeled as a simple resistance, completely neglecting the thermal mass. Abadie and Mendes (2006) noted that the simulation results might be sensitive to a simulation time step, and therefore a sensitivity analysis for each particular case would be beneficial.

The heat transfer through a thermally activated building slab (TABS) (Figure 3.1) is a three-dimensional problem that can be solved using the finite element method (FEM). Because this would be computationally expensive, TRNSYS Type 56 has implemented the alternative modeling method developed by Koschenz et al. (2000). Applying a resistance model (Figure 3.2) a two-dimensional heat transfer problem in x-y axis is reduced to a one-dimensional form. The simplified model showed very good agreement when compared against FEM results.

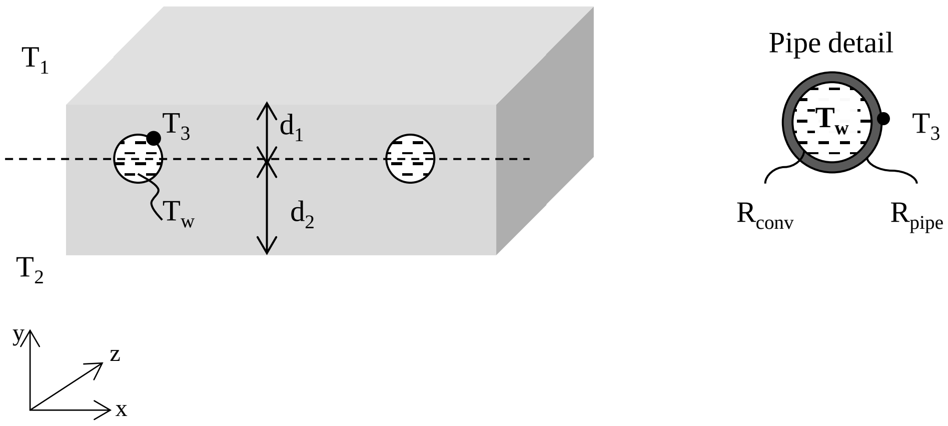

Figure 3.1 – Thermo-active construction element in TRNSYS thermally activated building slab model

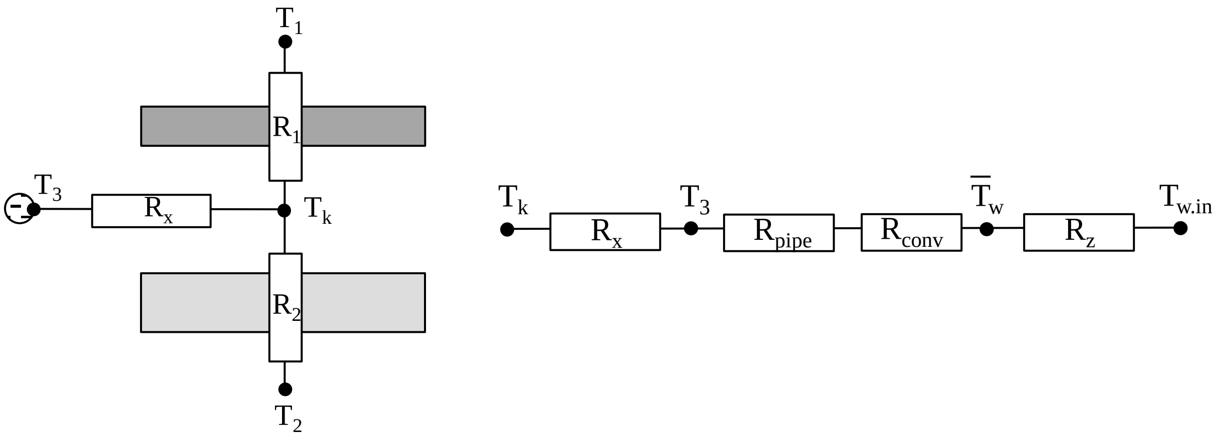

Figure 3.2 – Resistances in TRNSYS thermally activated building slab model

The heat flow from the outside pipe surface to both the air at the upper side of the element (q_1) and to the lower side of the element (q_2) can be then calculated as:

$$q_1 = \phi U_1 (T_3 - T_1) + (1-\phi) \frac{U_1 U_2}{U_1 + U_2} (T_2 - T_1) \tag{3.2}$$

$$q_2 = \phi U_2 (T_3 - T_2) + (1-\phi) \frac{U_1 U_2}{U_1 + U_2} (T_1 - T_2) \tag{3.3}$$

where T_1 is the air temperature on the upper side of the element, T_2 the air temperature on the lower side of the element and T_3 the temperature at the outside surface of the pipe. A pipe configuration is taken into account by the correction factor Φ.

The temperature at the outside pipe surface (T_3) is calculated taking into account conduction through the pipe and convection at the inside surface, where the convective heat transfer coefficient changes depending on the water mass flow rate. To account for water temperature changes in the z-direction, an expression for the z-direction thermal resistance is derived from the heat exchanger model, and combined with the x-y plane thermal resistances in the resistance network (Figure 3.2).

TRNSYS Type 56 offers two simplified models for zone humidity calculations, the effective capacitance model and the buffer storage model. Because the heat and moisture balance are not coupled in TRNSYS, nor a dependence of moisture transfer on the temperature gradient in the wall, nor a variation of material properties with variations in a moisture content can be taken into account. The program does not model moisture transfer from the ambient through the external wall either.

The effective capacitance model uses the first order differential equation for the room air, with the air capacity enlarged for a certain factor (*Ratio*) to account for the buffer effect of walls, furniture, soil and plants:

$$M_{air}Ratio\frac{dw_z}{dt} = m_{inf}\left(w_x - w_z\right) + \sum m_{vent}\left(w_{vent} - w_z\right) + L_{gain} + \sum m_{adj}\left(w_{adj} - w_z\right) \tag{3.4}$$

where M_{air} is the air mass, *Ratio* enlargement factor, w_z zone humidity, m_{inf} and w_x infiltration air flow rate and humidity, m_{vent} and w_{vent} ventilation air flow rate and humidity, L_{gain} internal room latent gains and m_{adj} and w_{adj} air flow rate and humidity from adjacent zones. The enlargement factor represents an increase in moisture storage, taking into account the buffer effect of walls, furniture, soil and plants.

Finding an appropriate enlargement factor represents a difficulty, since the TRNSYS manual only vaguely suggests this number to be between 1 and 10. Furthermore, the literature does not provide reliable and detailed information for this value, nor a comparison of the model against measured data.

A more sophisticated model, the buffer storage model, is based on the effective moisture penetration depth model by Karagiozis and Gu (2004). The wall surface is separated into a surface layer and a deep layer, both characterized with the moisture exchange coefficient β, mass M and gradient of the sorptive isothermal line κ. This introduces an additional term into the first order differential equation (Equation 3.4), plus two additional equations that account for moisture transfer between the layers:

$$M_{air}\frac{dw_z}{dt} = m_{inf}\left(w_x - w_z\right) + \sum m_{vent}\left(w_{vent} - w_z\right) + L_{gain} + \sum m_{adj}\left(w_{adj} - w_z\right) + \beta_{surf}\left(w_{surf} - w_z\right) \tag{3.5}$$

$$M_{surf}\kappa_{surf}f(\varphi, w)\frac{dw_{surf}}{dt} = \beta_{surf}\left(w_z - w_{surf}\right) + \beta_{deep}\left(w_{deep} - w_{surf}\right) \tag{3.6}$$

$$M_{deep}\kappa_{deep}f(\varphi,w)\frac{dw_{deep}}{dt}=\beta_{deep}\left(w_{surf}-w_{deep}\right) \tag{3.7}$$

M_{surf} and M_{deep} are the masses of the surface and deep layer, κ_{surf} and κ_{deep} are the gradients of sorptive isothermal line, $f(\varphi,w)$ is a conversion factor from relative to absolute humidity, β_{surf} and β_{deep} are moisture exchange coefficients and w_{surf}, and w_{deep} correspond to humidity of each layer.

For some common materials the TRNSYS manual gives values for a moisture diffusion resistance, material density and gradient of the sorptive isothermal line, all needed to calculate the moisture exchange coefficient β and the mass M of each layer. However, the difficulty for the buffer storage model is to correctly define the effective moisture penetration depth (EMPD) of each layer, also used to calculate the exchange coefficient β and mass M. The analysis by Abadie and Mendes (2006) showed that a moisture response can be strongly influenced by the EMPD value.

3.2.2 TRNSYS model description

The room modeled as TRNSYS Type 56 and used for the MPC analysis in Chapter 6 is the experimental room shown in Figure 3.3, located at MIT. This room was chosen because experimental measurements for cooling with TABS (Gayeski, 2010) can be used to validate the TRNSYS model. The room is divided into the climate room and test room, both adjacent to the larger laboratory room. The walls are made of two 16 mm gypsum layers, with 110 mm of a polyisocyanurate foam placed in between. There are two double pane windows between the test room and the climate room. The test room floor has PEX pipes embedded into commercially available subfloor system and covered with three layers of concrete pavers. Details on the room construction are given in Appendix A. The pipes can be used for hydronic sensible cooling or heating. The room has an additional indoor unit (split-system) for direct heating, cooling and dehumidification. Both systems are served by the common outdoor unit, which is placed in the climate room so that it captures changes in the chiller efficiency with respect to ambient conditions. The test room is also equipped with lights and heat sources that can simulate internal convective and radiative heat gains for a typical office building. The climate room temperature is controlled by a separate air cooling system, allowing for testing different climate conditions. Detailed parameters used to model the experimental room are given in Appendix B, and the main inputs and outputs for the Type 56 are given in Table 3.1.

The experimental measurements were not performed for the hygric response of the MIT's experimental room. Therefore, parameters used in the TRNSYS buffer storage model for hygric response are those given in the TRNSYS example for a typical office. The office is approximately of the same volume as the MIT's experimental room, with walls made of 12 mm gypsum and 100 mm mineral wool, and the floor and ceiling made of concrete. First 6 mm of gypsum are assumed to act as the surface layer, while the rest of the construction is considered the deep layer. The model validation that can be found in the TRNSYS manual shows good accuracy between the model predictions and 48 hours of measured data.

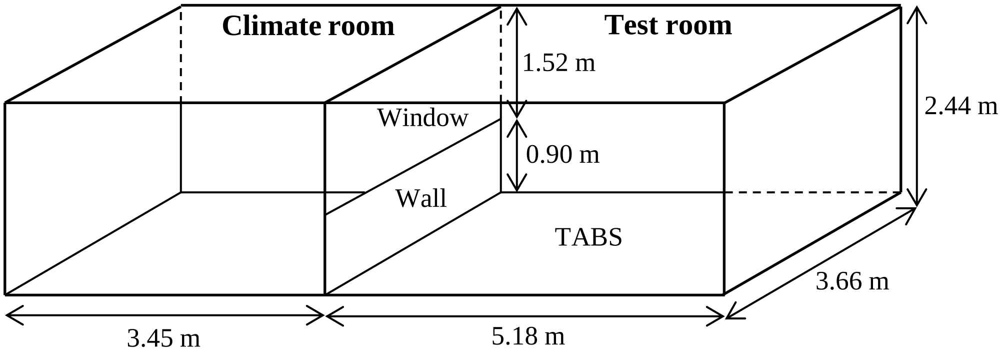

Figure 3.3 – Experimental room setup

Table 3.1 – Inputs and outputs for TRNSYS Type 56 (multi-zone building)

Inputs	Outputs
Climate room temperature	Test room air temperature
Internal sensible and latent gains	Test room operative temperature
Infiltration air ACH, temperature and humidity	Test room air humidity
Ventilation air ACH, temperature and humidity	Test room floor temperature
TABS water mass flow rate	TABS return water temperature
TABS supply water temperature	TABS cooling rate
Direct cooling/heating rate	Condensation flag (0 or 1)

3.2.3 TRNSYS model validation

The experimental measurements for a typical summer week in Atlanta (Gayeski, 2010) are used to validate the TRNSYS model temperature response. Experimentally measured parameters, measurement equipment and measurement tests are described in Gayeski (2010). Experimental measurements that were inputs to the TRNSYS model are the climate room temperature, laboratory room temperature, floor temperature below TABS, internal loads, supply water temperature, and water mass flow rate. The predicted air temperature response (Figure 3.4a), return water temperature (Figure 3.4b), floor temperature (Figure 3.4c) and TABS cooling rate (Figure 3.4d) show good agreement with the measured data. Relative errors in Figure 3.4 are calculated as:

$$Relative\ error = \frac{X_m - X}{\max(X_m) - \min(X_m)} \times 100 \tag{3.8}$$

Beside the zone temperature, the TABS cooling rate is the most important output parameter, since it represents a load on the chiller. It is the output from TRNSYS model, but can also be calculated from the water mass flow rate and supply and return water temperature differences. The water return temperature is another important output that influences the chiller COP and therefore, the cooling power consumption.

Although the time step used in the MPC simulation was 1 hour, additional cases are run in TRNSYS with time steps of 1, 15, and 30 minutes to ensure that the results are not affected by our choice of time step.

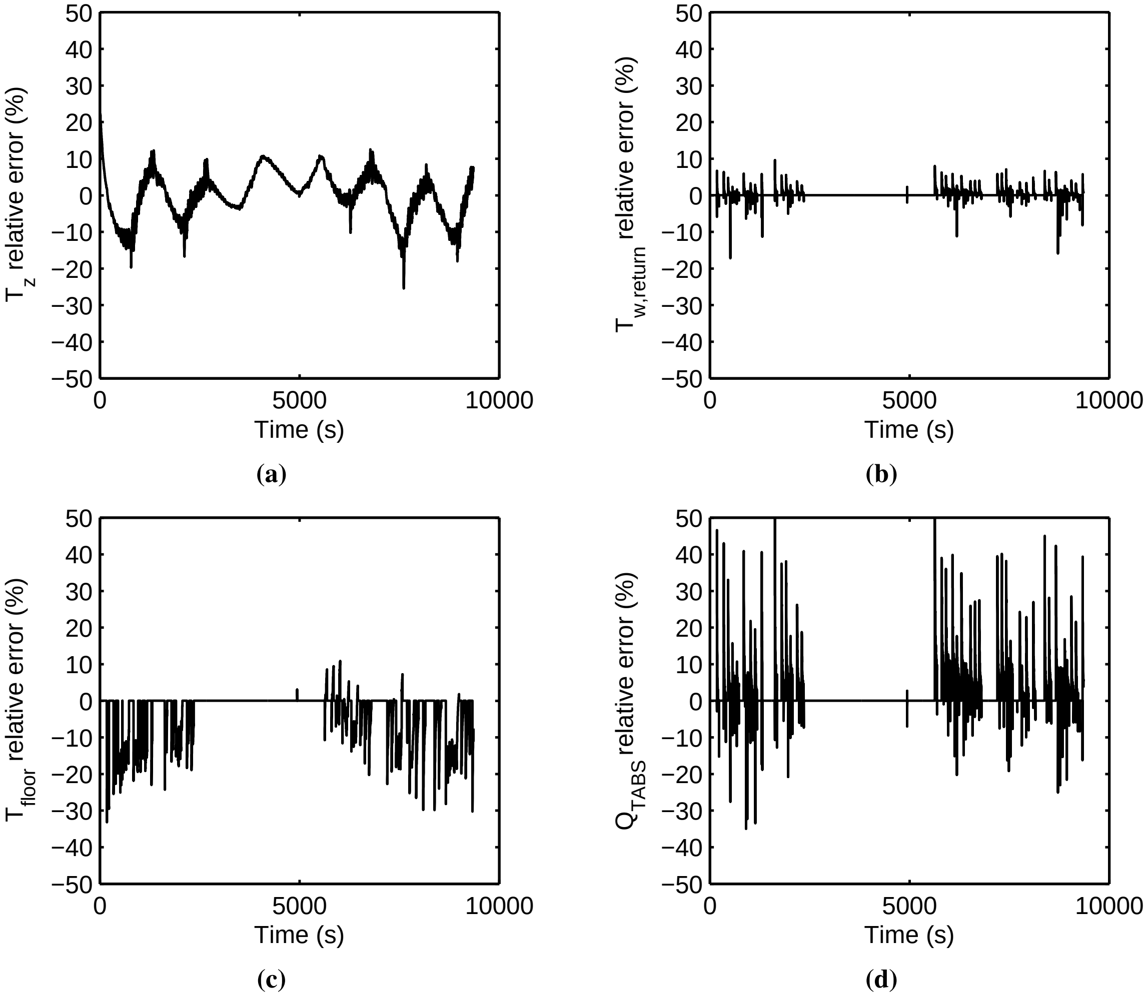

(a) (b) (c) (d)

Figure 3.4 – Comparison between TRNSYS model predictions and experimental measurements of (a) zone temperature, (b) floor temperature, (c) water return temperature, and (d) TABS cooling rate

3.2.4 TRNSYS model sensitivity analysis

The TABS performance strongly depends on the pipe spacing, pipe conductivity, concrete thermal properties, and convective heat transfer coefficient at the floor. Therefore, the sensitivity analysis is performed for the three least known properties: the thermal conductivity of concrete, thermal capacity of concrete, and TABS convective heat transfer coefficient. Each of the parameters was changed from the minimal assumed value, chosen value, and maximal assumed value. The results indicate that the predictions are most strongly influenced by the thermal conductivity of concrete (Table 3.2).

Table 3.2 – Sensitivity analysis for TABS properties

		Relative RMSE			
		$\mathbf{T}_z$	$\mathbf{T}_{w,return}$	$\mathbf{T}_{floor}$	$\mathbf{Q}_{TABS}$
$\mathbf{k}_{concrete}$ **(W/mK)**	0.5	0.2238	0.0087	0.0751	0.0572
	1	0.0512	0.0040	0.0339	0.0256
	1.5	0.1292	0.0029	0.0186	0.0175
$\mathbf{c}_{concrete}$ **(J/kgK)**	800	0.0520	0.0042	0.0304	0.0268
	900	0.0512	0.0040	0.0339	0.0256
	1000	0.0576	0.0039	0.0373	0.0245
$\mathbf{h}_{floor}$ **(W/m^{2}K)**	2	0.0655	0.0027	0.0367	0.0170
	5	0.0512	0.0040	0.0339	0.0256
	8	0.0615	0.0039	0.0361	0.0248

To assess conclusions from Abadie and Mendes (2006) on the importance of the EMPD value, a sensitivity analysis is performed for a surface layer thickness of 3 mm, 6mm (in the TRNSYS example) and 9 mm. Latent loads used as an input for this analysts were a simple step function (Figure 3.5), with the amplitude that corresponds to latent loads from two people. The results (Figure 3.6a) suggest that a layer thickness can have a significant influence on the predictions, and that with a thin surface layer (green), hygric response is notably faster than when more material (blue) is engaged in a surface layer moisture exchange. To make a comparison between the buffer model and simple effective capacitance model, additional cases are run for the effective capacitance model with the enlargement factor 1 and 5. As can be seen in Figure 3.6b, assuming a small enlargement factor significantly underestimates the buffer capacity of a typical room. Furthermore, assuming the enlargement factor of 5 did predict an order of magnitude for changes in the zone's humidity, but showed very different transient trends than the buffer model. When the latent gain goes to zero, the forcing function in the simple effective capacitance model (Equation 3.4) also goes to zero. Since this is not the case with the buffer model forcing function due to the additional buffer term (Equation 3.5), this is the expected behavior.

This analysts confirms the complexity of the moisture transfer problem and the importance of choosing the appropriate model and model parameters. Unfortunately, this topic has not been thoroughly analyzed in the literature and the future work should, therefore, perform experimental measurements on the zone's humidity response.

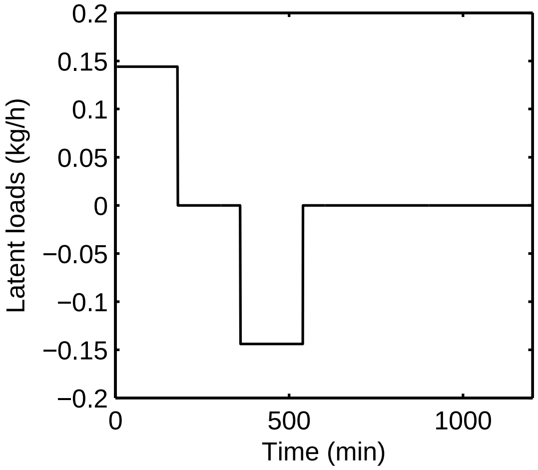

Figure 3.5 – Latent load input for TRNSYS moisture model sensitivity analysis

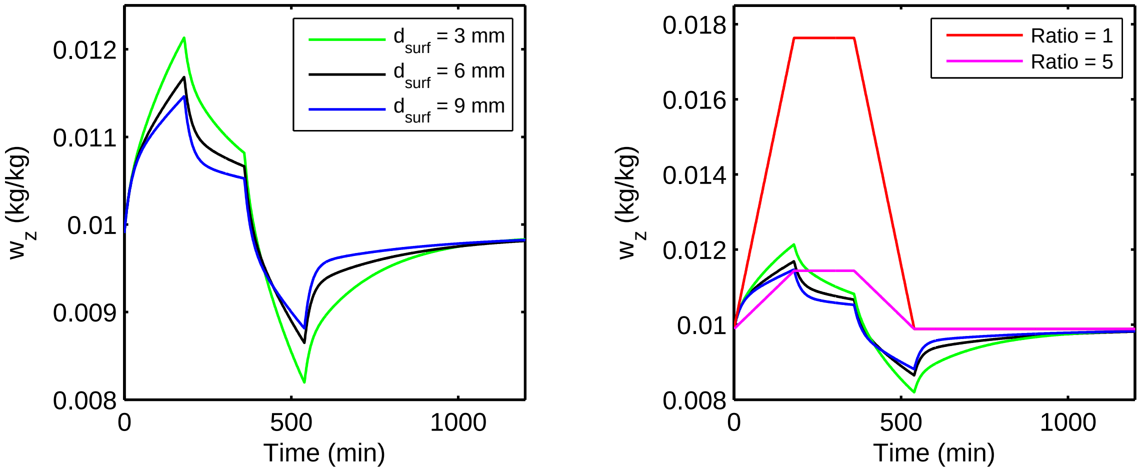

(a) **(b)**

Figure 3.6 – Sensitivity analysis for (a) buffer storage model with different surface layer thicknesses and (b) buffer storage model with different surface layer thicknesses versus effective capacitance model with different room capacity enlargement factor

3.3 TRNSYS-driven inverse model for MPC

Specifying the initial value of variables has shown to be the largest drawback of both TRNSYS and EnergyPlus when used for MPC. Therefore, to predict the thermal and hygric response, and also reduce computational time, the alternative, inverse model was utilized. Seem (1987) showed that the transfer functions used to describe transient changes for individual surfaces can also be used to describe transient changes of the whole room. In the derived comprehensive room transfer function (CRTF), a heat flux for a room was calculated as a weighted sum of past heat rates, and instantaneous and past temperatures. Similarly as for walls, the number of past terms depends on the "heaviness" of the mass, where more past terms are relevant for a heavier construction. Armstrong et al. (2006) showed that the CRTF coefficients for heat flux response are generally not best for temperature response (iCRTF). In their proposed model, a temperature is a weighted sum of past zone temperatures, and current and past ambient temperatures and heat rates:

$$T_z = \sum_{t=1}^{n} a^t T_z^t + \sum_{t=0}^{n} b^t T_x^t + \sum_{t=0}^{n} c^t q^t \tag{3.9}$$

where the coefficients a, b and c must satisfy the steady state equation:

$$q = UA\,(T_x - T_z) \tag{3.10}$$

of a transformed form:

$$q^t \sum_{t=0}^{n} c^t = T_z \left(\sum_{t=1}^{n} a^t - 1 \right) + T_x \sum_{t=0}^{n} b^t \tag{3.11}$$

By combining the Equations 3.10 and 3.11:

$$UA \sum_{t=0}^{n} c^t = \sum_{t=0}^{n} b^t \quad and \quad UA \sum_{t=0}^{n} c^t = \left(\sum_{t=1}^{n} a^t - 1 \right) \tag{3.12}$$

Therefore, the constraint for the inverse model coefficients is:

$$1 - \sum_{t=0}^{n} a^t = \sum_{t=0}^{n} b^t \tag{3.13}$$

Gayeski (2010) showed that the inverse model can serve as a fast and reliable implementation of MPC for a real building. He used the linear regression on a few weeks of training data to find the model coefficients, and then used the inverse model to predict room temperatures in the 24-hour-ahead TABS cooling optimization. Gayeski also analyzed the dependence of prediction accuracy on number of past terms for a specific case. He showed that a higher number of terms does not necessarily give better predictions, due to a system noise having a strong effect on parameters of high-order identified models.

3.3.1 Inverse model A – thermal response of a zone with TABS system

The inverse model is chosen as the alternative model to describe the building's thermal response, primarily the zone temperature, operative temperature, floor temperature and water return temperature as:

$$T_z = \sum_{t=1}^{n} a_z^t T_z^t + \sum_{t=0}^{n} b_z^t T_{adj}^t + \sum_{t=0}^{n} c_z^t T_x^t + \sum_{t=0}^{n} d_z^t Q_{TABS}^t + \sum_{t=0}^{n} e_z^t Q_i^t \tag{3.14}$$

$$T_o = \sum_{t=1}^{n} a_o^t T_o^t + \sum_{t=0}^{n} b_o^t T_{adj}^t + \sum_{t=0}^{n} c_o^t T_x^t + \sum_{t=0}^{n} d_o^t Q_{TABS}^t + \sum_{t=0}^{n} e_o^t Q_i^t \tag{3.15}$$

$$T_{floor} = \sum_{t=1}^{n} a_f^t T_{floor}^t + \sum_{t=0}^{n} b_f^t T_{adj}^t + \sum_{t=0}^{n} c_f^t T_x^t + \sum_{t=0}^{n} d_f^t Q_{TABS}^t + \sum_{t=0}^{n} e_f^t Q_i^t \tag{3.16}$$

$$T_{w,return} = \sum_{t=1}^{n} a_w^t T_{w,return}^t + \sum_{t=0}^{n} b_w^t T_{floor}^t + \sum_{t=0}^{n} c_w^t Q_{TABS}^t \tag{3.17}$$

where

$$Q_{TABS} = m_w c_w (T_{w,return} - T_{w,supply}) \tag{3.18}$$

and T_{adj} temperature of adjacent rooms.

The coefficients (a, b, c, d, e) are found from the linear regression on training data created by the TRNSYS model and are given in Appendix C. It was noticed that although only one week of training data was sufficient for a good fit, a careful selection of training data is needed. Two different sets of training data are shown, the first data set (Figure 3.7a) with similar magnitudes of internal loads and cooling rates for each day, and the second data set, in which every day has different ratios between internal loads and cooling rates (Figure 3.7b).

The coefficients calculated from the first data set gave relatively good agreement for a typical summer week operation in Atlanta. However, when the ratio of internal loads to cooling rate was significantly different from the training data, for an example in the case of significantly lower internal loads, the inverse model did not give good predictions compared to TRNSYS.

3.3.2 Validation of inverse model A – thermal response of a zone with TABS system

The TRNSYS predictions for a typical summer week in Atlanta (Figure 3.8a), previously used to validate the TRNSYS model from experimental data, are here used to validate the inverse model. The additional

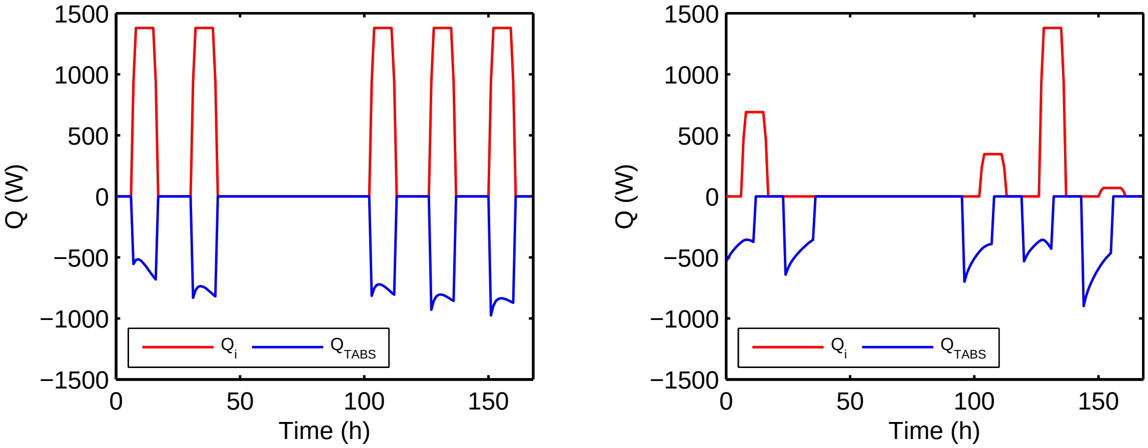

(a) **(b)**

Figure 3.7 – TABS cooling rate (blue) and internal load (red) profiles for (a) training data set 1 and (b) training data set 2, all for zone with TABS

set of the validation data (Figure 3.8b) is used to analyze the model accuracy in the case when cooling is delivered solely from floor or heating delivered from internal gains. The inverse model with three past terms gave good 24-hour-ahead predictions for the zone temperature T_z, operative temperature T_o, floor temperature T_{floor} and water return temperature $T_{w,return}$ for a typical summer week in Atlanta (Figure 3.9 and Figure 3.10). Relative errors are calculated as:

$$Relative\ error = \frac{X_{TRNSYS} - X_{inverse}}{\max(X_{TRNSYS}) - \min(X_{TRNSYS})} \times 100 \tag{3.19}$$

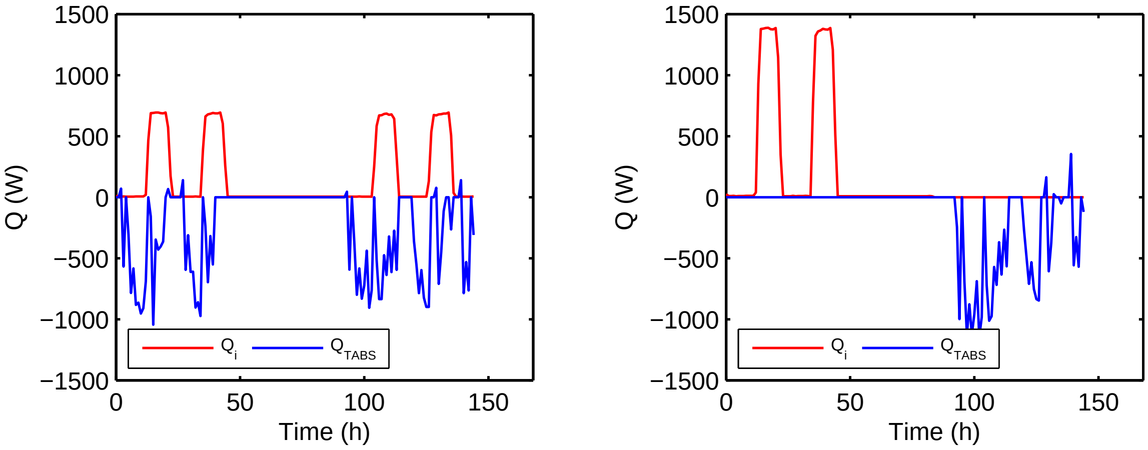

(a) **(b)**

Figure 3.8 – TABS cooling rate (blue) and internal load (red) profiles for (a) validation set 1, and (b) validation set 2, all for zone with TABS

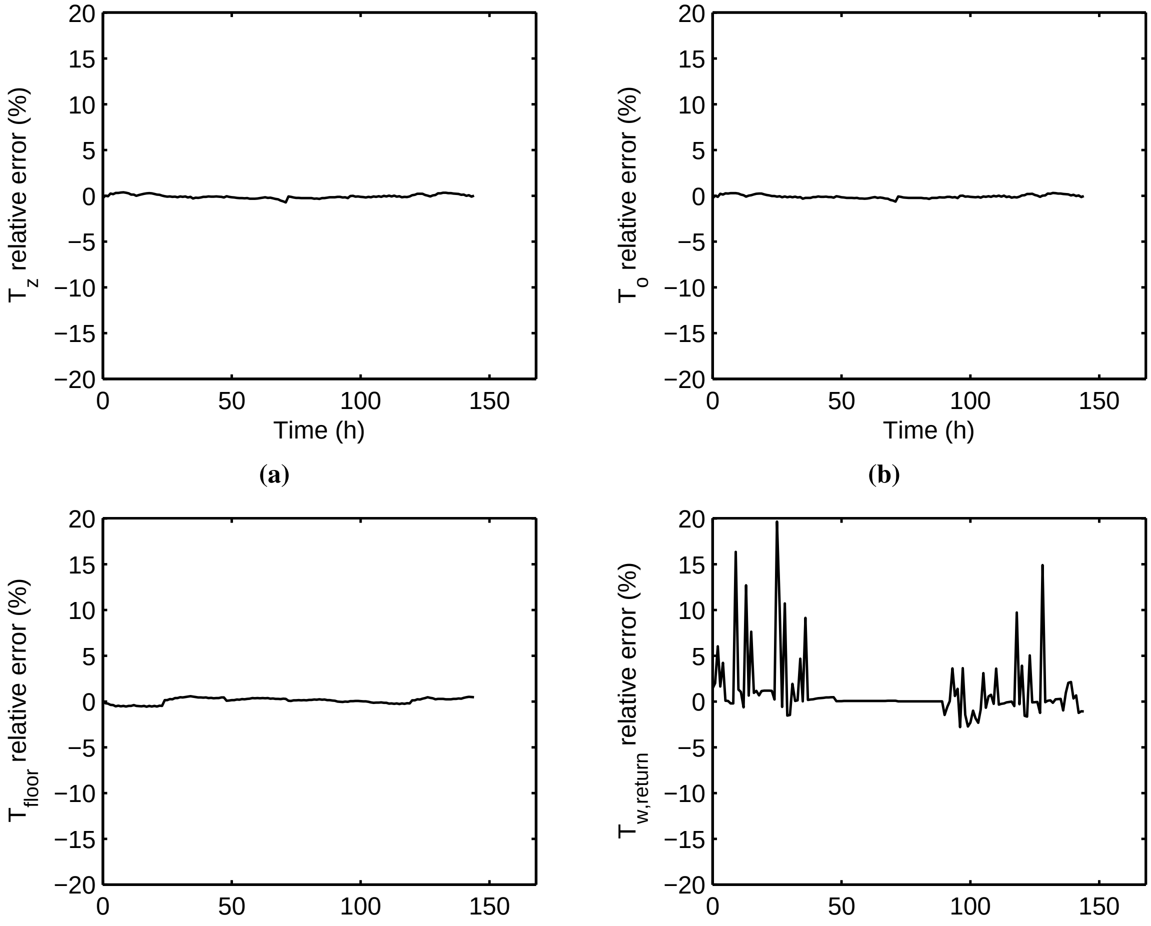

(a) (b) (c) (d)

Figure 3.9 – Comparison between TRNSYS model and inverse model A for 24-hour-ahead predictions of (a) zone temperature, (b) operative temperature, (c) floor temperature, and (d) water return temperature. Data used are from validation set 1, all for zone with TABS

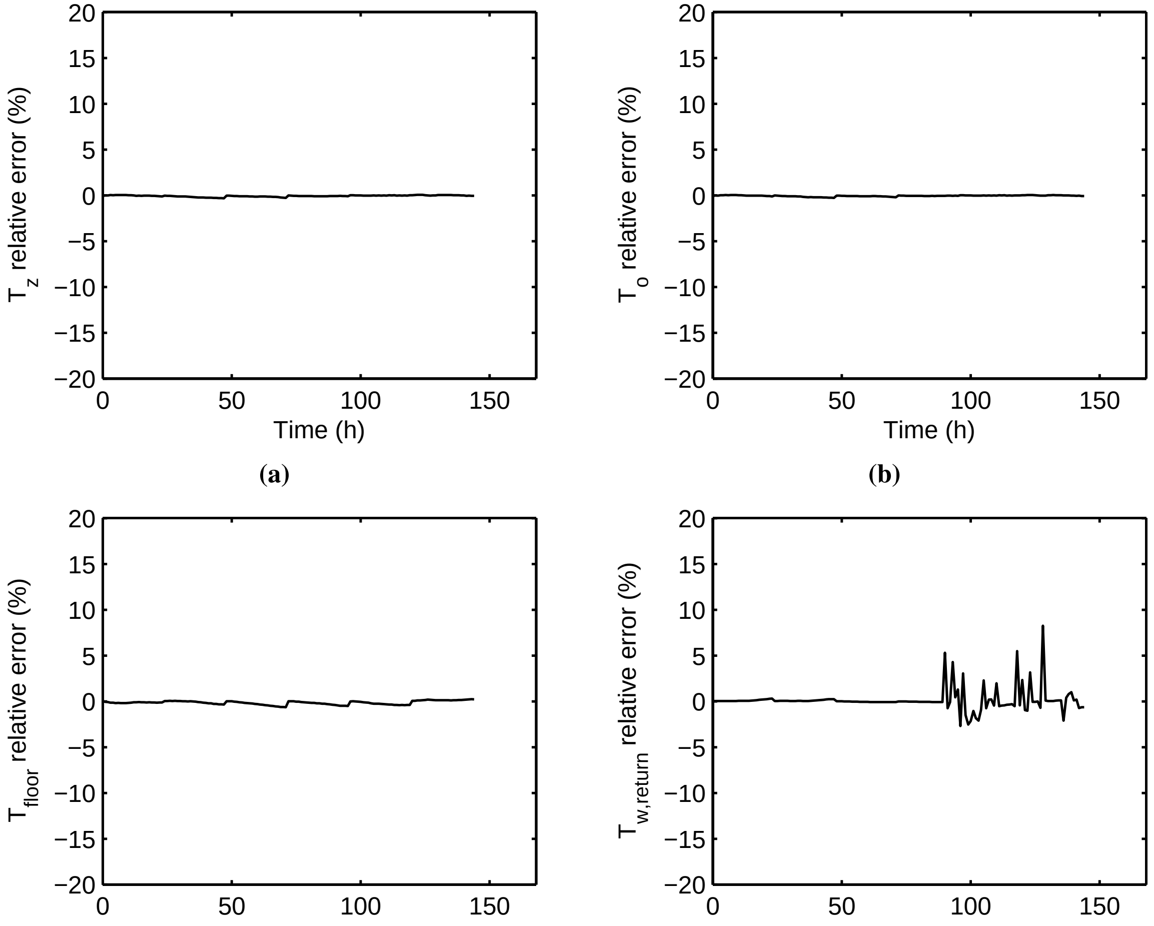

(a) **(b)** **(c)** **(d)**

Figure 3.10 – Comparison between TRNSYS model and inverse model A for 24-hour-ahead predictions of (a) zone temperature, (b) operative temperature, (c) floor temperature, and (d) water return temperature. Data used are from validation set 2, all for zone with TABS

3.3.3 Sensitivity analysis of inverse model A to number of past terms

The sensitivity analysis on the first validation set (Figure 3.8a) shows that using three past terms offers a good balance between the accuracy and computational speed for this particular room (Table 3.3). The relative mean square error in Table 3.3 is calculated as:

$$Relative\ RMSE = \text{mean}\sqrt{\left(\frac{X_{TRNSYS} - X_{inverse}}{\max\left(X_{TRNSYS}\right) - \min\left(X_{TRNSYS}\right)}\right)^2} \tag{3.20}$$

Table 3.3 – Sensitivity analysis for number of past terms in inverse model A

Number of past terms	Relative RMSE			
	$\mathbf{T}_z$	$\mathbf{T}_o$	$\mathbf{T}_{floor}$	$\mathbf{T}_{w,return}$
2	0.0361	0.0268	0.0081	0.0192
3	0.0012	0.0011	0.0027	0.0149
4	0.0015	0.0012	0.0012	0.0180
6	0.0027	0.0035	0.0006	0.0644
8	0.0019	0.0008	0.0003	0.0674

3.3.4 Inverse model A validation – thermal response of a zone with parallel TABS and air system

In addition to the TABS system, the room can have sensible cooling from either a VAV, convective, or a direct expansion system (indoor unit), which all represent an instantaneous convective cooling rate that needs to be accounted for in Equations 3.14 – 3.16. It is not straightforward to assume that the additional sensible cooling, which is purely convective, can be simply added to the zone's internal loads since internal loads have a certain convective-to-radiative heat transfer split. Two validation data sets are used to test the inverse model when convective air cooling and cooling through the slabs are acting in parallel. The first validation set (Figure 3.11a) represents the case with only internal gains an convective air cooling, while in the second validation set (Figure 3.11b) both TABS and convective air cooling act in parallel. If the convective air cooling rates are simply added to the internal load term in Equations 3.14 – 3.16, the results show relatively large prediction errors for the both validation sets (Figure 3.12 and Figure 3.13). Relative errors are calculated using Equation 3.19.

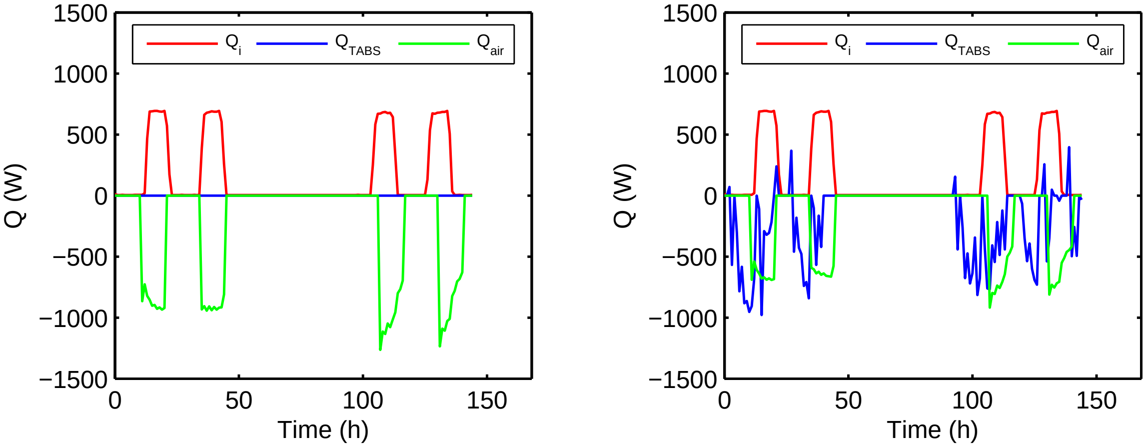

(a) **(b)**

Figure 3.11 – TABS cooling rate (blue), air cooling rate (green), and internal load (red) profiles for (a) validation set 1 and (b) validation set 2, all for zone with parallel TABS and air system

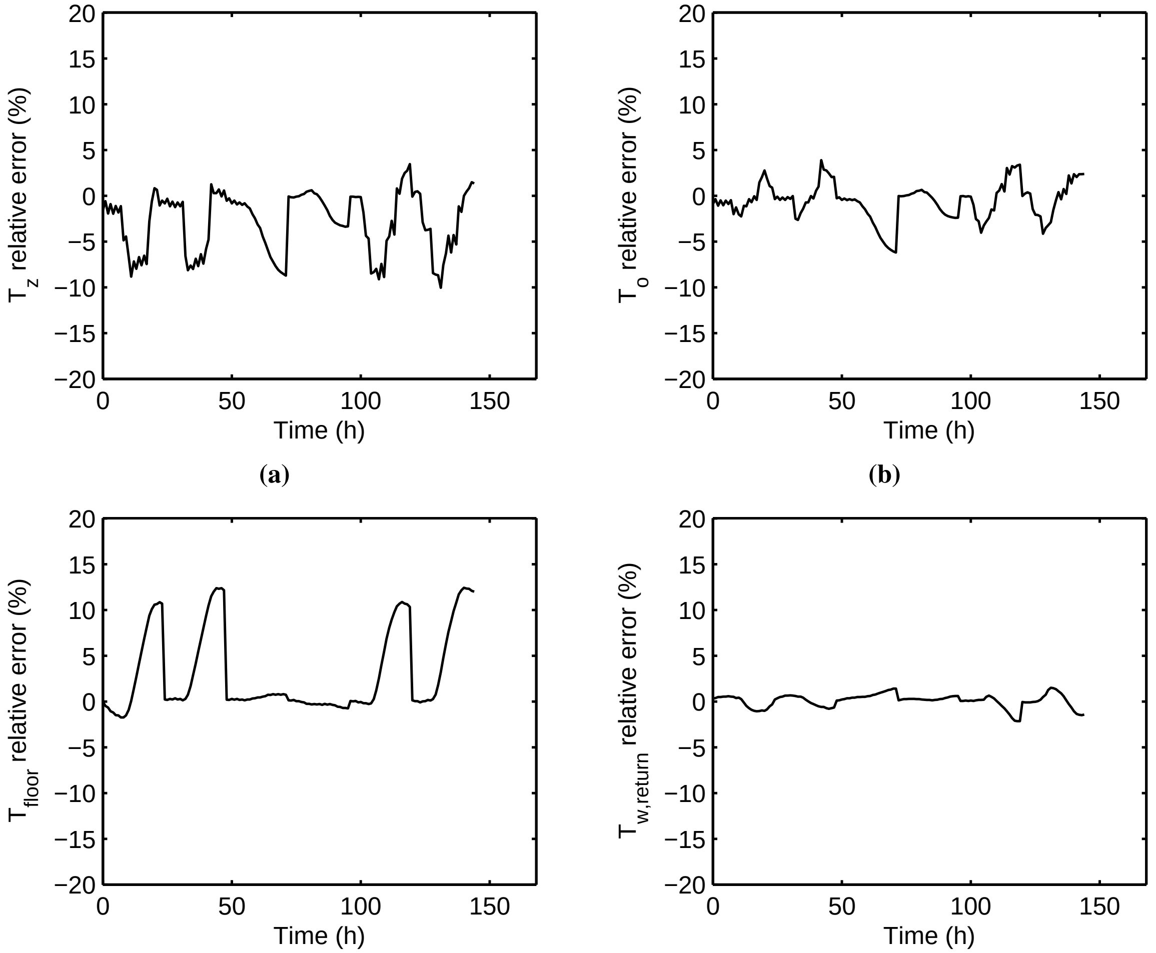

(a) **(b)** **(c)** **(d)**

Figure 3.12 – Comparison between TRNSYS model and inverse model A for 24-hour-ahead predictions of (a) zone temperature, b) operative temperature, c) floor temperature, and d) water return temperature. Data used are from validation set 1, all for zone with parallel TABS and air system

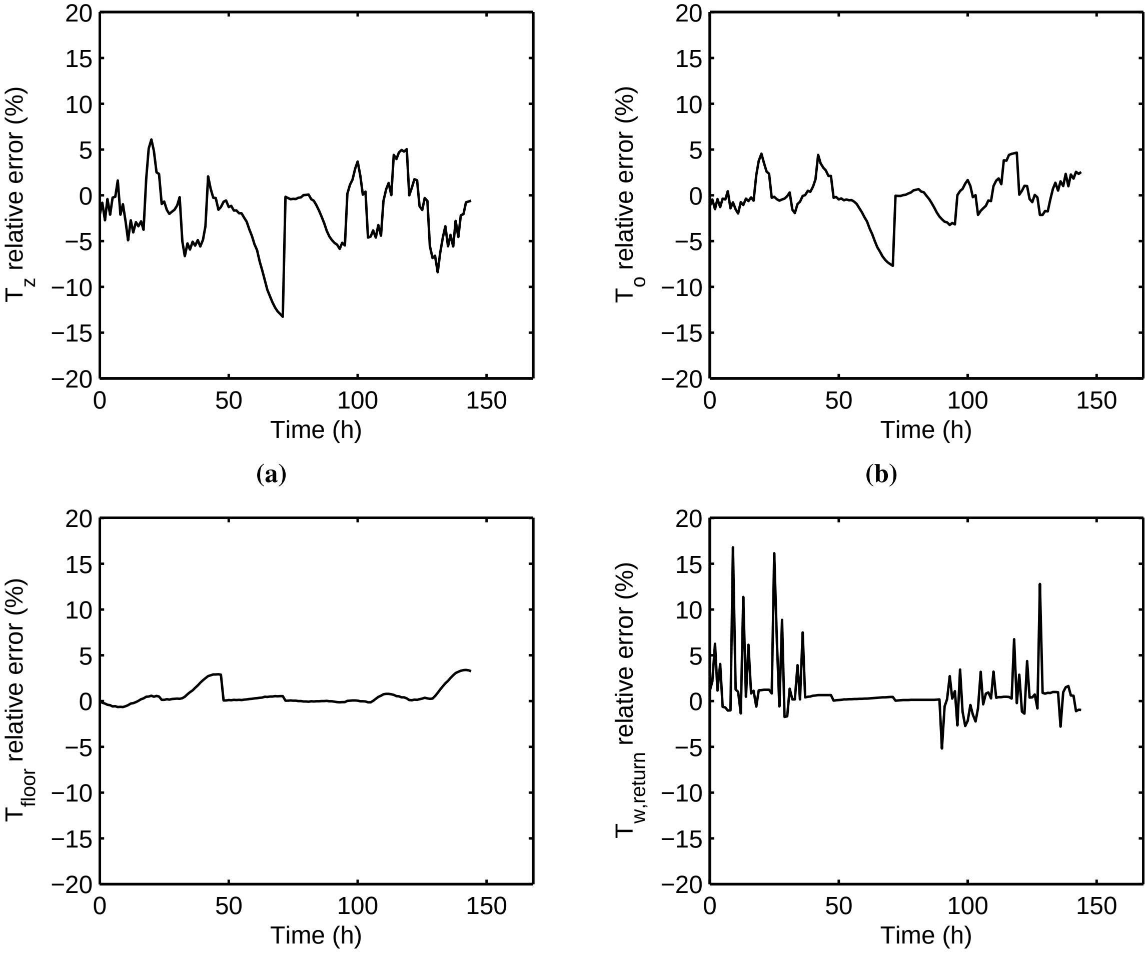

(a)

(b)

(c)

(d)

Figure 3.13 – Comparison between TRNSYS model and inverse model A for 24-hour-ahead predictions of (a) zone temperature, (b) operative temperature, (c) floor temperature, and (d) water return temperature. Data used are from validation set 2, all for zone with parallel TABS and air system

3.3.5 Inverse model B – thermal response of a zone with parallel TABS and air system

To improve the inverse model predictions in cases when TABS cooling, internal loads and additional convective air cooling/heating act together, Equations 3.14 – 3.16 have been modified by splitting the third term into a convective and radiative gain. Cooling through the slab is still treated as a separate variable, since it represents the cooling rate on the chiller. Modified equations are:

$$T_z = \sum_{t=1}^{n} a_z^t T_z^t + \sum_{t=0}^{n} b_z^t T_{adj}^t + \sum_{t=0}^{n} c_z^t T_x^t + \sum_{t=0}^{n} d_z^t Q_{TABS}^t + \sum_{t=0}^{n} e_z^t Q_{conv}^t + \sum_{t=0}^{n} f_z^t Q_{rad}^t \tag{3.21}$$

$$T_o = \sum_{t=1}^{n} a_o^t T_o^t + \sum_{t=0}^{n} b_o^t T_{adj}^t + \sum_{t=0}^{n} c_o^t T_x^t + \sum_{t=0}^{n} d_o^t Q_{TABS}^t + \sum_{t=0}^{n} e_o^t Q_{conv}^t + \sum_{t=0}^{n} f_o^t Q_{rad}^t \tag{3.22}$$

$$T_{floor} = \sum_{t=1}^{n} a_f^t T_{floor}^t + \sum_{t=0}^{n} b_f^t T_{adj}^t + \sum_{t=0}^{n} c_f^t T_x^t + \sum_{t=0}^{n} d_f^t Q_{TABS}^t + \sum_{t=0}^{n} e_f^t Q_{conv}^t + \sum_{t=0}^{n} f_f^t Q_{rad}^t \tag{3.23}$$

where Q_{rad} accounts for 50% of the internal loads from people, equipment and lights, and Q_{conv} for the other 50% of the internal loads and 100% of the additional cooling/heating.

To calculate zone temperatures using Equations 3.21 – 3.23, cooling rates delivered to the room by ventilation and/or infiltration must be known. However, the parameters that are usually known are ventilation/infiltration flow rates and temperatures, while the amount of delivered cooling depends on the zone temperature. Because the zone temperature and cooling rates are coupled, the iteration loop shown in Figure 3.14 has been added to the inverse model. Although this addition somewhat increased computational time, the inverse model is still significantly faster than the TRNSYS model. Simulating one week on an i7-2600@3.4 GHz processor took about 0.005 seconds for the inverse model without the additional interpolation loop, 0.5 seconds with the additional interpolation loop, and 2-3 seconds for the TRNSYS model.

3.3.6 Inverse model B validation – thermal response of a zone with parallel TABS and air system

After new coefficients have been found using the new training data set shown in Figure 3.15, the model has been validated using the same two validation data sets as for the previous comparison (Figure 3.11). It can be seen from Figure 3.16 and Figure 3.17 that splitting the loads into convective and radiative significantly improves temperature predictions. The RMS errors for both the original and modified inverse model are shown in Table 3.4 and are calculated according to Equation 3.24. The return water temperature predictions are not strongly influenced by this improvement, since the zone loads are not a direct input for the water return temperature calculation (Equation 3.17).

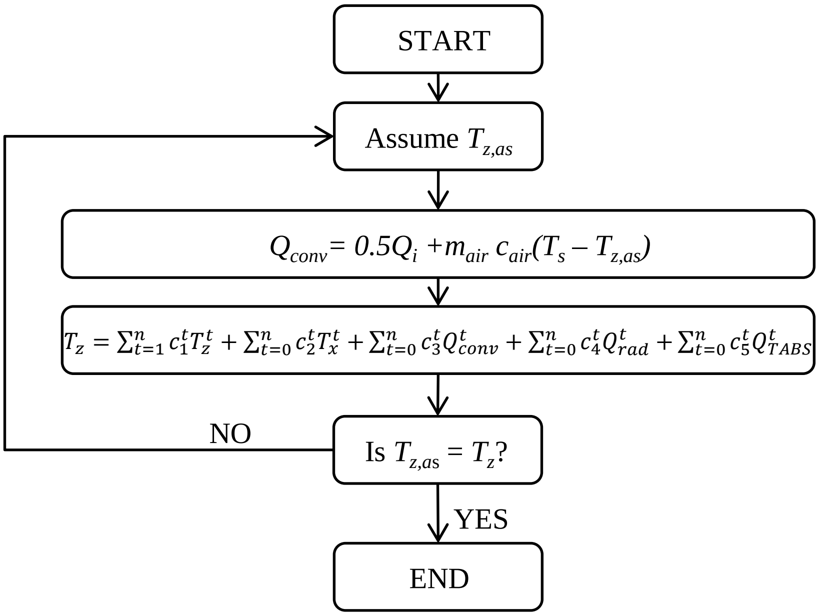

Figure 3.14 – Iteration loop for the case when m_{air} of ventilation and/or infiltration air with temperature T_s is supplied to the room

Table 3.4 – Comparison between inverse model A and inverse model B for case with parallel TABS and air system

	Relative RMSE			
	$\mathbf{T}_z$	$\mathbf{T}_o$	$\mathbf{T}_{floor}$	$\mathbf{T}_{w,return}$
Validation set 1, original model	0.0322	0.0165	0.0062	0.0150
Validation set 2, original model	0.0169	0.0089	0.0026	0.0052
Validation set 1, modified model	0.0011	0.0011	0.0049	0.0150
Validation set 2, modified model	0.0008	0.0006	0.0029	0.0052

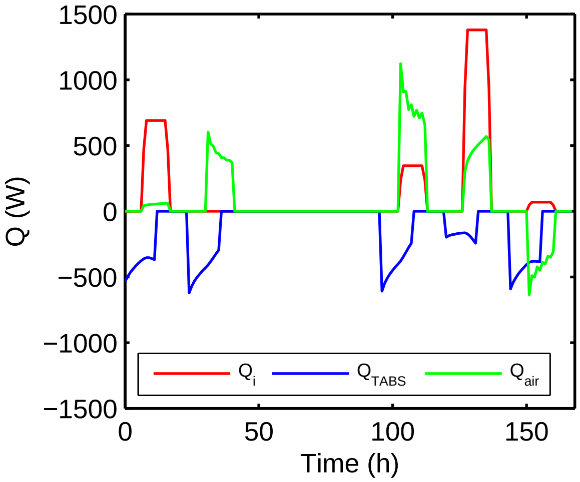

Figure 3.15 – TABS cooling rate (blue), air cooling/heating rate (green) and internal load (red) profiles for new training data set for zone with parallel TABS and air system

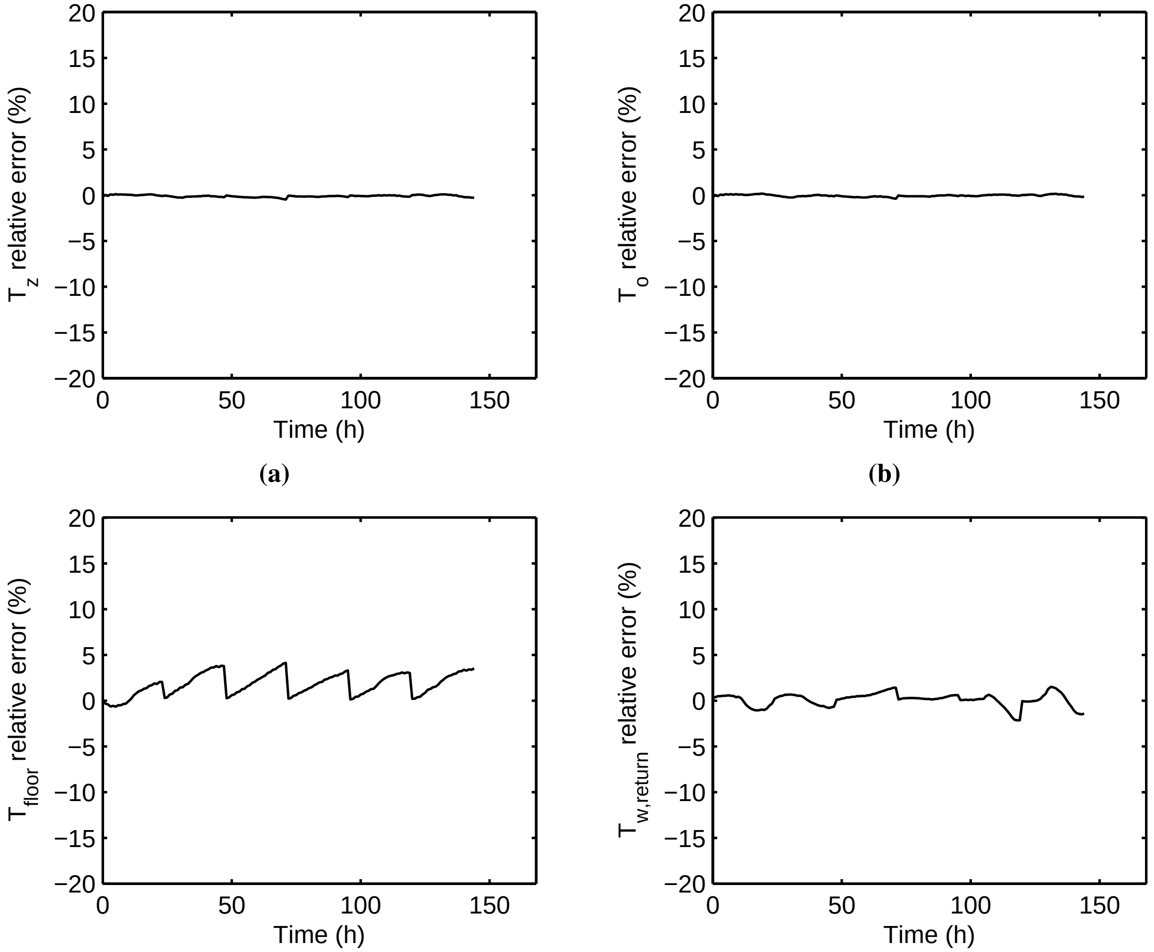

(a) **(b)**

(c) **(d)**

Figure 3.16 – Comparison between TRNSYS model and inverse model B for 24-hour-ahead predictions of (a) zone temperature, b) operative temperature, c) floor temperature, and d) water return temperature. Data used are from validation set 1, all for zone with parallel TABS and air system

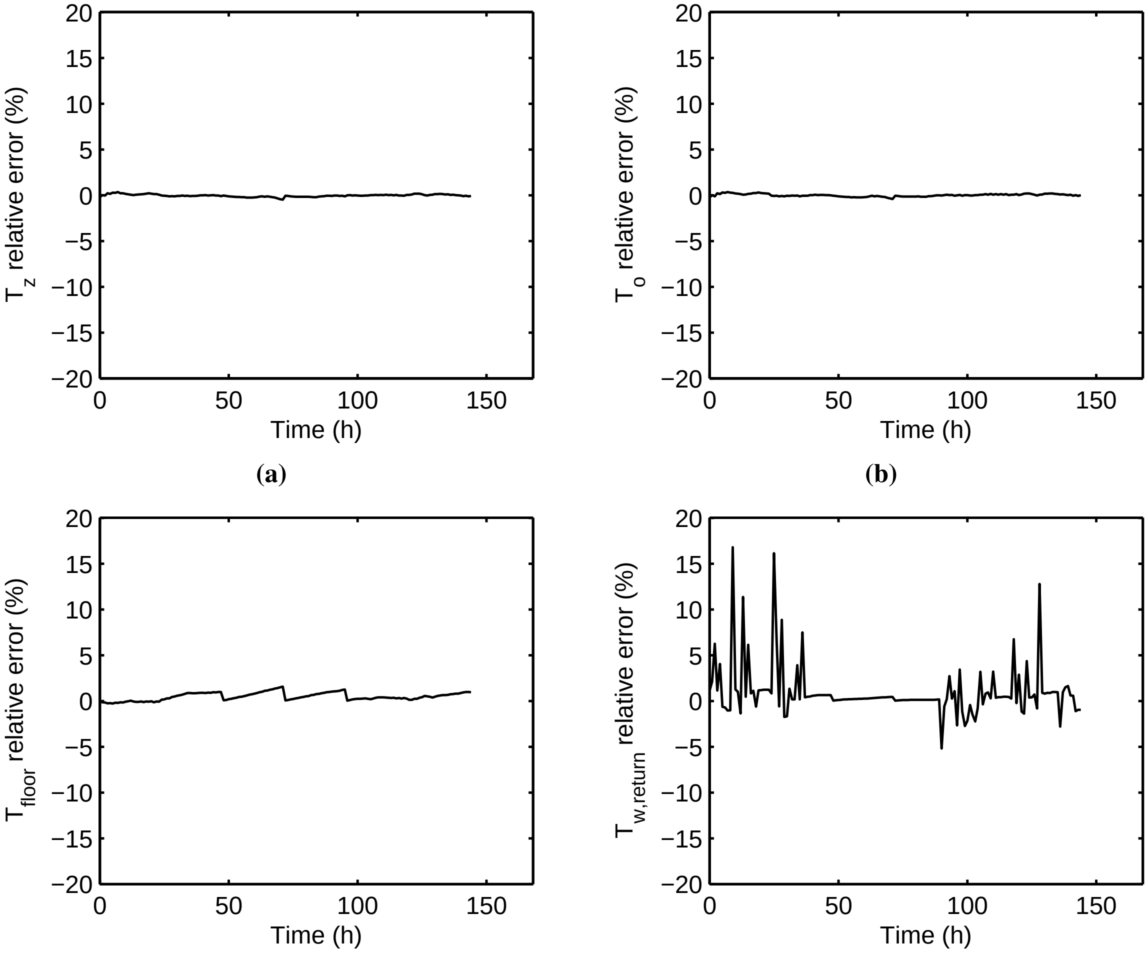

(a) **(b)**

(c) **(d)**

Figure 3.17 – Comparison between TRNSYS model and inverse model B for 24-hour-ahead predictions of (a) zone temperature, (b) operative temperature, (c) floor temperature and (d) water return temperature. Data used are from validation set 2, all for zone with parallel TABS and air system

3.3.7 Sensitivity analysis of inverse model B to number of past terms

The inverse model B uses past three terms to predict the zone, operative, water return and floor temperature, same as the inverse model A. The results in Table 3.5 show how the prediction error changes depending on the number of past terms, based on the analysis performed on the first validation set (Figure 3.11a). The relative mean square error in Table 3.4 is calculated as:

$$Relative\ RMSE = \text{mean}\sqrt{\left(\frac{X_{TRNSYS} - X_{inverse}}{\max\left(X_{TRNSYS}\right) - \min\left(X_{TRNSYS}\right)}\right)^2} \tag{3.24}$$

Table 3.5 – Sensitivity analysis for number of past terms in inverse model B

Number of past terms	Relative RMSE			
	T$_z$	**T**$_o$	**T**$_{floor}$	**T**$_{w,return}$
2	0.0308	0.0285	0.0105	0.0161
3	0.0011	0.0011	0.0049	0.0150
4	0.0012	0.0012	0.0010	0.0169
6	0.0024	0.0040	0.0003	0.0278
8	0.0007	0.0015	0.0003	0.0388

3.3.8 Inverse model for hygric response

The inverse model for hygric response uses similar transfer functions as for temperature calculations, with the room humidity as a function of the past humidity and past and current latent loads:

$$w_z = \sum_{t=1}^{n} g^t w_z^t + \sum_{t=0}^{n} h^t L_{gain}^t \tag{3.25}$$

Similarly as for ventilation/infiltration sensible gains, the latent load depends on the zone's humidity, and vice versa. Therefore, the iteration loop similar to the one shown in Figure 3.14 has been added for the alternative humidity model.

Coefficients g and h are found by the linear regression to TRNSYS training data (Figure 3.18), which assume internal latent gains (e.g. a latent gain per person is approximately 0.07 kg/h) and latent loads due to ventilation/infiltration.

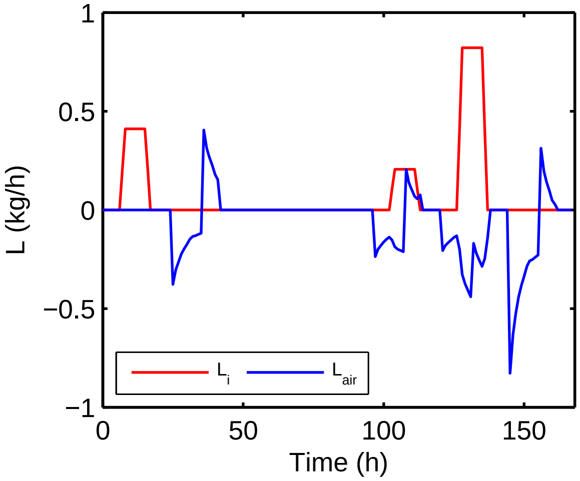

Figure 3.18 – Latent loads for training data set

3.3.9 Validation of inverse model for humidity response

Another set of TRNSYS data shown in Figure 3.19 is used as the validation data set. It can be seen from Figure 3.20 that the inverse model shows relatively good agreement with TRNSYS data, and is therefore used in the optimization algorithm.

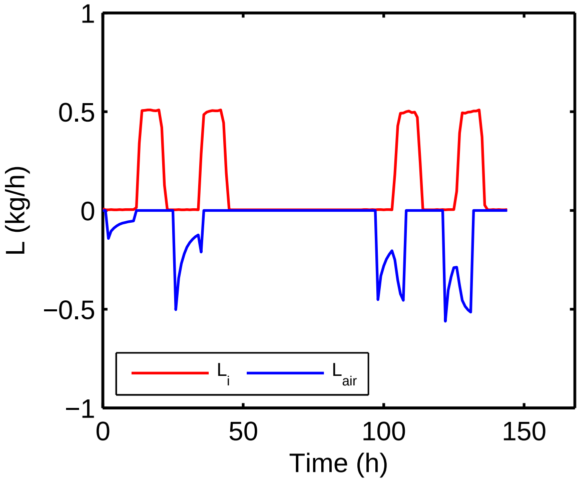

Figure 3.19 – Latent loads for validation data set

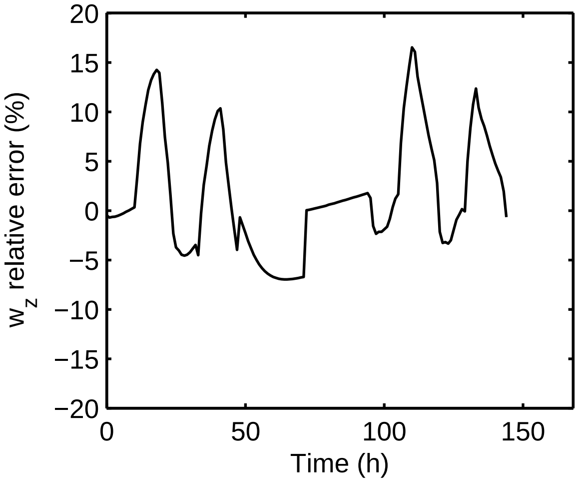

Figure 3.20 – Comparison between TRNSYS model and inverse humidity model for 24-hour-ahead predictions of zone humidity

3.3.10 Conclusion

Both the TRNSYS and inverse building model presented in this chapter are embedded in the MPC algorithm, as described in Chapter 4.

The TRNSYS model offers comprehensive simulation of a building's thermal and hygric response and has been validated using the experimental data for a typical summer week in Atlanta. The model is used to represent a "virtual building," as well as to create training and validation data for the inverse model.

The inverse model is more appropriate for the optimization algorithm since it significantly reduces computational time. For comparison, predicting the zone, operative, floor and water return temperature for a typical day, took approximately 0.3 seconds for the TRNSYS model and 0.05 seconds for the inverse model. This becomes extremely important for the MPC optimization function, where these calculations are performed hundreds of times for the 24-hour cooling strategy optimization. The inverse model also showed very good agreement with TRNSYS data, indicating that the optimization accuracy is not compromised for computational time.

For a zone that has the parallel TABS and air system, the inverse model for thermal response needs to be modified to account for purely convective heating/cooling of the air system. Appendix C gives coefficients for the inverse model used for the zone with TABS (inverse model A), and the modified model used for the zone with the parallel TABS and air system (inverse model B).

Chapter 4

Model predictive control

Model predictive control (MPC) is an algorithm that based on weather and load predictions decides on the optimal control strategy while ensuring thermal comfort for occupants. Although the objective of this research was to minimize the total energy consumption for cooling, different objectives, such as the total cost of electricity, can be achieved by modifying the objective function.

To determine whether the proposed strategy leads to a comfortable building conditions, the optimization algorithm needs to include a building model capable of predicting building dynamics. The MPC optimization is usually performed once per day, in the case of perfect weather and load predictions, or more often (e.g. each hour) in the case of a real-building optimization, which requires more frequent feedback information. This puts a constraint on computational time, and influences the selection of a building model and an optimization algorithm. The goal of this research was to develop a tool for the MPC analysis that can be widely used and also be fast enough for implementation in a real building. Therefore, only tools that would give a fast building response and that are commercially available were to be considered. Both the issue of computational speed and especially the issue of initialization of variables described in Chapter 3 were motives to use the inverse model based on a comprehensive room transfer function. The TRNSYS model is still used to the find the inverse model coefficients, and to more accurately predict how will a "virtual building" respond to optimized cooling rates. The results of the heat pump static optimization described in Chapter 2 are also used by the optimization algorithm to predict electrical energy for cooling as a function of cooling rates, water/air temperatures and ambient conditions.

This chapter gives the literature review on MPC, as well as the control for thermally activated building surfaces (TABS) with and without the predictive control. Furthermore, it describes three alternatives considered for the MPC algorithm and explains in more detail the one that was chosen. The objective function was defined with a goal of minimizing total cooling energy while maintaining the thermal comfort.

4.1 Literature review

There is an abundance of data found in the literature on systems for cooling and heating through large building surfaces, mainly floors and/or ceilings. However, the potential savings are shown to be very dependent on the weather conditions, the reference system used for the comparison, system components, and system controls. For example, the analysis done by Niu et al. (1995) on a cooled-ceiling system showed no significant improvement over a conventional variable air volume (VAV) system in the Danish climate. However, an implementation of a cooling tower in addition to a cooled-ceiling system had a significant impact, with up to 49% chiller energy savings. For the Tokyo climate, Imanari et al. (1999) showed 10% savings in annual energy consumption for ceiling panels compared to a conventional VAV system, 20% of which came through savings in the transport energy.

For an experimental room with a constant air volume system, Stoecker et al. (1981) analyzed the influence of a space thermostat throttling range (a room's temperature offset from a set point) on a reduction in peak cooling loads. With a throttling range that resulted in a zone temperature swing of 2.7°C, the reduction in peak cooling was 34%. Shapiro et al. (1988) also experimentally tested the control strategy that benefits from lower night temperatures. Although it was reported that the thermal comfort was maintained, and that there is a potential for large savings, the savings were not quantified.

Spratt et al. (1989) developed a control system that utilizes "free" night cooling and tested it on a real building. Compared to the conventional control strategy, occupant surveys indicated that the thermal comfort was maintained, with 41% of occupants even stating that the comfort level was improved. However, cost savings associated with a use of the predictive control were not quantified.

Using a data driven (inverse) model for the building dynamics, Rabl and Norford (1991) analyzed the potential for a peak cooling load reduction using the precooling of a building mass. The proposed control strategy resulted in 10–20% peak load reduction for a real office building, with 2°C temperature decrease over the precooling period.

Olesen et al. (2002) investigated several control strategies for a building with TABS. They performed a parametric study for different operation times, an intermittent pump operation and water supply temperature control. The best thermal comfort and energy performance was achieved when the water temperature (supply or average) was controlled based on the outside temperature. A proposed linear relation between the water temperature and outside temperature can be found in the paper. Furthermore, it was concluded that the time of operation can be limited by operating the system only at night time (6 pm–6 am used in the paper), or by using the intermittent operation for the pump. The limited operation time resulted in a reduced energy consumption, without compromising the thermal comfort.

Gwerder et al. (2007) compared the base case TABS control with the water supply temperature function of the mean outside temperature (over the last 24 hours) against a more advanced TABS control. The advanced control included a room temperature feedback and a pulse width modulation (PWM) approach for the pump on/off operation. Although the PWM control resulted in reduced pump operating hours, it also increased the total heating and cooling demand. Adding a room temperature feedback helped to avoid this issue, resulting in a similar heating and cooling energy compared to the base case but 75%

reduction for the pump-on period. The companion paper (Todtli et al., 2007) presented a systematic method for the system design and control integration. Two methods that can be used to calculate the PWM are described in Gwerder et al. (2009).

Henze et al. (2008) analyzed heating and cooling energy saving potential for a ventilation-assisted thermo-active system. TABS thermal response was captured by modeling a simplified active layer with prescribed temperatures and heat fluxes. Assuming a ground heat exchanger with unlimited capacity, all heat from the TABS was assumed to be transferred directly to the ground in a cooling season, while a heat pump was used to raise the water temperature in the heating season. In both heating and cooling mode, electricity was still required for the VAV ventilation system with the assumed constant heat pump COP of 4, and for the auxiliary systems (fans and pumps). Although resulting in 4% higher thermal energy consumption, the hybrid system showed 20% savings in the delivered (site) electricity, mainly reducing loads on a cooling coil and reduced fan power. The hybrid system also resulted in higher thermal comfort due to lower operative temperatures during occupied hours. The coordination between the TABS and VAV ventilation system was recognized as a critical issue that required further analysis.

Sourbron et al. (2009) investigated several TABS control strategies for a small office building modeled as a simplified resistance-capacitance (RC) network. The system utilized a direct ground heat exchanger connected to a heat pump serving TABS, and an air-handling unit for supplementary heating or cooling. The water supply temperature control was based on the zone temperature with (a) 1.5°C dead-band between a heating and cooling setpoint, (b) 3°C dead-band, and (c) only night precooling with a constant water temperature. Compared to a conventional all-air system, the TABS system with the control strategy (a) and (b) resulted in significantly higher primary energy consumption (37% and 26% respectively), due to frequent switching between heating and cooling mode. The control strategy (c) resulted in 80% primary energy reduction compared to a conventional VAV system. However, thermal comfort was not always adequate due to the large time constant of the TABS system, which suggested that the TABS systems could benefit from an additional system with a shorter response time. The subsequent work (Sourbron and Helsen, 2010) analyzed how the choice of a control variable influences energy use and thermal comfort. Among the zone temperature, operative temperature, TABS core temperature and TABS surface temperature, the TABS surface temperature is suggested as the best option and the operative temperature as a good alternative.

Kummert and Andre (2005) used optimal control for a building heating system with a goal of minimizing the boiler energy consumption. The reference zones (north and south) were represented in a state-space form through a resistance-capacitance (RC) network. Compared to a typical control, the optimal control saved 3–10% energy for the reference zones over a whole heating season but was not able to achieve savings for the non-reference zones.

Braun (1990) used MPC on a single building zone with the goal of minimizing the VAV system operating cost and peak cooling loads over 24 hours. The optimization variable was the zone setpoint temperature, and the dynamic optimization was repeated for different precooling periods. A cooling plant with cooling towers was also optimized, but decoupled from the building optimization. A plant with a "good," "flat" and "poor" part-load characteristic was included in the analysis. The "good" characterized a heat pump with variable speed motors for the compressor, fans and pumps, and the "poor" utilized fixed-speed equipment. While the efficiency for the "good" improved at part-load conditions, with the peak efficiency at 30–50% of the design load, the efficiency for the "poor" was at its maximum for the design load and significantly reduced for off-design conditions. Building thermal response was captured using the comprehensive room transfer function method developed by Seem (1987), while hygric response predictions used the lumped capacitance method for the moisture storage components. Humidity control was not considered; instead, the humidity was allowed to float between comfortable limits. Based on a single-day optimization, savings achieved through the use of MPC were 10–50% in the energy cost, and 10–35% in the peak power. Even without special time-of-day utility rates, the system with MPC resulted in 35% savings in the operating cost, mainly due to "free" night cooling. In the subsequent work Lee and Braun (2004) used the state-space building model described in Chaturvedi and Braun (2002) to apply the advanced control on the ERS building at the Iowa Energy Center. Building measurements were used to train the inverse model, as well as for the validation. A day was divided into four time periods (unoccupied, occupied-off peak, occupied-on peak and unoccupied), and different setpoint temperatures were assigned to each. By analyzing different period lengths and setpoints, the peak cooling power demand was reduced by 25–45%. Three practical methods for determining setpoint trajectories that would result in the near-optimal performance by minimizing the peak cooling demand are presented in Lee and Braun (2008a). The companion paper (Lee and Braun, 2008b) evaluated the performance of presented methods for three buildings representative of a small, medium and large commercial site. The simulations showed 33–51% reduction in peak cooling load over summer months.

Krarti et al. (1995) developed a simulation environment for the optimal control of an ice-storage system, taking into account utility rate structures and cooling plant characteristics. Using that environment, Henze et al. (1997) analyzed the MPC potential for a building with active thermal storage, where the ice-storage charge was optimized for the minimum cost of electricity. The optimization assumed a constant COP and neglected the required fan power. They investigated different lengths of the planning horizon, where the planning horizon represented the time interval over which the cost function was evaluated. Results showed that the planning horizon on the order of 24-hours is only marginally sub-optimal compared to the horizon over a simulation period of one week. To analyze MPC for a prototypical three-story office building with active and passive storage and VAV system, Krarti and Henze (2005) integrated EnergyPlus and GenOpt. This required modifications in the EnergyPlus code, described in detail in Phase 1 of that report. The additional model was done in TRNSYS, using the version of the TRNSYS source code not commercially available (Henze, 2012). Optimizing a day with 24 hourly setpoints took 1–4 hours for the Nelder-Mead simplex method and 8–29 hours with the OptQuest (population-based scatter search) method. To reduce computational time, a day was divided into four time periods (unoccupied-offpeak, unoccupied-onpeak, occupied-onpeak, and occupied-offpeak), with a constant setpoint temperature for each. This reduced the computational time to 1–5 minutes for Nelder-Mead and 3–4 hours for OptQuest without making significant differences in cost savings, and even resulting in a slightly better performance for certain cases. This indicated, first, that the 24-variable optimization was occasionally stuck in the local minima and, second, that the function was relatively flat near the optima. The results showed 10–20% reduction in the operating cost, with a 4 to 8-hour precooling period being the most effective. The analysis of the modeling uncertainty, with five parameters being zoning, geometry, construction material, internal loads and chiller plant COP, showed that zoning and building geometry had only a marginal impact on the results. The analysis of short-term weather forecasting models suggested that the bin model (which uses the observations from last 30 and 60 days) had the best prediction accuracy. The use of the bin model resulted only in marginally different cost savings compared to the case with perfect weather knowledge. Although the fan energy was not part of the optimization objective function, the field testing of the Energy Resource Station in Ankeny, IA, revealed that that fan energy can have a significant influence on the predictive controller decisions and, therefore, cannot be neglected.

Henze et al. (2010) further analyzed the cost savings for an optimally controlled building with a VAV system. Factors that were identified as the driving factors for a saving potential are the utility rates, building mass, internal loads, equipment efficiency, and equipment part-load performance. The highest savings were achieved for a building with high utility incentives, low internal gains, and with the equipment characterized by good part-load performance. No real savings were achieved for a building with high internal loads, regardless of the thermal mass. The cost savings for top relative performers were 12–27% for a month in September. Although the weather influenced the magnitude of the total cost, the savings potential was strongly influenced by the local utility rates, and was relatively insensitive to the weather. The analysis also showed that longer precooling at lower rates saved more energy. When the optimal control was simplified using the average values of the optimal setpoints, the results showed no significant difference in cost savings. This, again, suggests that the objective function is relatively flat near the optimum. The optimal setpoints were influenced by monthly temperature values, but only mildly by the daily temperature variations. However, although resulting in a substantially simpler control, acquiring the averaged setpoints still required the use of the more complex MPC environment.

Spindler and Norford (2009) and May-Ostendorp et al. (2011) showed that MPC can also be successful in optimizing a mixed-mode building behavior. While Spindler and Norford (2009) used the data-driven, inverse model trained on a real building, May-Ostendorp et al. (2011) employed the combination of EnergyPlus and MATLAB environment. Using the particle swarm optimization, May-Ostendorp et al. (2011) optimized a window operation in a mixed model building with 24-hour planning horizon and 2-hour optimization block. This resulted in 12 optimization variables of binary window decisions (window in position 0 or 1). The reported simulation time for 11 weeks in summer was 12 hours.

Corbin et al. (2012) described a framework for MPC that combines EnergyPlus and MATLAB and uses the particle swarm optimization. The algorithm can be used for MPC of different building systems, which was shown on two examples. The first example was MPC for a building with a VAV system, with a goal of minimizing the cost of electricity. For a week in August, the results showed 5.3% cost savings compared to a VAV system with conventional control. With 14 daily temperature setpoints as optimization variables, the simulation time for one week was 26 clock hours. The second example was MPC for a building with TABS and a ventilation system. The ventilation system was designed as a constant air volume system that delivers the minimum amount of fresh air, with a constant supply temperature of 20°C. The base case assumed that the TABS water supply temperature changes depend on the ambient temperature according to Olesen (2007). The proposed system utilized MPC with 6 time blocks per day (4-hour each), and with the water supply temperature and slab circulator availability (which mimic the pulse-width modulation) as the two optimization variables. The proposed system also assumed the use of the ground heat exchanger. For a simulated spring month in Stuttgart, the base case resulted in often switching between heating and cooling mode, since it immediately reacted to changes in the ambient temperature. The proposed system showed 54% energy savings compared to the base case, mainly through avoidance of over-conditioning and cooling/heating mode switching, as well as the use of the ground-loop bypass. To simulate one day for a building with 11 thermal zones and 12 optimization variables took one day of clock time.

Coffey et al. (2010) developed a software framework for MPC that combines GenOpt and SimCon with any building energy simulation program that can read and write into a text file. The connection between SimCon and the energy modeling software TRNSYS was enabled through the Building Control Virtual Test Bed. When compared to the typical control, the heuristic rules gave only marginally different results than MPC, with 28% versus 30% respectively in a peak cooling power reduction. However, it was suggested that MPC would be worth considering for more complex problems. To optimize one day using MPC, the reported computational time was 3 nights. However, it was not described how the presented framework would overcome the TRNSYS variable initialization problem for a building with TABS.

Verhelst et al. (2012) analyzed the influence of COP formulation on the optimized control strategy and the cost function for a hydronic radiant heating system. The building dynamics was simplified using four first-order differential equations. The typical TABS control using the heating curves was compared to the optimized control, all for the continuous, 24-hour heat pump operation. The COP was defined as a function of (a) part-load efficiency, ambient temperature and supply water temperature, (b) ambient and supply temperature, (c) ambient temperature only, and (d) as a constant. The electricity price was only considered for the compressor power. Although resulting in different compressor frequency and supply temperature profiles, the optimization of the water temperature using formulations (a) and (b) did not show significant differences in electricity consumption. The optimization using formulations (c) and (d) resulted in 14% and 7% higher electricity consumption respectively. However, when the cost function was modified to minimize the square of predicted electricity cost (which penalizes peak powers), formulations (c) and (d) gave similar predictions to the ones obtained by the heating curves, without the optimization.

Jiang et al. (2007) and Armstrong et al. (2009) proposed a system that integrates hydronic radiant cooling, variable-speed drive motors for a compressor and auxiliary fans and pumps, an active thermal energy storage, a dedicated outside air system, and a night precooling control strategy. The system was termed low-lift cooling, since it reduces pressure rise across the compressor. The condensing temperature is lowered through the use of night precooling, and the evaporating temperature is increased through the use of radiant slabs. While many different studies have shown the benefits of each separate component, this was the first study on the combined system. The building loads were evaluated using the DOE-2.2 simulation program, with the rest of the system modeled in MATLAB. TABS were modeled using the Number-Of-Transfer-Units (NTU)-method, and the thermal storage was assumed as ideal. The heat pump operation was optimized using a heat pump model based on first principles. The detailed description of the heat pump model, the combined model, and simulation assumptions can be found in Armstrong et al. (2009). Utilizing the active thermal storage and model predictive control, the cooling loads were shifted toward night time, taking advantage of lower night temperatures. This resulted in a peak load reduction as well as lower chiller energy consumption. Several case studies were done with different combinations of proposed components (hydronic radiant cooling, variable-speed drive, an active thermal energy storage, and a dedicated outside air system), to understand how, and to what extent, each of these elements influences the energy saving potential. The scoping studies were performed for five different US climates and three building types (low-performance, mid-performance and high-performance). When all four elements were implemented, cooling system energy savings were 30–70% compared to a typical VAV system (Armstrong et al., 2009). The largest savings were achieved for hot climates with larger temperature differences between day and night (e.g. Houston), while the lowest savings were for mild climates (e.g. Los Angeles). The largest "jumps" in the energy consumption were observed when implementing the thermal energy storage, even for the VAV system, and when adding the radiant cooling. The subsequent work (Katipamula et al., 2010) extended the analysis to 16 U.S. climates, confirming the promising energy savings results from the previous work. The market assessment done by an independent agency showed that this system represents an attractive option for the current market, and is worthy of further research and development. Two possible barriers based on the market assessment were the use of the advanced control, and an active thermal storage. For a successful adaptation, the advanced control of the novel technology would need to be user-friendly, and adapted for a building facility personnel. Furthermore, the potential customers were somewhat discouraged by the use of the active thermal storage, which in general takes useful space, and has shown to be challenging to control. This, however, does not represent a serious limitation for the proposed technology, since the building thermal mass can successfully be utilized as the passive thermal storage, as will be shown in this research. The capital cost estimate, performed for several building types, showed that office buildings represent ideal first candidates for the implementation of the novel system. Compared to a conventional system, an estimated incremental cost for a large office building was approximately 7.5 $\$/m^2$, while a medium office building even had negative incremental cost of -6 $\$/m^2$. The largest estimated incremental costs were 28 $\$/m^2$ for a school, and 60 $\$/m^2$ for a supermarket.

Promising results for the low-lift cooling system were a motivation for the experimental work done by Gayeski et al. (2012). In MIT's experimental room, he measured the performance of the TABS cooling system that employs predictive control and compared it to a high-efficiency variable-speed split-system air conditioner. Cooling rates for TABS were optimized 24-hours ahead, and the optimization was repeated each hour to account for unexpected changes in building response. The loads and weather conditions were controlled and therefore not a source of uncertainty. The empirical model of a low-lift chiller, based on the experimental measurements (Gayeski et al., 2011) was also implemented in the predictive control algorithm. The results for a typical summer week in Atlanta and Phoenix showed sensible cooling savings of 25 and 19% respectively relative to the split-system. The experimental work did not consider latent cooling.

Based on the work in the literature, both MPC and TABS have shown to be promising technologies, especially when combined together. However, the lack of detailed and robust tools for MPC is preventing more accurate analysis of these technologies and the identification of factors that influence their energy saving potential. Many analyses found in the literature have used simplified models for a building response, chiller control, or chiller plant. However, it was shown in Henze et al. (1997) that even neglecting the transport power can influence predicted optimal control and achieved energy savings. Therefore, the novel technologies that incorporate MPC could tremendously benefit from a more comprehensive MPC tool.

4.2 MPC algorithm

The MPC algorithm developed here for a building with a TABS and/or VAV system optimizes cooling rates for the lowest energy consumption. Different objective functions, such as the lowest operating cost, could also be implemented. Based on the predicted weather forecast and building loads, the optimization function finds the optimal cooling rates for each of the following 24 hours. The optimization function uses the inverse model for the building dynamic response, after which the optimal values are applied to the "virtual building," represented with the more accurate model in TRNSYS.

The total power consumption is a sum of the heat pump power required for air/water cooling and the fan/pump energy required to distribute air/water through the building. Furthermore, the heat pump power is a sum of the compressor power, evaporator fan/pump power and condenser fan power. The objective function also accounts for the comfort criteria by introducing the cost penalty when the temperature is outside the desired limits.

Thermal comfort is influenced by both air and surface temperatures, which becomes especially relevant for a zone with large cold or warm surfaces. One of the benefits of the radiant cooling system is that people might feel equally comfortable at slightly higher air temperatures compared to all-air systems. Therefore, the operative temperature, which takes into account the air temperature and a weighted average of surface temperatures, is chosen as the controlled temperature. To account for the cold-floor effect in a real building, where surface temperature measurements are usually not available, a more practical solution would be to set an air temperature setpoint 1–2°C higher than for the VAV system.

4.2.1 Setup A

The first intention for MPC was to combine GenOpt (Wetter, 2008) for the optimization part with TRNSYS for the building's thermal and hygric response. The objective function would be calculated in MATLAB, although the alternative option, to develop an objective function module inside TRNSYS, is also possible. After finding the optimal cooling rates, the second TRNSYS model would simulate the behavior of a "virtual building," using the optimal values as inputs. Figure 4.1 shows the schematic and simulation parameters for the TABS system MPC. The VAV system MPC schematic would be very similar, with air cooling rates as optimization parameters and the air flow rates as inputs to the "virtual building" (the supply temperature for the VAV system is assumed to be constant).

This particular setup was abandoned early on, mainly due to issues with initialization of variables, as explained in Chapter 3. Furthermore, this setup is somewhat similar to the MPC models found in the literature, for which reported computational times were not suitable for fast simulation and implementation in a real building. Finally, connecting GenOpt, MATLAB and TRNSYS, or even GenOpt and TRNSYS would not be straightforward, and would require the use of the Building Controls Virtual Test Bed as a connecting platform. This would add to model complexity and possibly further degrade computational speed.

4.2.2 Setup B

The next intention for the optimization part was to replace the TRNSYS building model with the inverse model. The optimization part combines GenOpt and MATLAB, where MATLAB is used to evaluate the objective function and building thermal response (Figure 4.2). The TRNSYS model still acts as a "virtual building," providing a more accurate response to the optimized parameters. The response from the "virtual building" is also an input for the next optimization step, since the inverse model requires the knowledge of the zone's thermal and hygric history.

GenOpt is a general optimization software that can be linked to other computer programs (including MATLAB, TRNSYS and EnergyPlus). Detailed instructions for the connection with TRNSYS can be found in Kummert (2007). The software manual (Wetter, 2008) offers a good insight into different types of optimization problems and appropriate optimization algorithms. For optimization problems that calculate the objective function using building modeling programs, the manual recommends some of the non-gradient optimization algorithms included in the GenOpt library, such as the combination of Particle Swarm Optimization (PSO) and Hooke-Jeeves Pattern Search (HJPS). PSO, inspired by a social behavior of, for example, bird flocking or fish schooling, has a swarm of particles moving around the search space, where the movements of individual particles are influenced by the improvements discovered by others in the swarm. This method is used in the first optimization stage to find an appropriate starting point for the HJPS method. HJPS, similar to the MATLAB built-in pattern search, takes steps in different search directions, modifying the step size and search direction every time a lower objective function cannot be found using the current step size.

4.2.3 Setup C

The third option for the optimization part was to use only MATLAB (Figure 4.3), which reduces the model complexity and possibly computational time. The optimization algorithm used is a MATLAB built-in pattern search algorithm. The pattern search is a non-gradient optimization method that does not guarantee finding the global minima (but neither do the gradient-based methods). However, as described in more details in Wetter (2008), gradient-based methods are not particularly suitable for the problems where the objective function is determined using building models, and can therefore be very dependent on building model tolerances. Furthermore, the chances of finding the global minima with the pattern-search method can be improved by choosing an appropriately large initial step, and/or starting with a different initial point. Setting the GenOpt-MATLAB connection (setup B) was notably more challenging than setting the whole optimization in MATLAB (setup C). Figure 4.4 shows the optimization results (only TABS sensible cooling) for a typical summer day in Atlanta using setup B and setup C. It can be seen from the results that both setup B and setup C predict night precooling as the optimal strategy, with marginal differences in the energy consumption between two setups (1020 Wh for setup B, and 1050 Wh for setup C). However, while it took 30 s to optimize TABS cooling rates over 24 hours with setup C, the computational time for setup B (with default GenOpt optimization settings) was approximately 45 minutes.

Setup C is chosen for MPC analysis due to its simplicity and computational speed. Assuming a perfect knowledge of weather data and predicted loads, the planning horizon used in the MATLAB optimization function and the execution horizon used in the TRNSYS "virtual building" are both 24 hours. In a real building, where actual ambient temperature and load profiles can be very different than predicted a day ahead, the execution horizon would typically be shorter. For an example, in the experimental work on MPC, Gayeski et al. (2012) used 24-hour planning horizon, but the cooling rate for only the following hour was applied. The 24-hour-ahead optimization was repeated after each hour, using the updated information for the weather forecast, internal loads and building response.

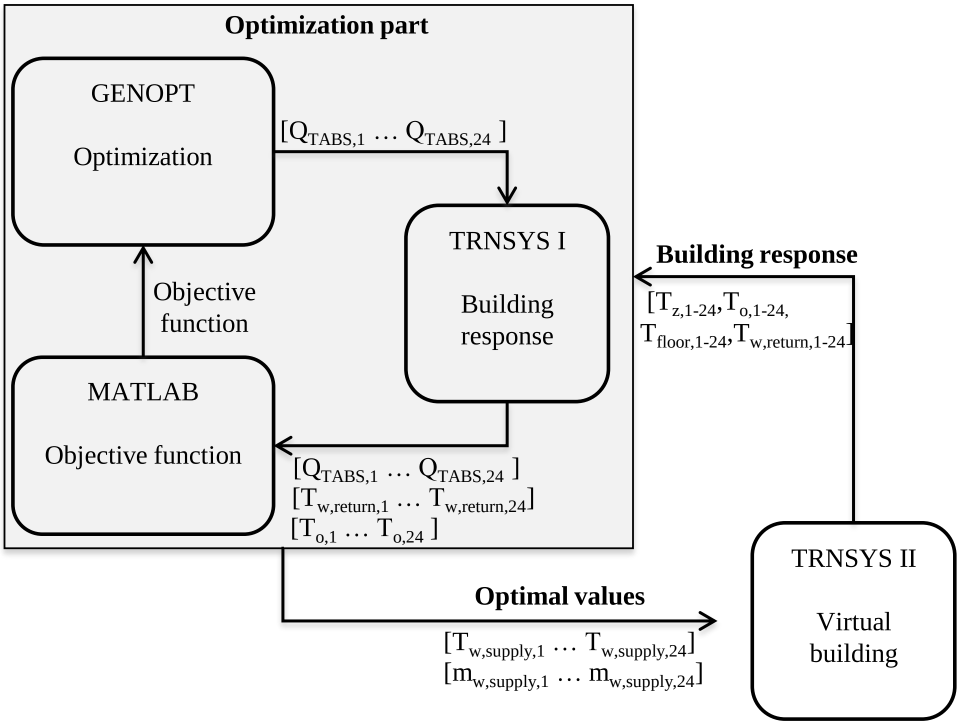

Figure 4.1 – MPC algorithm setup A

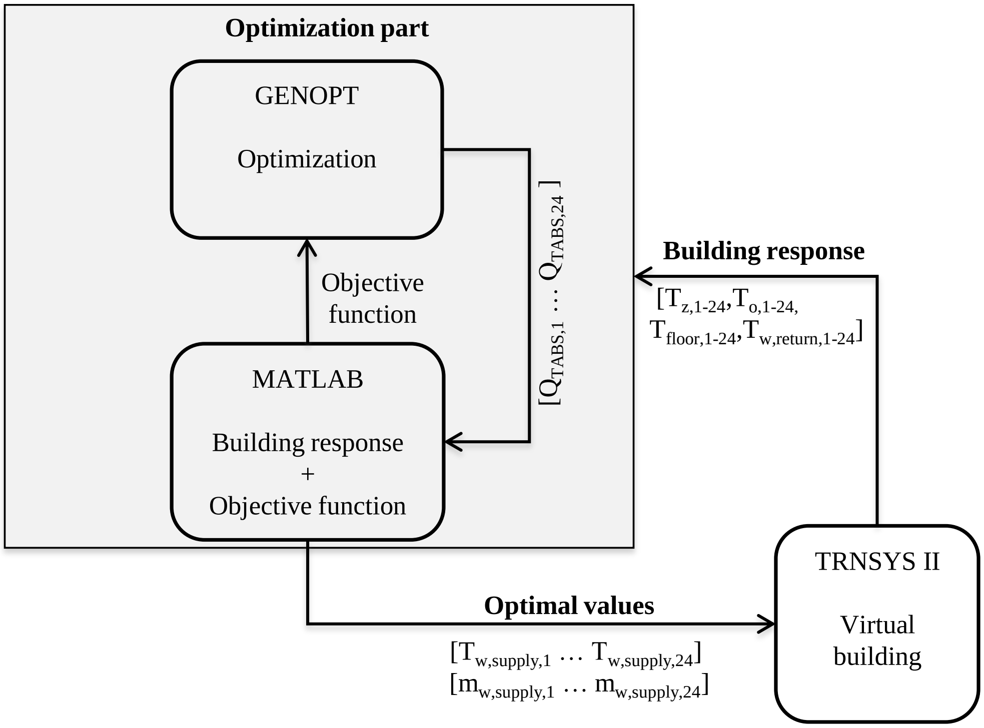

Figure 4.2 – MPC algorithm setup B

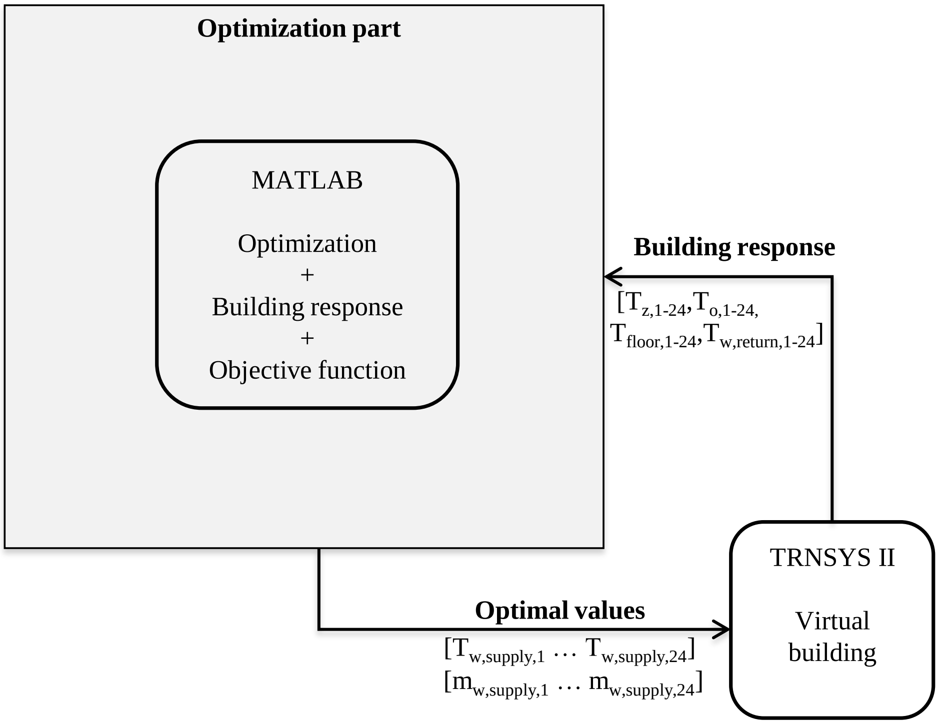

Figure 4.3 – MPC algorithm setup C

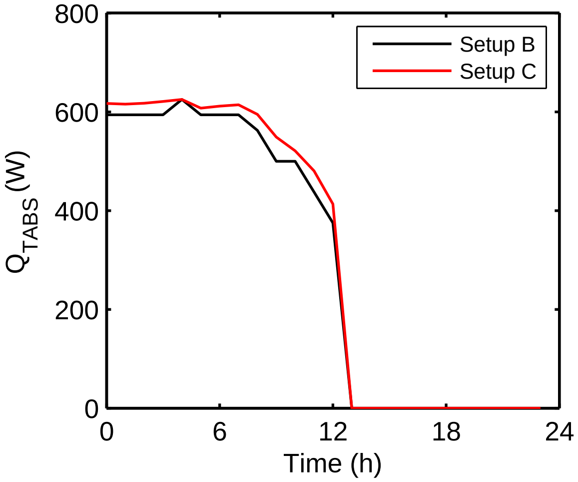

Figure 4.4 – Optimized TABS cooling rates using setup B (black) and setup C (red)

4.3 Optimization objective function

For each day the MATLAB function optimizes 24-hour-ahead cooling rates using the objective function:

$$OF = P_{hp} + P_{trans} + T_{penalty} \tag{4.1}$$

where

$$P_{hp} = Q_{cc} COP \left(Q/Q_{max}, T_{fluid,e,in}, T_{fluid,c,in}\right) \tag{4.2}$$

if $T_o < T_{llim}$

$$T_{penalty} = F_{penalty} \left(T_{llim} - T_o\right)^2 \tag{4.3}$$

if $T_o > T_{ulim}$

$$T_{penalty} = F_{penalty} \left(T_o - T_{ulim}\right)^2 \tag{4.4}$$

The objective function is a sum of the cooling power P_{hp}, transport power P_{trans} required to deliver air/water to each zone, and the temperature penalty $T_{penalty}$ related to thermal comfort.

The penalty factor $F_{penalty}$ is the penalty for the operative temperature existing outside the given limits. When choosing the appropriate penalty factor, the amount of energy cost added to the penalty function (for the excursion just outside the comfort bounds) should be larger than the energy cost required to run the chiller to prevent that excursion (Gayeski, 2010). The chiller used in the MPC analysts consumes approximately 200 W at the lowest compressor speed, under the most conditions. Therefore, $F_{penalty}$ = 800 W/K^2 means that when the operative temperature drifts 0.5 K outside the comfort region, the cost of running the compressor will be lower than letting the temperature drift any further.

4.3.1 Cooling power

The largest power consumption in building cooling systems is for the heat pump, with the heat pump COP being a function of part-load ratio, evaporator air/water inlet conditions and condenser water/air inlet conditions. In the literature, it is common to find HVAC system analyses that are using a constant COP. This simplification might be acceptable for certain analyses, for example, when comparing energy consumption of different building facade, or shading options. However, when using MPC to minimize the cooling energy, a constant COP would not give the optimal solution since it would not capture significant changes in the chiller performance depending on the temperatures and part-load ratios. Manufacturer's heat pump data are very limited, usually specified as an energy efficiency ratio (EER) evaluated at a single operating condition, or a seasonal energy efficiency ratio (SEER) evaluated for single indoor and range or outside temperatures. However, for the energy efficient radiant system that operates at lower part-load ratios most of the time, these data are not sufficient. Also, it is shown in Zakula et al. (2012) that the modest over-sizing of a heat pump can be desirable, which suggests that even conventional systems could benefit from detail heat pump performance data.

Heat pump performance maps were created from the heat pump static optimization results both for the water-to-air heat pump serving TABS, and the air-to-air heat pump serving the VAV system. The static optimization data are then approximated with polynomial curves to reduce computational time. The MATLAB toolbox function LinearModel.stepwise was used for linear regression. The function starts with an initial model (a third- or fourth-order polynomial in this case) and systematically determines which terms in the model can be neglected, based on their statistical significance. The heat pump curve fits are given in Appendix D.

For the water-to-air heat pump, a polynomial of the third order was fitted to specific power (1/COP) curves. It was found that the specific power data were easier to fit than the COP data. The fitted specific power polynomial is a function of the part-load ratio (Q/Q_{max}), outside temperature, T_x, and water return temperature $T_{w,return}$. Figure 4.5a shows the results of the static optimization (black) and fitted values (red) for a single water return temperature. When the outside temperature is lower than the water supply temperature, the heat pump could run in the economizer mode, with the compressor turned off. However, as shown in Chapter 2, it is not straightforward to assume that the economizer mode will always give lower power consumption. Therefore, an additional polynomial of the fourth order was fitted for the economizer mode. Different than before, the COP values were easier to fit than the specific power data for the economizer mode (Figure 4.5b). When the outside temperature drops bellow the water supply temperature, the optimization function evaluates the COP for both the compressor-on and economizer mode, and decides which one consumes less power.

The results for the air-to-air heat pump optimization in Chapter 2 were shown for the sensible cooling only. Since the assumed supply conditions for the VAV system are 12.5°C and 9 g/kg absolute humidity

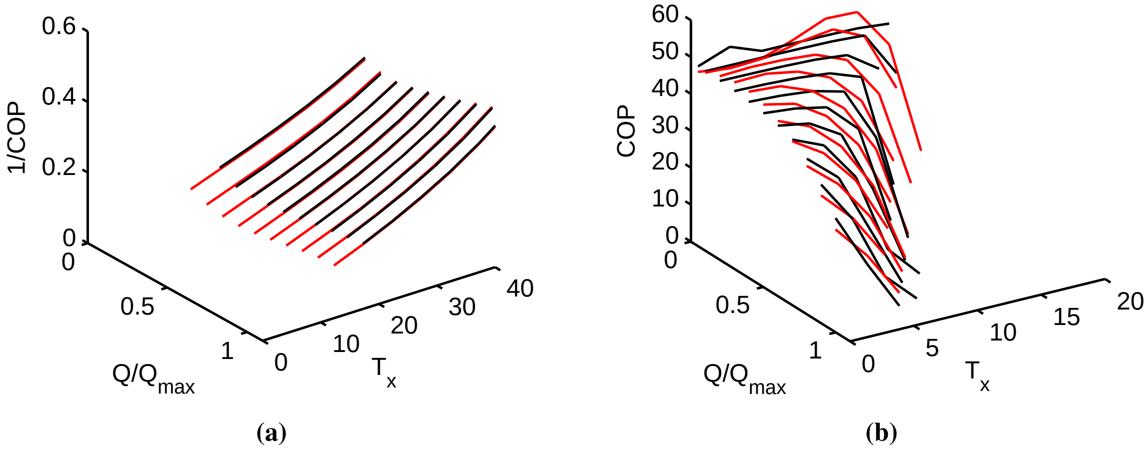

Figure 4.5 – (a) Third-order polynomial fit (red) to optimized specific power (black) in compressor-on mode and (b) fourth-order polynomial fit (red) to optimized COP (black) in economizer mode. Results are shown for water-to-air heat pump, and water return temperature of 17°C.

(saturated state), both sensible and latent loads can occur on the cooling coil. Also, the supply airflow rate in the VAV system is determined by loads in the zone and therefore, cannot be optimized. The wet coil model for partially, or fully wetted surface was developed according to Threlkeld (1970). For given evaporator inlet conditions, airflow rate and desired evaporator outlet conditions, the model calculates the required evaporating temperature and ratio of evaporator surface where latent loads are removed.

The air-to-air heat pump performance map was created for a range of evaporator inlet air temperatures and humidities (Figure 4.6), and condenser inlet air temperatures. The evaporator airflow varied from 0.05 to 0.1 m^3/s, while the condenser airflow was optimized for the lowest heat pump power consumption. Figure 4.7 shows the specific power (1/COP) as a function of the outside temperature T_x, and part-load ratio Q/Q_{max}. The cooling rate Q represents a sum of both sensible and latent loads on the cooling coil, and is, therefore, influenced by evaporator inlet air flow temperature and humidity. Similarly as for the water-to-air heat pump, the linear regression is used to fit a third-order polynomial to the optimized specific powers, as shown in Figure 4.8.

Details on the polynomials for water-to-air and air-to-air heat pump can be found in the Appendix D.

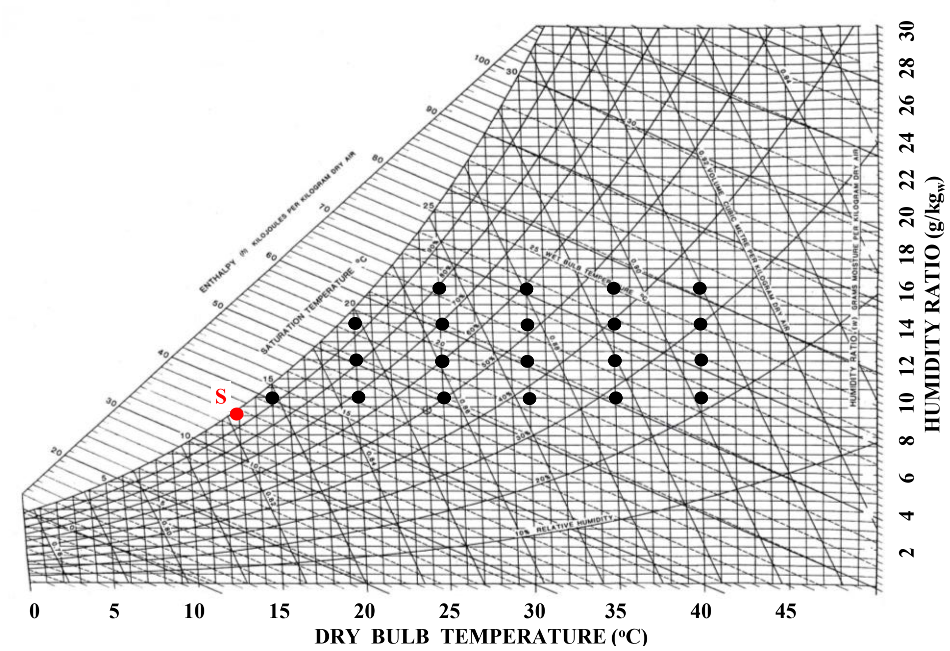

Figure 4.6 – Evaporator inlet air temperatures and humidities for air-to-air heat pump static optimization

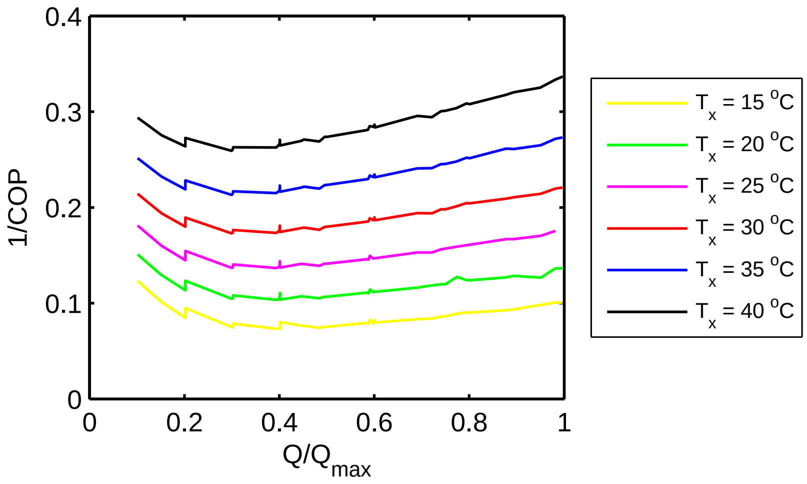

Figure 4.7 – Optimized air-to-air heat pump specific powers for supply temperature of 12.5°C and a range of part-load ratios Q/Q_{max}, and outside temperatures T_x

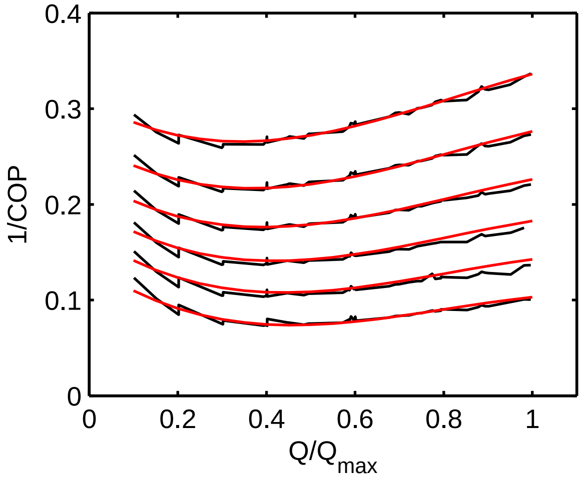

Figure 4.8 – Third-order polynomial fit (red) to optimized air-to-air heat pump specific power (black)

4.3.2 Transport power

One of the important advantages of water systems compared to all-air systems are the significant savings achieved through a reduction of transport power. Moreover, it is reported in Krarti and Henze (2005) that excluding the transport power from MPC optimization can influence the optimization results, and the related cost savings. Therefore, the MPC objective function used in this work accounted for both the cooling and transport power.

The transport power P_{trans} is a function of a fan/power characteristic, flow rates and total pressure losses throughout a building. The limitation for the fan power as a function of the design airflow rate is given in ASHRAE Standard 90.1 (ASHRAE, 2004) as 2.7 kW/m^3/s. This information was used to calculate the design point fan power for the VAV and ventilation system. For the radiant cooling system, which operates with constant water flow rates, the assumed transport power was 355 kW/m^3/s. This value was available from data for one of the Boston University buildings (Blum, 2013). For the comparison, the specified supply fan power in the design point was 2.63 kW/m^3/s in the real building, very close to the Standard 90.1 limitation.

For the VAV systems, an additional correlation was needed to calculate the fan power at airflow rates different than designed. While the airflow rates in the VAV system vary depending on the building loads, the ventilation system is mostly designed as a constant air volume system, sized to deliver fresh air to each zone. However, for a building with occupancy sensors, or where a ventilation system is controlled based on a zone's humidity sensor, designing a variable air volume ventilation system could result in fan power savings. Since further analysis assumed variable air volume ventilation system, the additional correlation for off-design airflow rates was used for the ventilation system as well.

The first correlation for a fan power as a function of off-design flow airflow rates was a simple, and often used fan power law $Power = Constant(Airflow^3)$. However, the use of this correlation led to illogical results when comparing the VAV and ventilation system transport powers. For example, the design airflow rate for the ventilation system was about four times smaller than for the VAV system, and the design powers for both systems were scaled accordingly. However, for the ventilation system design airflow, the VAV system fan power was sixteen times smaller than the ventilation fan power. Since the VAV system was sized for the four times larger design airflow rate, and due to the cubic relation between the power and airflow at off-design conditions, the VAV system power was almost negligible for airflow rates at which the ventilation system was operating.

As explained in detail in Englander and Norford (1992), the power for centrifugal devices varies as a cube of the flow only in cases where the pressure is solely a function of a flow. For these cases, the power goes to zero as the flow rate goes to zero, and can be described with the simple power law. For example an exhaust fan is controlled based on the airflow, and needs to overcome only losses in the exhaust duct. However, for devices that are pressure-regulated, and have a certain pressure to overcome, the fan power does not go to zero as the airflow goes to zero, but instead has a certain offset. Assuming a simple cube correlation and the zero power under no-flow conditions can significantly underestimate the power at low flow rates, as shown in Figure 4.9. An example is a HVAC supply fan that has setpoint static pressure to overcome. Englander and Norford (1992) developed a correlation (Equation 4.5) for the dimensionless fan power P/P_{design}, a function of the dimensionless pressure setpoint p_{set}/p_{design}, and the dimensionless airflow rate V/V_{design}. The correlation showed extremely good predictions when compared to experimental measurements for a VAV supply fan.

$$\frac{P}{P_{design}} = \left[1 - \left(\frac{1}{2}\frac{p_{set}}{p_{design}}\right)^{1.5}\right]\left[\left(1 - \frac{p_{set}}{p_{design}}\right)\left(\frac{V}{V_{design}}\right)^{2} + \frac{p_{set}}{p_{design}}\right]\frac{V}{V_{design}} + \left(\frac{1}{2}\frac{p_{set}}{p_{design}}\right)^{1.5} \tag{4.5}$$

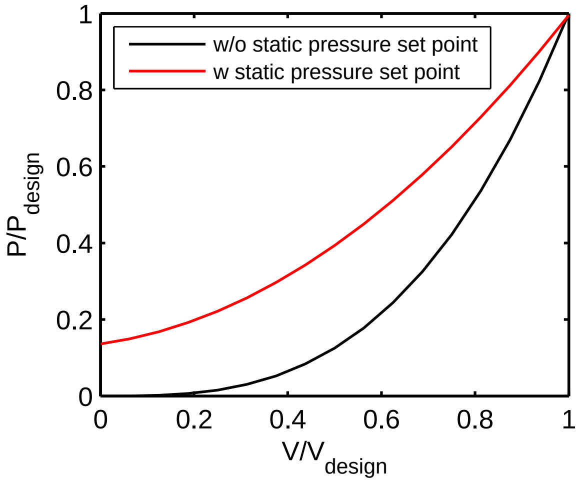

Figure 4.9 – Dimensionless fan power versus dimensionless air flow relation for VAV and ventilation system supply fan, with (red) and without (black) static pressure setpoint

Since a detailed air distribution system has not been modeled, the design point static pressure was calculated from another simulation. The simulation was done by Blum (2013) for the same Boston University building mentioned before, and was validated using the measured data. The model included a detailed distribution network of ducts and dampers, and assumed static pressure setpoint of 1.5 in wg. When Equation 4.5 was implemented, the ventilation system fan power was only 10% higher than the VAV system fan power at the same airflow (design airflow for ventilation). Slightly higher power for the ventilation fan was expected, since the VAV fan was sized for the larger design airflow rate.

Compared to supply fans, return fans have lower power at design conditions due to lower pressure drops in return ducts. Furthermore, they are usually controlled based on the flow, rather than the pressure setpoint, having a zero power for no-flow conditions. Therefore, the return fans for the VAV and ventilation systems were modeled using the simple fan law. The return fan powers at the design conditions were scaled as 40% of the supply fan power, based on values from the Boston University building. In a real building, the return airflow would be somewhat lower than the supply airflow due to building air leaks and pressurization. Since details on building leakiness and fan controls are not considered in this work, the return airflow was assumed equal to the supply airflow.

4.4 Conclusion

The model predictive control algorithm was developed combining the optimization function in MATLAB and the TRNSYS model for a "virtual building." Two additional modeling approaches were described, but were abandoned due to model complexity, issues with initialization of variables, and computational speed.

The MATLAB optimization function uses the pattern-search optimization algorithm to find the optimal cooling rates over 24 hours, based on a predicted weather and internal gain forecast. The objective was to minimize the daily cooling and transport energy consumption, while maintaining the comfort for the occupants. The building thermal and hygric responses are captured through the inverse building model described in Chapter 3. The heat pump optimization is performed for the water-to-air and air-to-air heat pump, and is decoupled from the building optimization. When the outside temperature is lower than the water supply temperature, the power for the water-side economizer mode is calculated, and compared to the compressor-on mode to determine which one is more economical.

After the optimization, the optimal values are sent to the "virtual building," modeled in TRNSYS. Although slower than the inverse model, the TRNSYS model allows to predict the building response with better accuracy. The TRNSYS model outputs, mainly temperature and humidity responses, are used in the next optimization step, since the inverse model requires the knowledge of the building's thermal and hygric history. The planning and execution horizon are both 24-hours, assuming perfect weather and load predictions. In a real building, the execution time would be shortened to account for unexpected changes in weather forecast, internal loads and building responses.

The transport power for supply fans could not be accurately modeled using the simple fan law, in which the power goes to zero for no-flow conditions. When comparing the VAV system fan power with the ventilation system fan power for the same airflow rate, this formulation resulted in unreasonably smaller powers for the VAV system fan. The problem emerged from the fact that the pressure-controlled centrifugal devices, in which the fan power is not a function of airflow only, do not have zero power at no-flow conditions. Therefore, VAV and ventilation system supply fan powers were calculated using the correlation that accounts for the static pressure setpoint (Englander and Norford, 1992). The simple fan law is still used for the return fans, which are flow-controlled devices and hence, have zero power at no-flow conditions. The return fan powers in the design point are assumed 40% of the supply fan power, accounting for lower pressure losses in the return ducts. The TABS system is assumed to have a constant water mass flow rate, resulting in the constant pump power.

Chapter 5

Dehumidification and ventilation system

For all-air systems, the room temperature, humidity and ventilation rates are all controlled through the supplied air, and are therefore strongly influenced by the supply conditions. In multi-zone buildings, in which the supply conditions are determined based on a critical zone, it can be difficult to maintain both the desired temperature and humidity in individual, non-critical zones. Moreover, in most cases different zones have different ventilation needs, and the ratio between the return and fresh air is determined based on a zone with the highest needs. This causes other zones to have larger amounts of fresh air than needed, and increases the energy consumption.

Decoupling the sensible (temperature) control from the latent (humidity) and ventilation control was suggested for the improved indoor air quality (IAQ) and energy savings (Coad, 1999, Mumma, 2001, and Fischer and Bayer, 2003). In a decoupled system, ventilation and humidity are controlled by a dedicated outdoor air system (DOAS), which can also deliver a certain amount of sensible heating/cooling. The remaining sensible loads are met by a parallel system.

Most of the work found in the literature is focused toward analyzing the possible benefits of a typical constant air volume DOAS with an air-cooled heat pump, and with or without an enthalpy wheel. Although Gatley (2000) proposed promising alternatives to the typical DOAS, an additional analysis is needed to determine their feasibility for different scenarios.

This chapter describes several dehumidification strategies considered to be used in combination with TABS system and predictive control. Their common goal is to improve the performance of DOAS heat pump, which could potentially reduce the total energy consumption. To understand which strategies would perform better under certain conditions, their performance is compared across different climates in Chapter 6.

5.1 Literature review

A thorough analysis of design considerations, advantages and possible disadvantages for a DOAS can be found in numerous papers by Mumma. Based on different DOAS supply air temperatures, Shank and Mumma (2001) analyzed the capital and operating cost for the parallel sensible cooling system (chiller and terminal coil equipment). In the proposed system, the outside air first passes through the enthalpy wheel, gets cooled to the dew-point temperature of approximately 7°C, and is reheated to the supply dry-bulb temperature of 13°C using the sensible wheel. When delivering the same amount of outside air, DOAS showed to be a promising technology compared to a conventional all-air system, based on the annual performance results for Atlanta (Mumma and Shank, 2001). However, Mumma (2010) also pointed out the importance of building pressurization for indoor air quality and mechanical equipment loads, as well as the problem of reduction in the enthalpy wheel efficiency for unbalanced flows. The analysis showed that for an office building with a leakage rate of 5 $m^3/(hm^2)$ at 50 Pa, and with ASHRAE Standard 62.1. ventilation requirements, the ratio of the pressurization flow to the total ventilation flow rate should be around 0.7 to achieve adequate pressurization.

Gatley (2000) gave a detailed overview of different dehumidification options and suggested several energy efficient alternatives to conventional reheat coils, such as coil-loop run-around, heat-pipe run-around, air-to-air heat exchanger, rotary-wheel heat exchanger, and the arrangement in which, after passing through the condenser, the refrigerant passes through an additional coil used to transfer heat from the refrigerant to the air. In this way the refrigerant is subcooled, resulting in an increased enthalpy difference on the evaporator.

Mumma (2002) analyzed DOAS in a combination with metal ceiling radiant cooling panels (CRCP). The condensation on the ceiling was prevented by maintaining the water inlet temperatures above the room dew-point temperature. The cost analysis showed that this system can have lower both the capital and operating cost compared to a conventional VAV system, mainly due to cost savings for the chiller and ductwork, as well as a required fan energy. Jeong et al. (2003) compared a conventional VAV system with an air-side economizer, to the proposed system. The proposed system had CRCP sized to meet sensible loads, and a parallel, constant air volume DOAS sized to meet full latent, and a part of sensible loads. For small cooling loads, both latent and sensible loads were met solely by DOAS. As the load increased, DOAS supply temperature dropped until reaching the lower limit of 11°C. If the zone set point temperature was still not met, the radiant cooling system was turned on, and the water supply temperature was controlled to meet the remaining sensible loads. Compared to the VAV system, savings were 42% for the annual energy consumption and 50% for the peak energy. Jeong and Mumma (2003) also analyzed the influence of a convective heat transfer coefficient on the radiant panel cooling capacity. Although mixed convection (natural and forced) significantly enhanced a panel cooling capacity, the impact was small for discharge air velocities less than 2 m/s. In subsequent work, Mumma and Jeong (2005b) gave control recommendations for the parallel DOAS and CRCP system. While testing the proposed control strategy in the real building, with the DOAS supply air temperature of 17°C, average CRCP temperature 16°C, room dry-bulb temperature 23°C and room dew-point temperature 12°C, the thermal comfort analysis showed very low Predicted Percent Dissatisfied (PPD) of 5% (Mumma and Jeong, 2005a).

Emmerich and McDowell (2005) performed a simulation study of a two-story office building over five U.S. climates, with and without DOAS. The analysis was done by combining TRNSYS for the building response and CONTAM for the infiltration and inter-zonal airflow. Compared to the base case, adding DOAS resulted in 14–37% annual energy cost savings. However, although DOAS had cooling coils intended to fully meet latent loads, a certain amount of latent cooling was still occurring on the parallel system. This suggests that designing DOAS to provide only ventilation requirements can potentially cause condensation issues for the radiant cooling systems.

Similar cost savings for the combined radiant-DOAS system were shown in the field demonstration for the school in Florida (Khattar et al., 2003). In addition to an ice-storage system, the system had separate conditioning for the recirculation and ventilation air, with the ventilation air being cooled to lower temperatures (6°C) for dehumidification purposes. Compared to the school of a similar size and use, and with a conventional VAV system, the cost savings were 22%, with only 1% increase in the capital cost. It is also reported the the school with DOAS had much better humidity control.

For a typical office building in Denver, Colorado, Moore (2008) analyzed a hydronic radiant system in slabs, combined with DOAS and a cooling tower. The system saved around 60% energy over the whole cooling season, compared to a conventional VAV system with an air-side economizer. The reported Predicted Percentage of Dissatisfied (PPD) was below 10%.

Stetiu (1999) also compared a combined radiant-DOAS system to a VAV system with an air-side economizer. The analysis for a typical office was performed for a summer week, across 9 U.S. climates, and for different latent fractions of the total cooling energy. To analyze the importance of night humidity built-up, two ventilation strategies were analyzed. The first strategy was ventilation only during day time, and the second was 24-hour ventilation, with lower airflow rates during the night. The results showed that in all climates, even in a humid climate like New Orleans, the radiant coiling system with the supply water temperature of 20°C was able to maintain the indoor temperature within comfortable 24°C, and without condensation problems. For two locations (Phoenix and Salt Lake City), 20°C water supply temperature was not low enough to maintain the room at 24°C, and needed to be lowered to 17.5°C. However, since both climates are relatively dry, condensation was not an issue. Between the two ventilation strategies, the continuous ventilation is recommended for humid climates, and the interrupted ventilation strategy for dry climates. It was shown that the combined cooling system uses less energy compared to the all-air system for all climates, even with the continuous ventilation. The energy and the peek power savings were 17 – 42% and 22 – 37% respectively, with lower savings corresponding to cold, moist climates with better potential for an air-side economizer. However, this analysis assumed a constant COP, and did not take into account a water-side economizer.

Although one of the advantages for all-air systems is a good potential for an air-side economizer, radiant systems have a good potential for a water-side economizer due to higher water supply temperatures. This was considered only in two analyses found in the literature (Tian and Love, 2009a, and Niu et al., 1995). For a multi-zone building, Tian and Love (2009a) analyzed a VAV system with an air-side economizer, and a radiant-DOAS system with a water-side economizer that utilizes a cooling tower. Similar to Stetiu (1999), they compared the continuous DOAS operation and the operation with over-night shutdown. The radiant-DOAS system performed better across 16 analyzed U.S. climates, with annual cooling energy savings up to 60% for the night-time shutdown, and 40% for a continuous operation. The largest savings were reported for dry climates (hot and cold), while humid climates had lower savings due to the need for the continuous ventilation for dehumidification purposes. However, they pointed out that in some cases the combined system could have higher energy consumption compared to the conventional VAV system if the water-side economizer is not included. In the subsequent work, Tian and Love (2009b) compared the simulation results to the real measurements for the University of Calgary building. Using the simulation, they managed to overcome certain control issues of the existing building. For example, the combined radiant-DOAS system had higher energy consumption compared to the VAV system, caused by simultaneous heating and cooling. Making simple changes in the control strategy they managed to achieve 50% savings compared to the original operating state of the combined system.

5.2 DOAS configurations

Five dehumidification strategies shown in Figure 5.1 are considered, with the corresponding processes on the psychrometric chart (Figure 5.2). Point X represents outside air conditions, W conditions after the enthalpy wheel, $CC1$ conditions at the cooling coil inlet, $CC2$ conditions at the cooling coil outlet, S supply conditions, and Z zone conditions.

To remove latent loads from a zone, the supply air needs to be cooled to a low enough temperature for moisture removal, and supplied to the room at a low absolute humidity. Since the air cannot be supplied to the zone at the temperature lower than 13°C for comfort reasons, reheat of the supply air is often needed. To avoid additional air reheat that would increase the total energy consumption, it is assumed for all dehumidification scenarios that the air is supplied to the zone with an absolute humidity 9 g/kg, corresponding to the dew-point temperature of 12.5°C. One can argue that the lower dew-point temperature would result in reduced airflows required for dehumidification, and therefore a reduced fan power. However, it would also result in lower heat pump efficiency due to lower evaporating temperature and the need for reheat energy. Hence, a similar analysis as done by Shank and Mumma (2001) could be performed in future work to determine the optimal supply conditions for a particular case.

All strategies utilize the enthalpy recovery wheel, as an efficient way to recover sensible and latent heat from the return air. Although wheel efficiency will depend on its size relative to the airflow, performance characteristic, and the rotational speed, it will be assumed that the total sensible and latent heat recovery efficiency is 0.8. Furthermore, it is assumed that the wheel operates only if the outside air enthalpy is higher than the return air enthalpy. Since an enthalpy recovery wheel needs a balanced flow for an efficient operation, an additional consideration is the reduction of return air due to the need for building pressurization (Mumma, 2010). The reduction can vary significantly depending of the building leakiness and wind conditions, details of which are not considered in this analysis. Therefore, a parametric study will be performed in Chapter 6, with 100% and 50% of the return air compared to the supplied air.

System A is a typical DOAS found in a majority of analyses of a combined radiant and DOAS. The system consists of an enthalpy recovery wheel and a cooling coil, with the heat being rejected to the outside air.

System B represents a similar configuration, but with the heat being transferred to the supply air stream. This configuration could possibly improve the heat pump COP due to lower condenser air temperatures. Although this will add sensible loads to TABS system, it is expected that the radiant system can remove those loads more efficiently during the night precooling. Cases where adding heat to the supply stream would not be feasible are buildings with very high sensible gains. Because the floor temperature is limited for thermal comfort reasons, the radiant system can provide a limited amount of cooling, usually around 50 W/m^2. This suggests that in buildings with higher sensible loads, adding an additional sensible load to the radiant system might be undesirable. However, in most high-performance buildings, with efficient appliances, and with heat transfer through the envelope significantly reduced, heat gains are usually lower than 50 W/m^2.

System C represents a variation of system B, but with a parallel condenser. The first condenser is placed in the supply stream, and the second in the exhaust stream, after the enthalpy wheel. This configuration was considered after experiencing some practical difficulties with system B, as described in more details later in the chapter.

System D also assumes the configuration with parallel condensers, but with the second condenser placed outside. Although this configuration will on average result in higher condenser inlet air temperatures than for system C, it will also allow for higher, optimized condenser airflow rates.

System E is a variation of system A, with a run-around heat pipe used to precool the air before entering the evaporator. This can, again, have positive implications for the COP due to lower evaporator inlet air temperatures. Similarly as for the enthalpy wheel, it will be assumed that the heat pipe has a constant efficiency of 0.5 (Wallin et al., 2012). The ventilation system analyzed by Wallin et al. (2012) had one coil placed in the supply air stream and the other in the exhaust stream. The experimental results for Stockholm and Berlin showed 47% annual heat recovery using the run-around coil.

Another promising strategy, not analyzed in this work, would be to use a small indoor unit (direct expansion system) for dehumidifcation purposes, also providing a certain amount of sensible cooling. To satisfy dehumidification needs when latent loads are high, a DOAS needs to supply more air to the building than required for breathing. With the direct system running to remove latent loads, only a minimum amount of fresh air would be supplied though the duct system, reducing the transport energy. Furthermore, DOAS needs to deliver a certain amount of air during night time to remove latent loads caused by infiltration. The direct system would enable dehumidification without delivering outside air to the zone during night time. This would reduce transport energy, and energy required to condition the outside air to zone conditions.

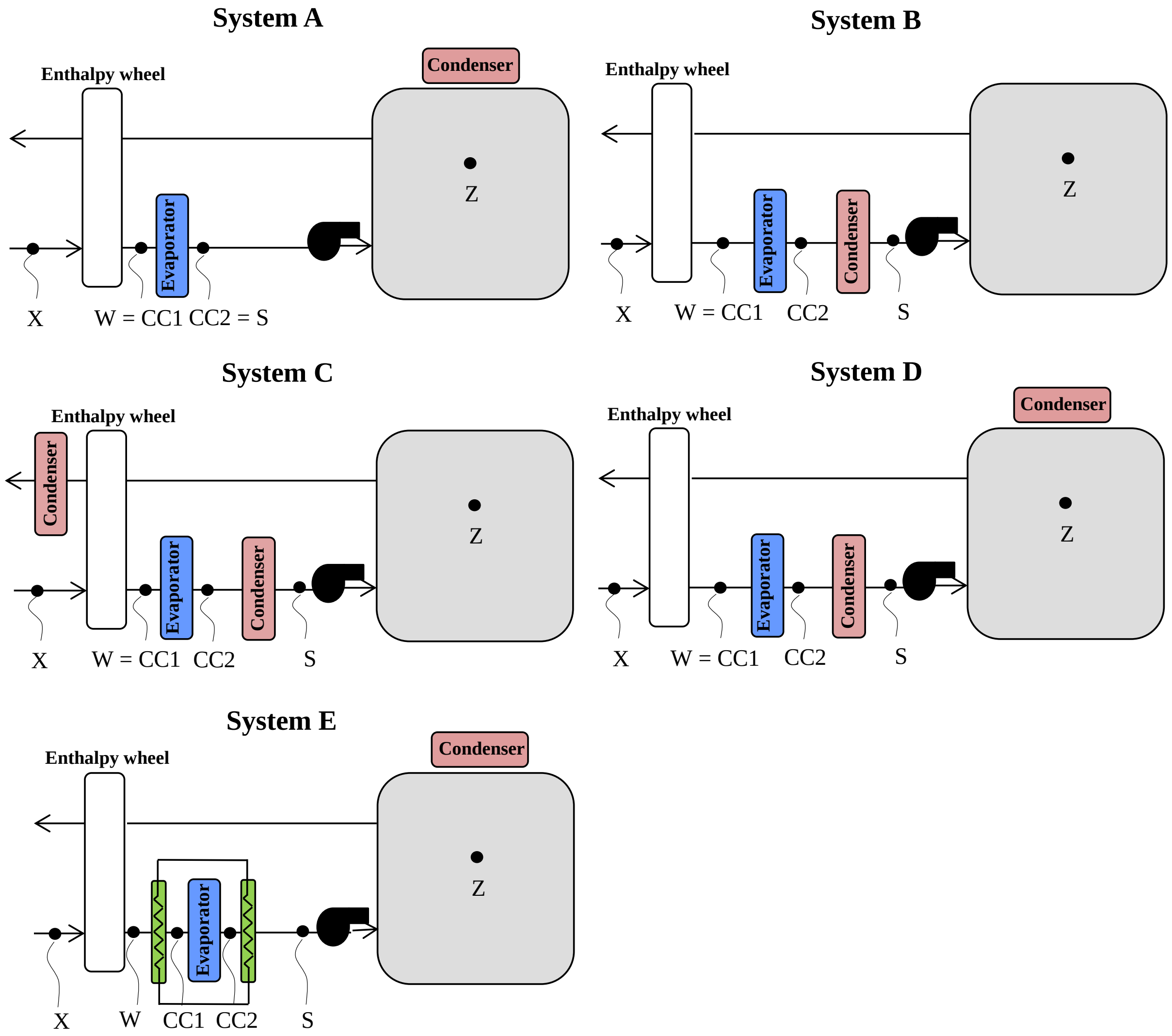

Figure 5.1 – DOAS configurations

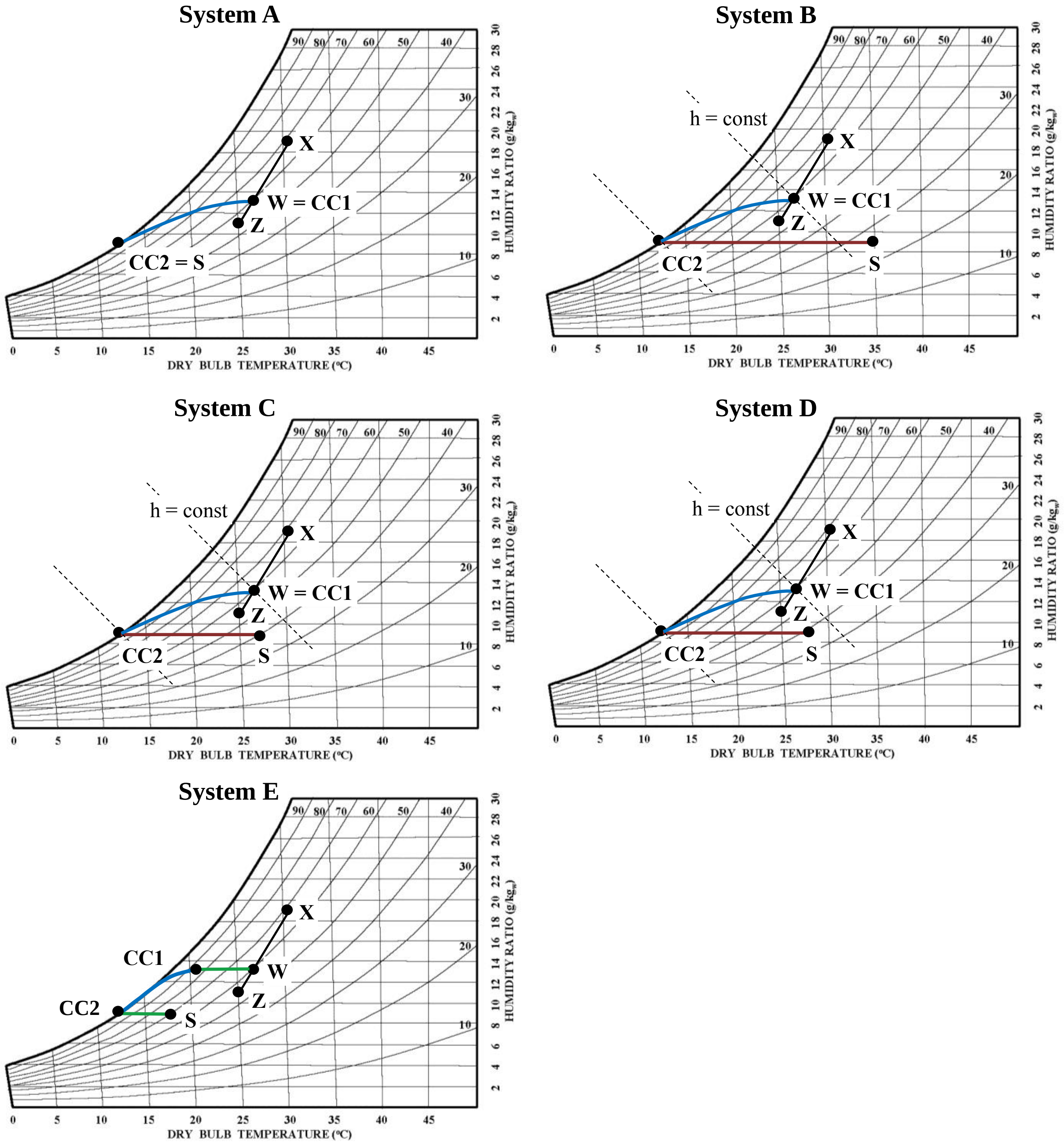

Figure 5.2 – DOAS configurations in psychrometric chart

5.2.1 Heat pump performance maps for different DOAS configurations

To calculate the energy required for conditioning of the outside air to the supply conditions, the MPC algorithm uses the curve fits to the heat pump static optimization data, as explained in Chapter 4. System A uses the same performance map as shown in Chapter 4 for the VAV system (Figure 5.3). The heat pump map is created over a range of inlet temperatures and humidities, assuming the supply temperature of 12.5°C, and the condenser placed outside. The condenser airflows are optimized for the lowest heat pump energy consumption.

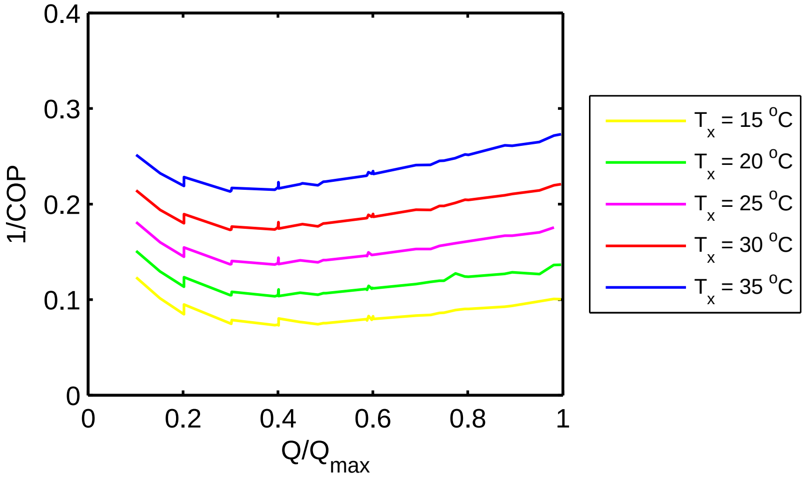

Figure 5.3 – Optimized heat pump specific power for system A and supply temperature of 12.5°C. Specific power is a strong function of outside temperature T_x.

In system B, the condenser is cooled with the air exiting the evaporator at constant 12.5°C, and the COP becomes a function of the evaporator inlet air temperature and humidity (Figure 5.4). The increase in any of these two variables causes the increase of the cooling coil load, and increase of heat that needs be rejected. Since the condenser airflow is limited (equal to the evaporator airflow), this results in a larger temperature difference across the condenser.

It is shown in Zakula et al. (2012) that the airflow optimization can have a significant influence on the heat pump performance. It is, therefore, not apparent that system B will always have a higher COP compared to System A, despite lower condenser inlet air temperatures. This can be shown by comparing two cases with different evaporator inlet air temperatures (the airflow rate, evaporator inlet air humidity and outside temperature are held constant at V_e = 0.075 m^3/s, w_{cc1} = 0.012 kg/kg, T_x = 30°C). For the evaporator inlet air temperature of 25°C, COP_A = 5.3 versus COP_B = 5.8, but when the temperature increases to 30°C, COP_A = 5.0 versus COP_B = 4.5.

Additional simulations were performed to analyze whether the performance of system B can be improved by increasing the condenser area. However, even with three times larger condenser depth, the improvement in the COP was mediocre due to limited condenser airflows. A more severe issue caused by the limited condenser airflows is an inability to reject all the heat for cases with high cooling loads. Increasing the condenser area can help to a certain extent, but even with an infinite condenser area (Figure 5.5a), the maximum heat that can be rejected is limited by the airflow and temperature difference across the condenser according to the equation:

$$Q_{ideal} = m_{air} c_{air} \left(T_c - T_s\right) \tag{5.1}$$

For the condenser to be in a steady state, the heat transfer across the condenser, the refrigerant-side heat balance, and the air-side heat balance all need to be satisfied. In the case of high loads and limited airflows, even if Equation 5.1 is satisfied by increasing the condensing temperature, it is possible that the refrigerant side heat balance (Equation 5.2) is not satisfied due to the lower latent energy (h_2 - h_3) at high temperatures and pressures (Figure 5.5b). As a result of the discussed issues, system B was abandoned as unfeasible for practical implementation.

$$Q_{refrigerant} = m_{ref} \left(h_{c1} - h_{c3}\right) \tag{5.2}$$

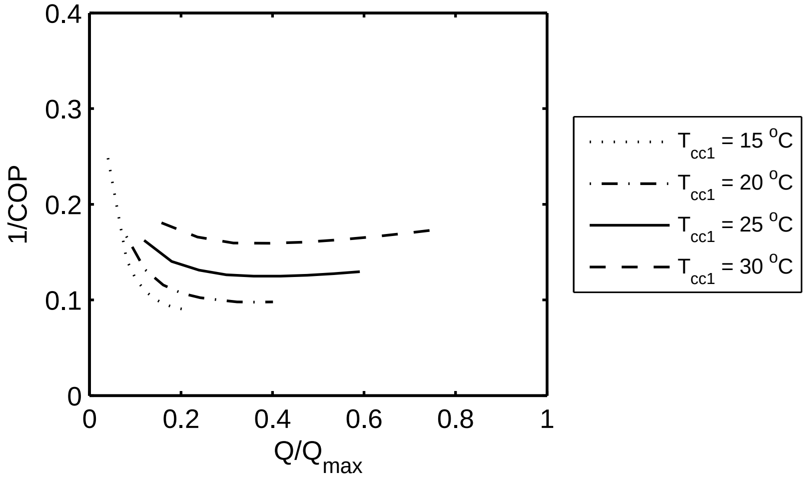

Figure 5.4 – Heat pump pump specific power for system B (shown for w_{cc1} = 0.01 kg/kg). Specific power is a strong function of evaporator inlet temperature T_{cc1}, and humidity w_{cc1}.

System C and system D, both with the parallel condensers, were analyzed with an expectation they would overcome the difficulties experienced with system B. System C has the first condenser placed in the supply stream, and the second in the exhaust stream (after the enthalpy recovery wheel), while system D has the second condenser cooled with the outside air. Although system C has somewhat lower air temperatures on the second condenser compared to system D, it also has limited condenser airflows. Hence, it is not apparent which of the two systems would perform better without performing a more detail analysis.

The same heat pump model as described in Zakula et al. (2011) is used to create performance maps for both systems (Figure 5.6a and Figure 5.8a). For this particular case, the model calculates the right split between the heat exchanged on each condenser. The calculation is done assuming that the con-

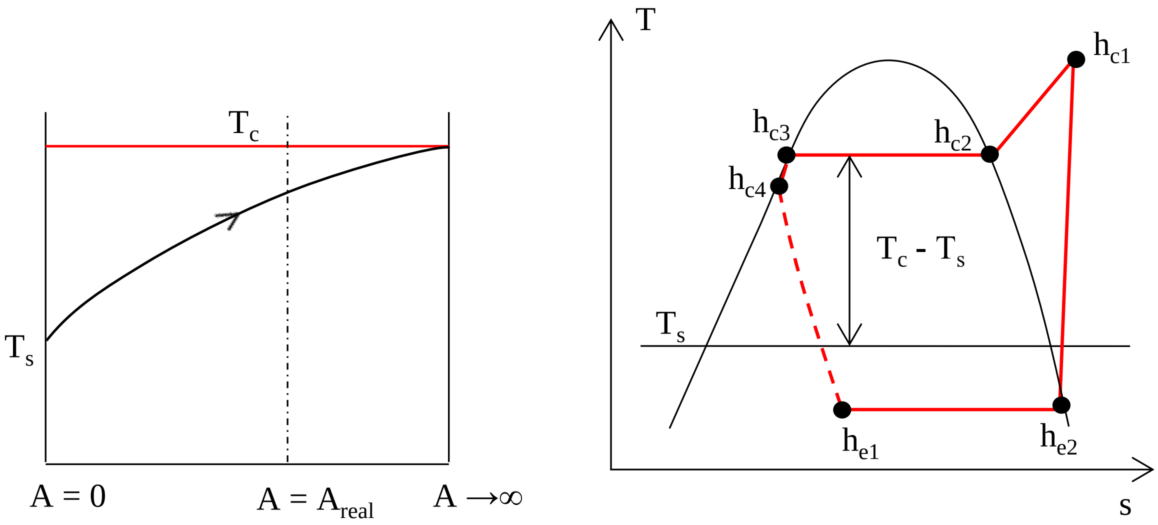

Figure 5.5 – (a) Temperature profiles and (b) cooling process in T-s diagram for the condenser with infinite area

densing pressure in both condensers needs to be the same, since both condensers are served by the same compressor.

The additional important information for systems C and D, which will influence the supply air temperature, is the temperature rise across the first condenser (Figure 5.6b and Figure 5.8b). Depending on the heat ratio rejected by the first condenser, the temperature can be much higher than the supply temperature of 12.5°C assumed for system A.

Polynomials of the third order were fitted to the specific power (1/COP) and temperature increase curves, with fitted values being a function of the part-load ratio Q/Q_{max}, evaporator airflow rate V_e, and exhaust temperature T_{exh} for system B, or outside temperature T_x, for system C. Figures 5.7 and 5.9 show fitted vales (red) to the results of the static optimization (black) for a specific evaporator airflow rate.

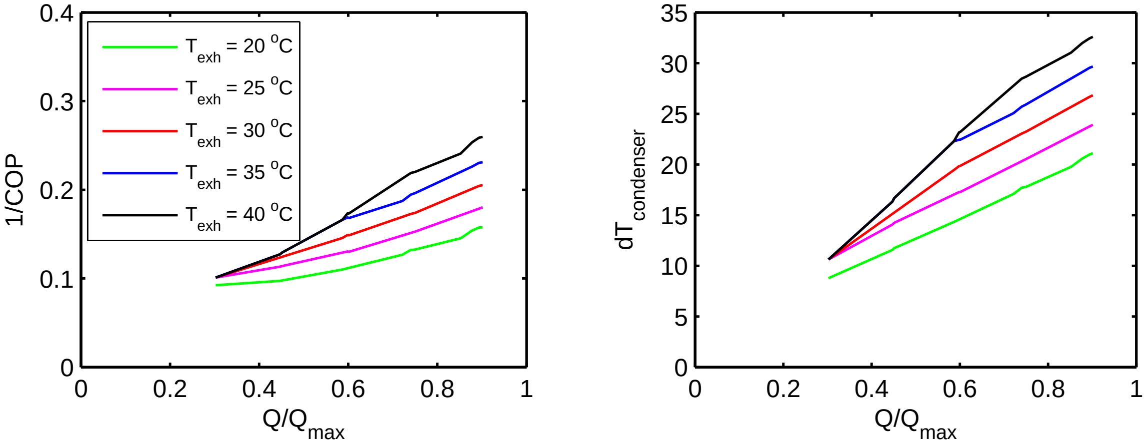

(a) **(b)**

Figure 5.6 – (a) Heat pump specific power and (b) supply temperature increase for system C (shown for evaporator airflow rate $V_e = 0.075$ m^3/s). Specific power and temperature increase are a function of exhaust air temperature T_{exh} and evaporator airflow rate V_e.

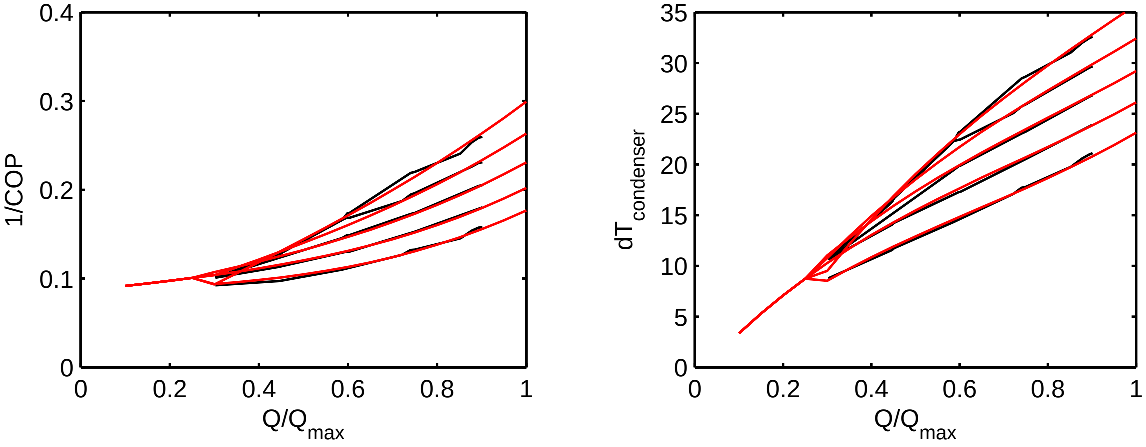

(a) **(b)**

Figure 5.7 – Third-order polynomial fit (red) to (a) specific power (black) and (b) supply temperature increase (black) for system C. Result are shown for evaporator airflow rate $V_e = 0.075$ m^3/s.

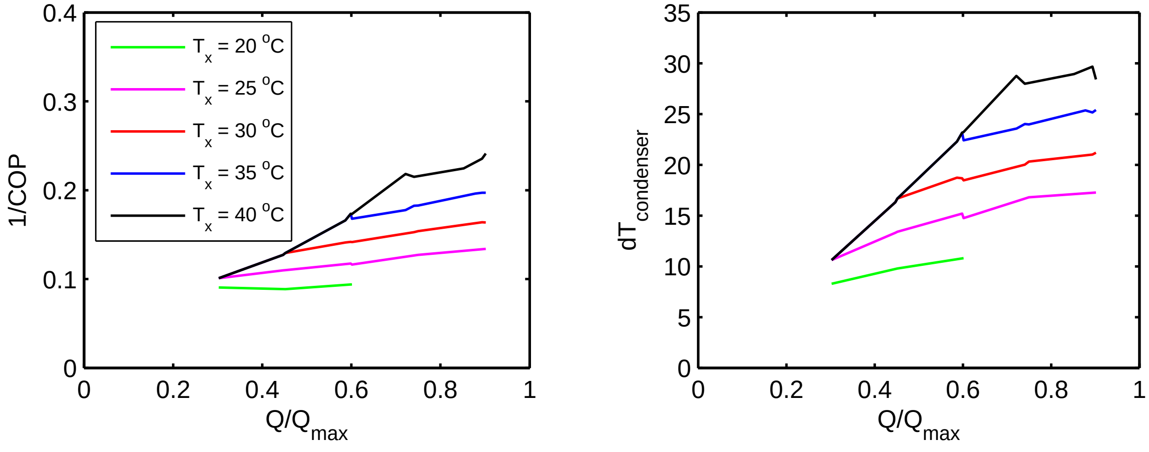

(a) **(b)**

Figure 5.8 – (a) Heat pump specific power and (b) supply temperature increase for system D (shown for evaporator airflow rate $V_e = 0.075$ m^3/s). Specific power and temperature increase are a function of outside air temperature T_x and evaporator airflow rate V_e.

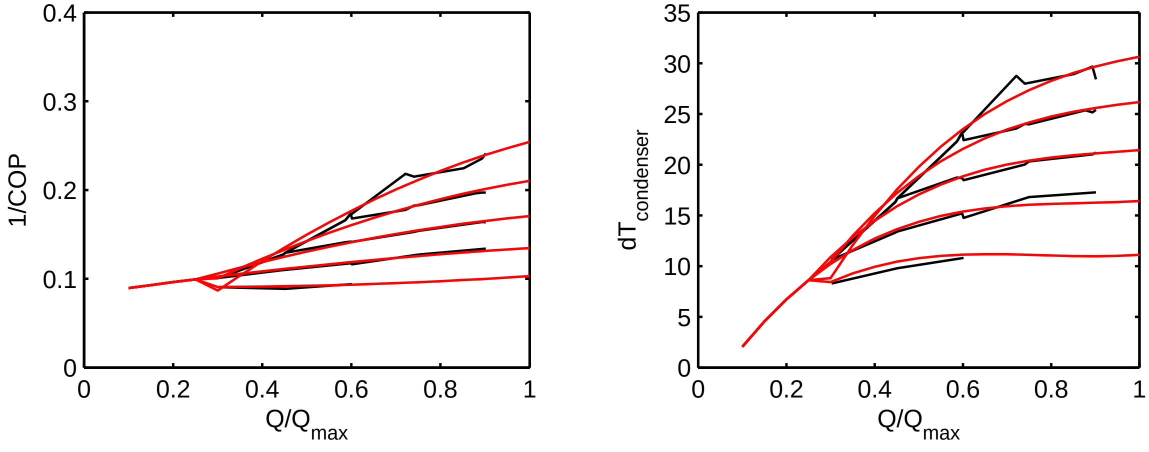

(a) **(b)**

Figure 5.9 – Third-order polynomial fit (red) to (a) specific power (black) and (b) supply temperature increase (black) for system D. Result are shown for evaporator airflow rate $V_e = 0.075$ m^3/s.

5.3 Conclusion

This chapter described several different configurations that are considered for dehumidification and ventilation purposes. The basic variable air volume DOAS assumed the enthlapy recovery wheel, and the heat pump cooled with the outside air. Other options considered more complex configurations with the goal of improving the DOAS heat pump performance.

The system with the condenser placed in the supply stream was found unfeasible for the practical implementation. Although the condenser air temperatures were lower than in the basic DOAS, the condensing refrigerant temperatures were still relatively high due to limited condenser airflows. Moreover, for high loads on the cooling coil, it was not always possible to reject all the heat.

To overcome this problem, the additional two systems assumed parallel condensers, one placed in the supply stream, and the other placed in the return stream after the enthalpy wheel, or placed outside. Although the condenser placed in the return stream has lower condenser air temperatures, it also has limited airflows. On the other hand, the system with the second condenser is placed outside can have higher airflow rates.

The final configuration considered a variation of the basic DOAS, with the heat pipe around the cooling coil. This way, the evaporator inlet temperature would be reduced, improving the DOAS heat pump performance. The increase in the supply air temperature would not be as large as in the previous two configurations, since the entire heat is rejected to the outside air.

The performance of these strategies will be analyzed in Chapter 6 across different climates to gain better understanding as to which strategy would be more suitable for the implementation in the energy efficient cooling system.

Chapter 6

Results

This chapter analyzes the performance of the energy efficient cooling system referred as a low-lift cooling system (LLCS), and compares its energy consumption against a split-system and a variable-air-volume (VAV) system. The comparison with the split-system (direct-expansion system) is useful since the split-system was used in measurements done by Gayeski et al. (2012). Moreover, direct expansion units with a variable refrigerant flow are recently becoming more popular, even for such large buildings as hotels. They can provide both heating and cooling, and can save transport energy compared to all-air systems. The comparison with the VAV all-air system is useful since the VAV system is one of the most commonly used system for heating, ventilation and air-conditioning of commercial buildings. Also, the VAV system was compared with the LLCS in the research study by Pacific Northwest National Laboratory (PNNL) ((Jiang et al., 2007); (Armstrong et al., 2009); (Katipamula et al., 2010)). While the PNNL study assumed the ideal active thermal storage with water, and analyzed different combination of components for the LLCS, this work analyzes the full LLCS described below and building mass acting as a passive thermal storage. Furthermore, this work aspires to identify and separate benefits of model predictive control (MPC) from the use of thermally activated building surfaces (TABS). Finally, four DOAS configurations described in Chapter 5 will be analyzed across different climates. As the ratio of latent to sensible loads increases, the amount of air delivered for dehumidification also increases, removing a larger portion of sensible loads. Therefore, the limiting case will be identified, for which the amount of latent gains becomes large enough for the DOAS to remove all sensible loads in addition to latent.

6.1 Simulation assumptions

The analyses are done for a typical summer week (two weekdays, weekend, three weekdays) from July 15 through July 21, and for some cases over the cooling season from May 1 until September 31. The typical weather conditions across different climates are simulated using TMY3 weather files.

The model of an office room described in detail in Chapter 3 accounts for heat gains from internal loads and through the envelope, while neglecting solar gains. If not specified differently, the peak sensible internal load for the 19 m^2 room is 680 W (2 people each releasing 80 W, 220 W for lights and 300 W for the equipment), or approximately 36 W/m^2. Occupied hours are from 8–18 h, with 66% of the maximum internal loads from 8–9 h, 100% from 9–17 h, and 66% from 17–18 h. The internal gains are modeled as 50% convective and 50% radiative. The only sources of latent gains during occupied hours are loads from people of 0.072 kg/h/person (50 W/person). The internal sensible gains and latent gains are shown in Figure 6.1. Latent loads caused by infiltration are neglected during occupied hours since most commercial buildings are slightly pressurized to avoid infiltration. The ventilation rate used in the analysis for both the VAV and LLCS system is 0.01 kg/s/person (8.5 l/s/person), according to ventilation requirements from ASHRAE Standard 62.1-2007 for office buildings.

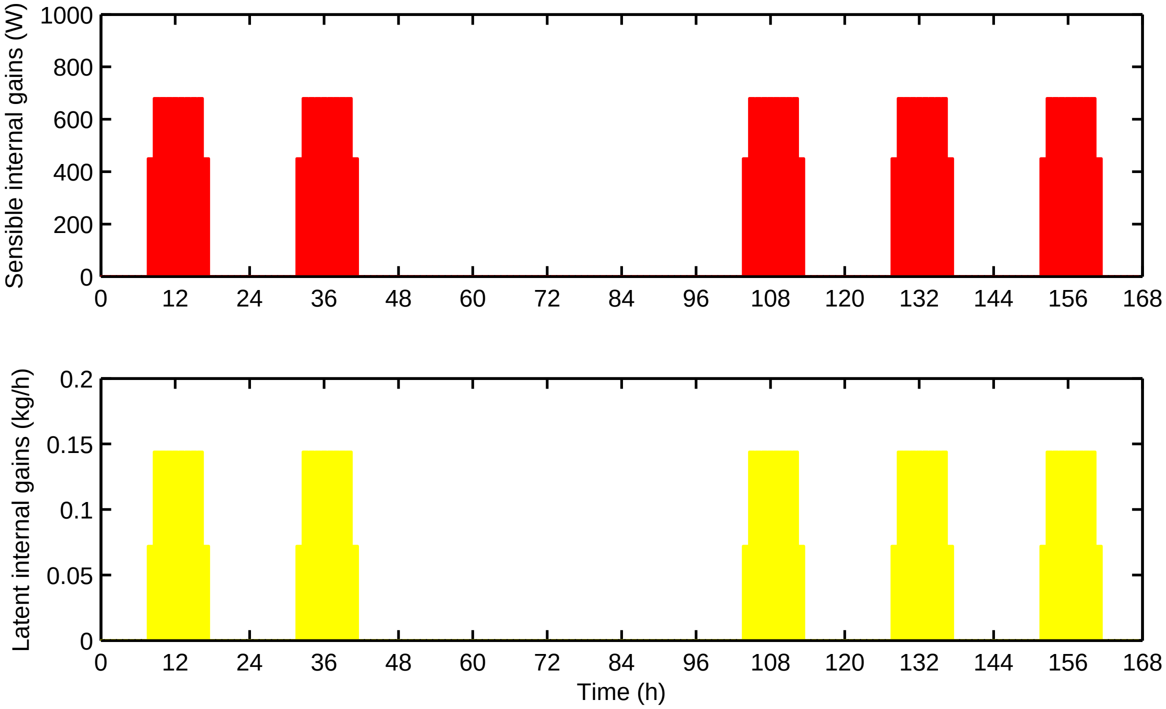

Figure 6.1 – Weekly sensible internal gains (top graph) and latent internal gains (bottom graph)

The LLCS consists of thermally activated building surfaces (TABS), a water-to-air heat pump with variable-speed drive for the compressor, pump and fans, and a dedicated outside air system (DOAS) for ventilation and dehumidification. Sensible cooling through TABS is controlled varying the water supply temperature and pump operation (on/off mode), with the water mass flow rate being constant. The DOAS assumed in this work is a variable-volume system controlled based on a humidity sensor. During operating hours, the DOAS delivers air required for breathing and removal of latent loads. During night time, indoor humidity needs to be controlled to prevent possible condensation on the cold TABS. Hence, the DOAS operates during night delivering airflow rates necessary to remove infiltration latent loads and maintain the desired humidity. The DOAS does not operate during weekends. It is served by a separate air-to-air heat pump, with cooling coil outlet conditions of 12.5°C and 9 g/kg absolute humidity (saturated state). These conditions are chosen based on the two following criteria. First, assuming the zone's humidity setpoint of 11 g/kg, a minimum required amount of fresh air 0.01 kg/s/person, and latent loads of 0.072 kg/h/person, the supply air humidity of 9 g/kg is sufficient for the removal of latent loads using the minimum amount of fresh air required for breathing. Second, the lowest allowed air supply temperature is usually 13 °C for comfort criteria and, therefore, the supply temperature in this work is chosen to prevent the need for an additional reheat. Four different DOAS configurations are analyzed, all utilizing the enthalpy recovery wheel with sensible and latent efficiency of 0.8. The recovery wheel does not operate when the outside enthalpy is lower than the zone's enthalpy. The heat pump performance maps for the water-to-air and air-to-air heat pump are the result of static optimization. Curve fits to static optimization data are used to reduce computational time, as described in detail in Chapters 4 and 5.

The VAV system delivers air at constant 12.5 °C and 9 g/kg absolute humidity (saturated state), and with airflows varied to remove zone's sensible loads. It uses the same air-to-air heat pump performance map as the DOAS, but for the heat pump of a larger capacity. When the outside temperature is higher than the zone's temperature, the minimum amount of fresh air for breathing is mixed with the recirculation air. When the outside temperature drops below the zone's temperature, the VAV system runs in an economizer mode, with 100% outside air.

The two control strategies used in the analyses are a conventional control and MPC. Under a conventional control, the system operates during occupied hours trying to maintain a given setpoint temperature. Under MPC, temperature limits are allowed to float during occupied hours, and the cooling rates are optimized for the lowest energy consumption, allowing for night precooling. Both the planning horizon (the time interval over which the objective function is evaluated) and the execution horizon (the time interval over which the control strategy is applied) are 24 hours since in these simulations we have a perfect knowledge of weather conditions and loads.

6.1.1 Infiltration

During unoccupied hours, latent loads are caused by infiltration. According to the U.S. National Institute of Standards and Technology data base (Emmerich and Persily, 2011), the average measured airtightness of 228 commercial building (normalized by the above-grade surface area of the building envelope) is 24.8 $m^3/h/m^2$ at 75 Pa. The recommended value by ASHRAE Standard 189.1 for the Design of High-Performance Green Buildings, and also by 2012 International Energy Conservation Code is 7.2 $m^3/h/m^2$ at 75 Pa. To convert those values to a more typical pressure difference under ambient conditions (4 Pa) the power low equation is used:

$$V = c\,(\Delta P)^n \tag{6.1}$$

where V (m^3/s) is an airflow through openings, c ($m^3/(sPa^n)$) is the flow coefficient, and n is the pressure exponent. The pressure exponent n ranges from 0.5 to 1, with a typical value of 0.65 (ASHRAE, 2009). The values can also be converted to ACH based on the surface area of the building envelope and building volume as:

$$ACH = V(m^3/s/m^2)\frac{Surface\ area}{Volume} \times 3600 \tag{6.2}$$

Based on the geometry for a medium-size office from DOE benchmark buildings (50 m x 33 m floor plan), the infiltration rates in ACH are given in Table 6.1. The value used for the analysis is 0.2 ACH, as the average between the measured and recommended value.

Table 6.1 – Average measured and recommended airtightness for commercial office buildings

	@ 75 Pa in $m^3/h/m^2$	@ 4 Pa in $m^3/h/m^2$	@ 4 Pa in ACH
Measured average	24.8	3.7	0.37
Recommended	7.2	1.1	0.11

6.2 Comparison of split-system and LLCS for sensible cooling only

The LLCS and split-system were simulated for a typical summer week under the Atlanta and Phoenix climate to replicate the experimental measurements by Gayeski et al. (2012). The LLCS temperature limits were 19–25°C during occupied hours, while the split-system was controlled to maintain constant 22°C during the occupied hours. The pipe spacing for TABS was 30 cm. The simulations for Atlanta climate assumed standard office internal loads of 36 W/m^2, and for Phoenix climate high-performance loads of 22 W/m^2. The ventilation and dehumidification systems were not included in this analysis since they were not a part of the experimental measurements by Gayeski. Furthermore, both LLCS and split-system would need an additional system for ventilation and possible dehumidification. It is expected that they would perform relatively similar for both the LLCS and split-system and would not have major impact on the findings presented here. A heat pump with a maximum capacity of 3000 W was operated at the constant evaporator airflow and optimized condenser airflows.

Temperature profiles, thermal loads, and electricity consumption are shown for the split-system (Figure 6.2) and LLCS (Figure 6.3) for Atlanta, and for the split-system (Figure 6.4) and LLCS (Figure 6.5) for Phoenix. It can be seen from the results that MPC shifts the LLCS cooling rates toward night time, also resulting in the reduced peak loads during occupied hours, relative to the split-system under the conventional control. The same trends are found in the experimental measurements by Gayeski et al. (2012). However, the predicted electricity savings of 8.9% and 9.7% for Atlanta and Phoenix respectively are different from 25% and 19% achieved in measurements. Although it is interesting that simulations show lower savings than the measurements, this is caused by inevitable differences in modeling, especially in modeling the heat pump performance. The heat pumps used in the simulation were carefully optimized; hence, although trying match the heat pump operation used in the experiment, the simulated heat pump operated more efficiently than under experimental conditions. The COP is a strong function of the evaporating and condensing temperatures. Comparing the average evaporating and condensing temperatures for Atlanta, the measured evaporating temperatures for the split-system were lower than in the simulation,[1] resulting in a lower average COP. Predicted savings are highly sensitive to changes in the COP. For example, an average COP of 6.3 results in 8.9% electricity savings for Atlanta, while an average

---

[1] The measured average evaporating temperatures were approximately 9°C for the LLCS and 12°C for the split-system, and the average condensing temperatures were 27°C for the LLCS and 32°C for the split-system. The simulation results predicted the average evaporating temperatures of approximately 12°C for the LLCS and 17°C for the split-system, and the average condensing temperatures of 26°C for the TABS and 30°C for the split system.

COP of 5.3 would result in 24% difference. Furthermore, savings predictions are also highly sensitive to temperature setpoints, as can be seen in Table 6.2. Although simulations tried to mimic the experimental measurements, the small differences in temperature profiles between simulation and measurements can be an additional cause of differences in savings. The electricity consumption savings in the tables are defined as:

$$Savings = \frac{(E_{split\ system} - E_{LLCS})}{E_{split\ system}} \times 100 \tag{6.3}$$

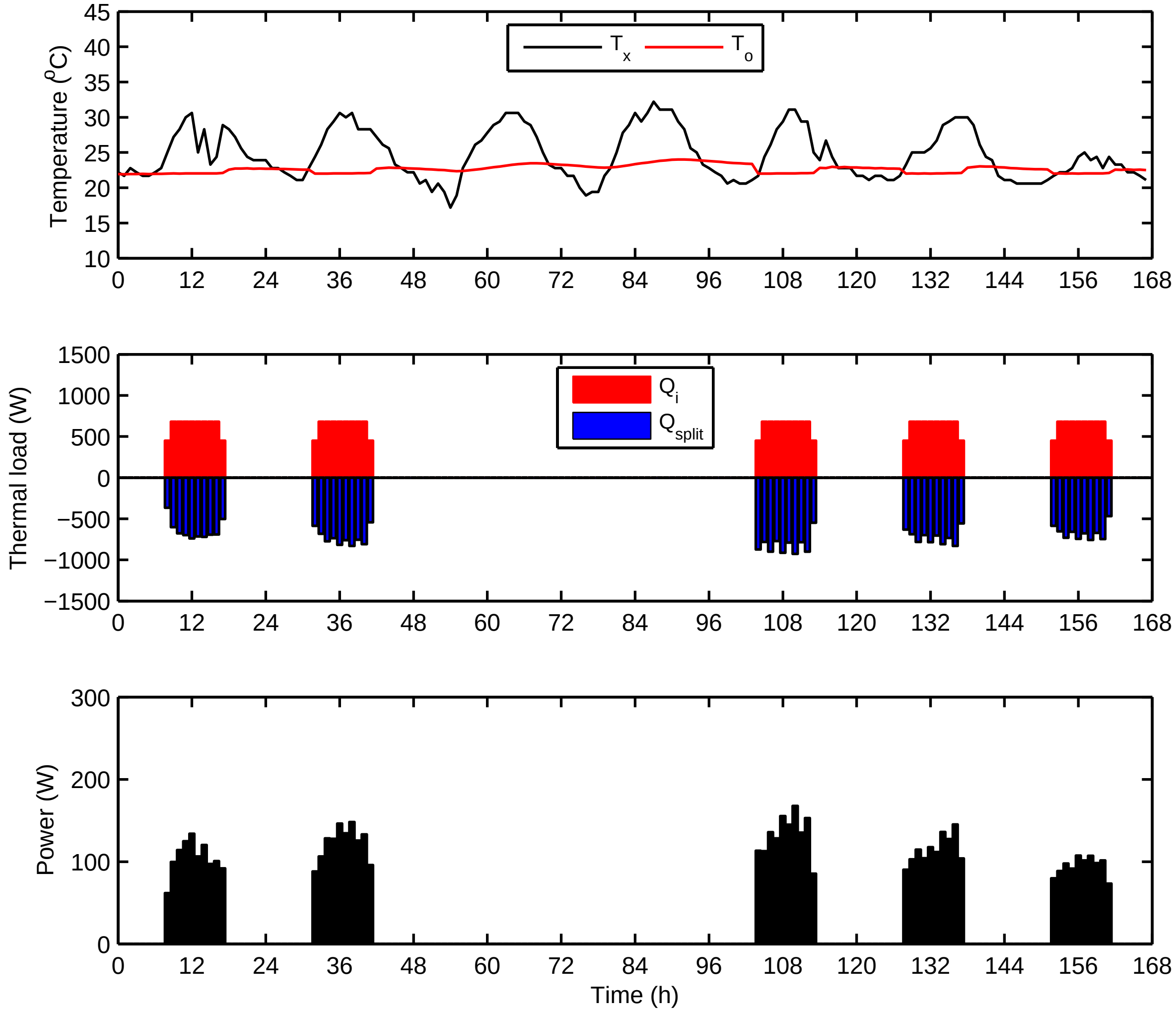

Figure 6.2 – Results for split-system for Atlanta climate and standard loads. Top graph shows outdoor air temperature T_x (black) and zone operative temperature T_o (red); middle graph shows internal load heat rate Q_i (red) and split-system cooling rate Q_{split} (blue); bottom graph shows electricity consumption.

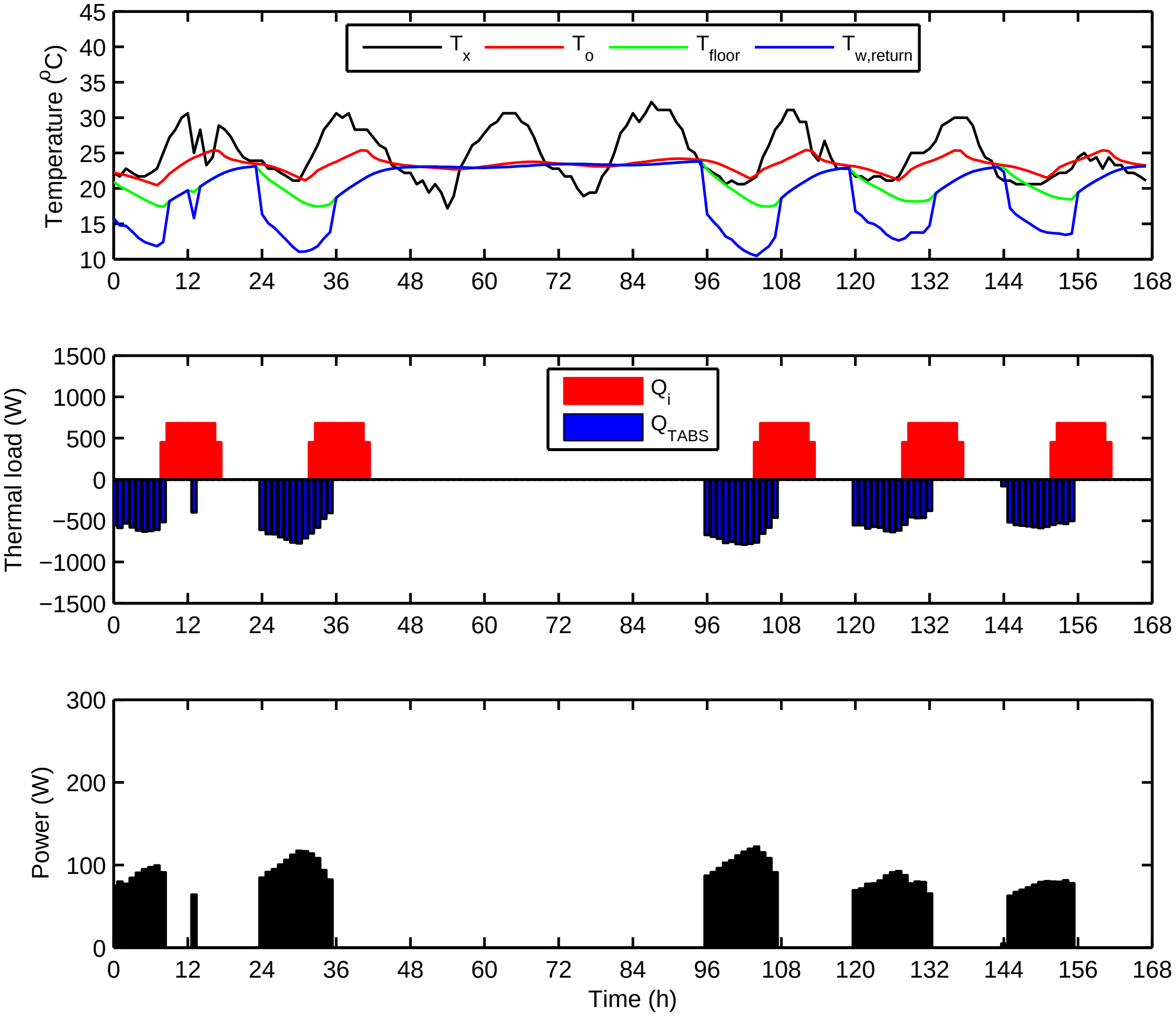

Figure 6.3 – Results for LLCS for Atlanta climate and standard loads. Top graph shows outdoor air temperature T_x (black), zone operative temperature T_o (red), floor temperature T_{floor} (green), and return water temperature $T_{w,return}$ (blue); middle graph shows internal load heat rate Q_i (red) and TABS cooling rate Q_{TABS} (blue); bottom graph shows electricity consumption.

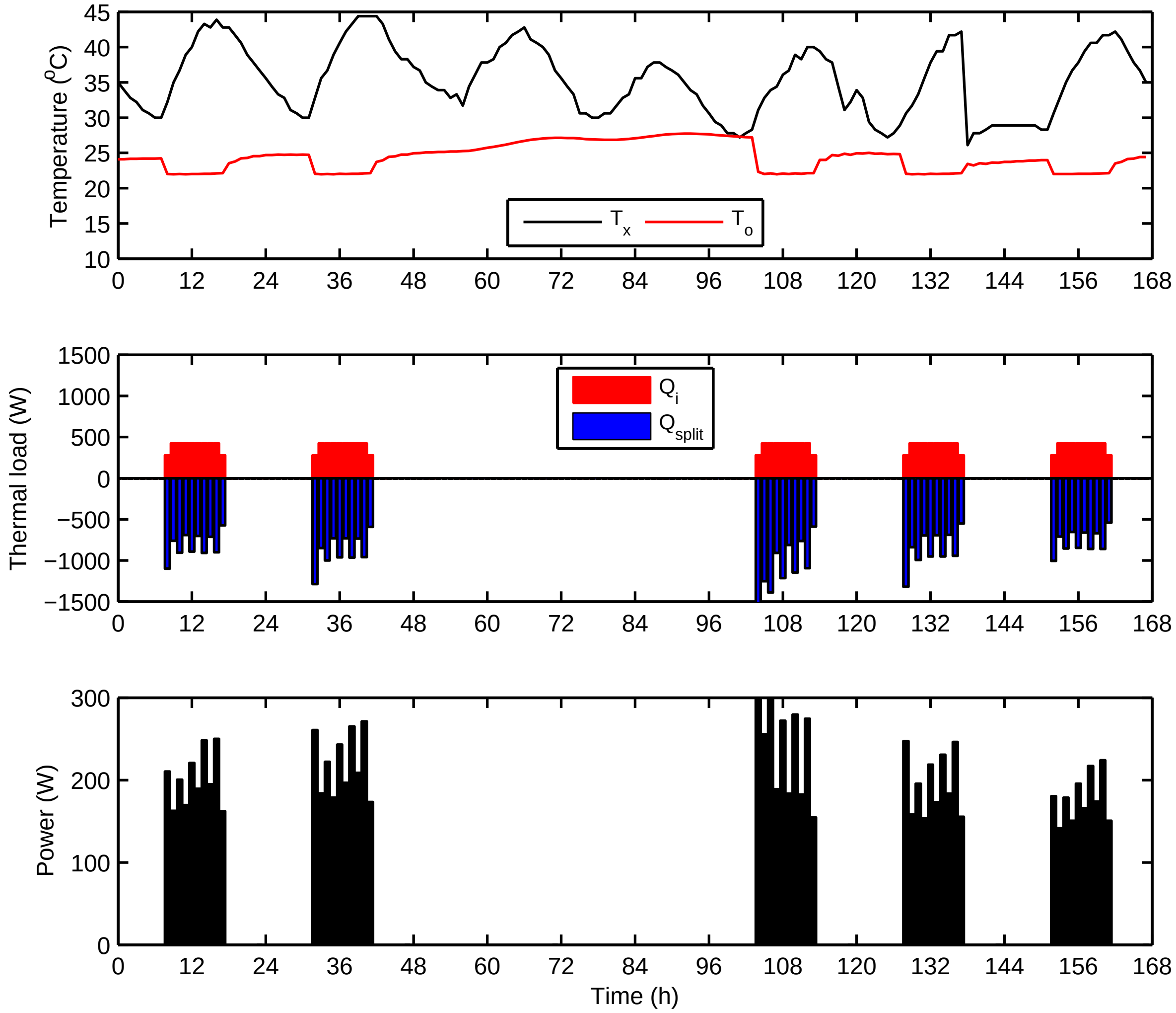

Figure 6.4 – Results for split-system for Phoenix climate and high-performance loads. Top graph shows outdoor air temperature T_x (black) and zone operative temperature T_o (red); middle graph shows internal load heat rate Q_i (red) and split-system cooling rate Q_{split} (blue); bottom graph shows electricity consumption.

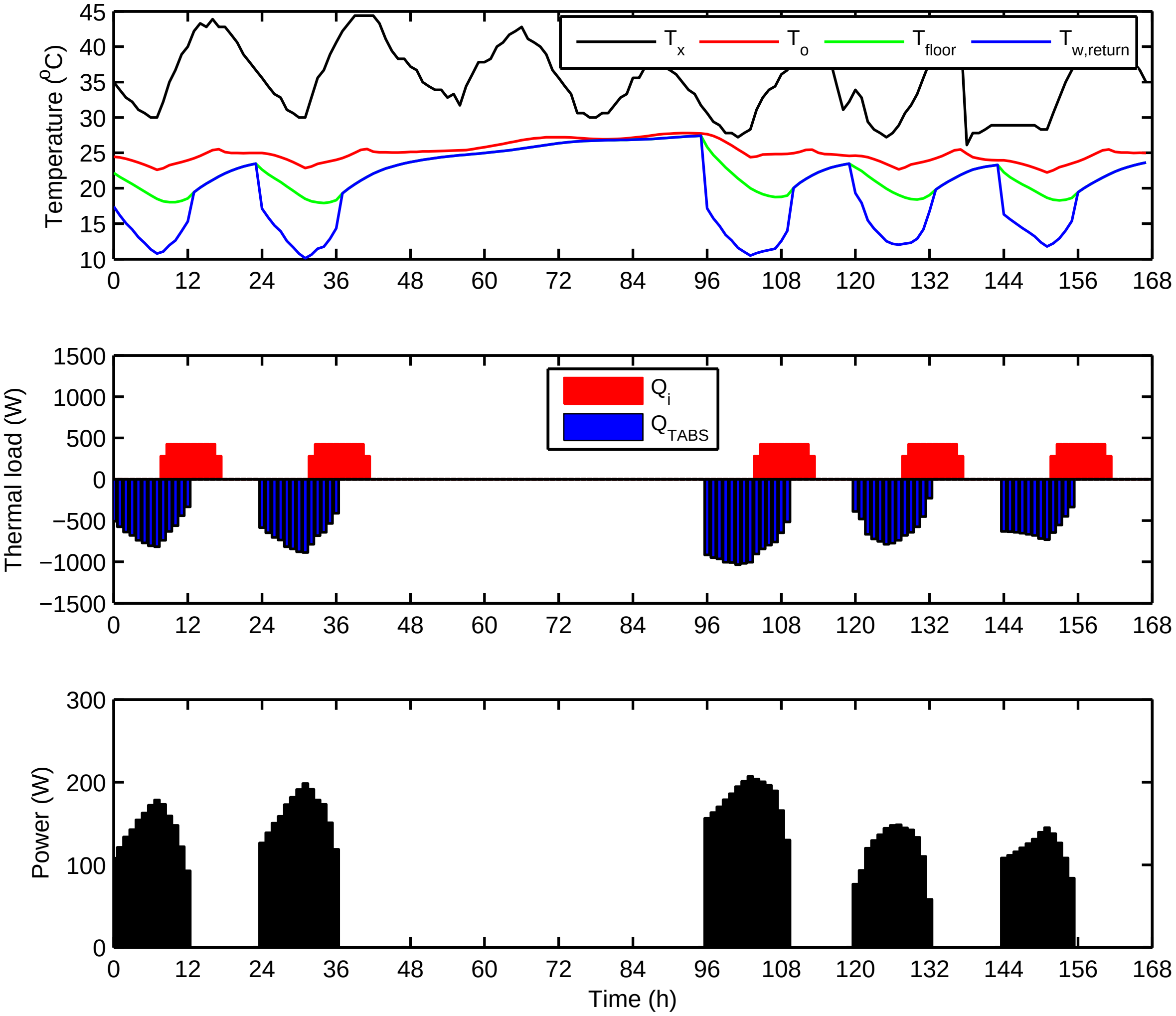

Figure 6.5 – Results for LLCS for Phoenix climate and high-performance loads. Top graph shows outdoor air temperature T_x (black), zone operative temperature T_o (red), floor temperature T_{floor} (green), and return water temperature $T_{w,return}$ (blue); middle graph shows internal load heat rate Q_i (red) and TABS cooling rate Q_{TABS} (blue); bottom graph shows electricity consumption.

6.2.1 Effect of pipe spacing

The pipe spacing of 30 cm used in the experimental measurements in somewhat atypical for cooling with TABS; hence, a new TABS system with the reduced pipe spacing of 15 cm is simulated here. This reduction improves the total effectiveness of TABS heat transfer, resulting in higher water temperatures (Figure 6.6) and significantly larger electricity savings for both climates (Table 6.3)

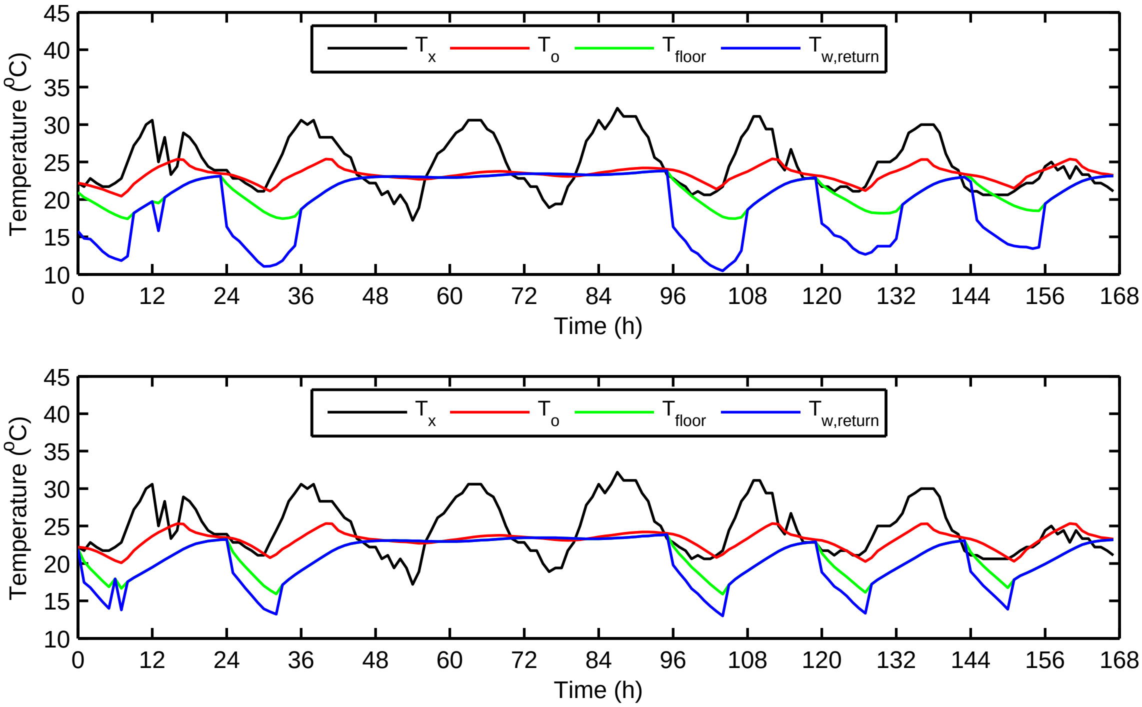

Figure 6.6 – Outdoor air temperature T_x (black), zone operative temperature T_o (red), floor temperature T_{floor} (green), and return water temperature $T_{w,return}$ (blue) for LLCS for Atlanta climate. Top graph shows temperatures for TABS pipe spacing of 30 cm; bottom graph shows temperatures for reduced TABS pipe spacing of 15 cm.

6.2.2 Effect of heat pump optimization

The air-to-air heat pump used in the experiment operated with optimized condenser airflows and constant evaporator airflow. To analyze the effect of the heat pump optimization, the air-to-air heat pump with optimized evaporator and condenser airflows was implemented for the split-system. This resulted in better performance for the split-system, and reduced the power saving potential of the LLCS (Table 6.4). The improvements in performance, however, were not as pronounced as was reported in Chapter 2 (Figure 2.12b) when comparing the setup with optimized and non-optimized airflows because condenser airflows were already optimized for the analyses presented at the beginning of section 6.2 and subsection 6.2.1.

6.2.3 Effect of heat pump sizing

Cooling and heating equipment are conventionally sized by calculating cooling/heating energy needs for a design day, and choosing the equipment capacity accordingly. Although it will rarely operate at its maximum capacity, the equipment will operate at high part-load ratios most of the time. The LLCS, on the other hand, will operate at lower part-load ratios as a result of cooling loads being spread during night and morning hours, and the daily peak loads being reduced. Since the heat pump COP increases for lower part-load ratios, this will favor the LLCS over the system with the conventional control. However, the heat pump of 3 kW used for the experimental measurements is greatly over-sized for the magnitude of the imposed sensible gains. As can be seen in Figures 6.2–6.5, the peak cooling loads rarely exceed 1 kW, even for the split-system operated under the conventional control for hot summer days in Phoenix. This causes both system to run at atypically low part-load ratios, especially pronounced for the conventional split-system. More appropriate sizing of the heat pump is done by reducing its capacity from 3 kW to 1.5 kW. This significantly increases savings potential of the LLCS, as shown in Table 6.5. Compared to the case with the over-sized heat pump, the electricity savings increase from 21% to 33.4% for Atlanta, and 23.6 % to 36% for Phoenix.

6.2.4 Effect of internal loads

Analyzing the cost savings potential of the VAV system under MPC, Henze et al. (2010) noted that no real savings were achieved for a building with high internal loads. To test these findings for the LLCS and electricity consumption savings rather than cost savings, different magnitudes of internal loads are imposed, ranging from 20 W/m^2 to 50 W/m^2. The internal loads of 20 W/m^2 are representative of new buildings implementing a high-performance envelope and equipment. Although not included in this work, solar gains would be an additional heat gain to the zone. However, office buildings, which are the best first candidates for LLCS implementation according to the PNNL study, are internally dominated buildings due to a small ratio of external surface to building volume. Hence, it is not anticipated that including solar gains would crucially change findings of this analysis, especially for core building zones. The results shown in Table 6.6 confirm findings by Henze et al. (2010) that savings are highly sensitive to internal loads. Reducing internal loads from 50 to 20 W/m^2 results in the saving potential increase from 25.4% to 53.3% for Atlanta and 16.7% to 37.3% for Phoenix.

6.2.5 Effect of temperature limits and precooling with split-system

To investigate the impact of MPC, the split-system was allowed to float between the same temperature limits during the occupied hours as the LLCS. Cooling rates for both systems are optimized over the 24-hour planning horizon. As shown in Figure 6.7, the load shift for the split-system is not as pronounced as for the LLCS since the split-system can not engage the building mass storage potential as effectively as the LLCS. However, the split-system under MPC was able to significantly reduce the electricity consumption relative to the system under the conventional control, performing even better than the LLCS. Compared with the LLCS with the same temperature limits (19-25°C), the split-system consumed 18.5%

less electricity in Atlanta and 10.6% less in Phoenix.

The load shift for the split-system also resulted in an undesirable increase of the total cooling energy. Relative to the split-system with 23°C setpoint temperatures, the total cooling energy for the system with MPC and 19-23°C temperature limits increased by 2.2% for Atlanta and 5.4% for Phoenix. However, even with this load increase, the cooling energy consumption is lower than for the LLCS. For same 19–23°C temperature limits, the LLCS consumes 28.7% more cooling energy (thermal) for Atlanta and 21.7% for Phoenix.

Although these results imply that the split-system controlled by MPC and with wider temperature limits could be equally, or even more promising as the LLCS, there are additional practical considerations to take into account. For example, TABS can provide more uniformed cooling since the whole surface acts as a heat exchanger area. Furthermore, the LLCS does not have fans that would compromise acoustic comfort, or cause discomfort for occupants due to cold air exiting the unit at high velocities. Finally, the LLCS can reduce the cost of electricity if utility rates favor night operation since the load shifting is much more effective than with the split-system.

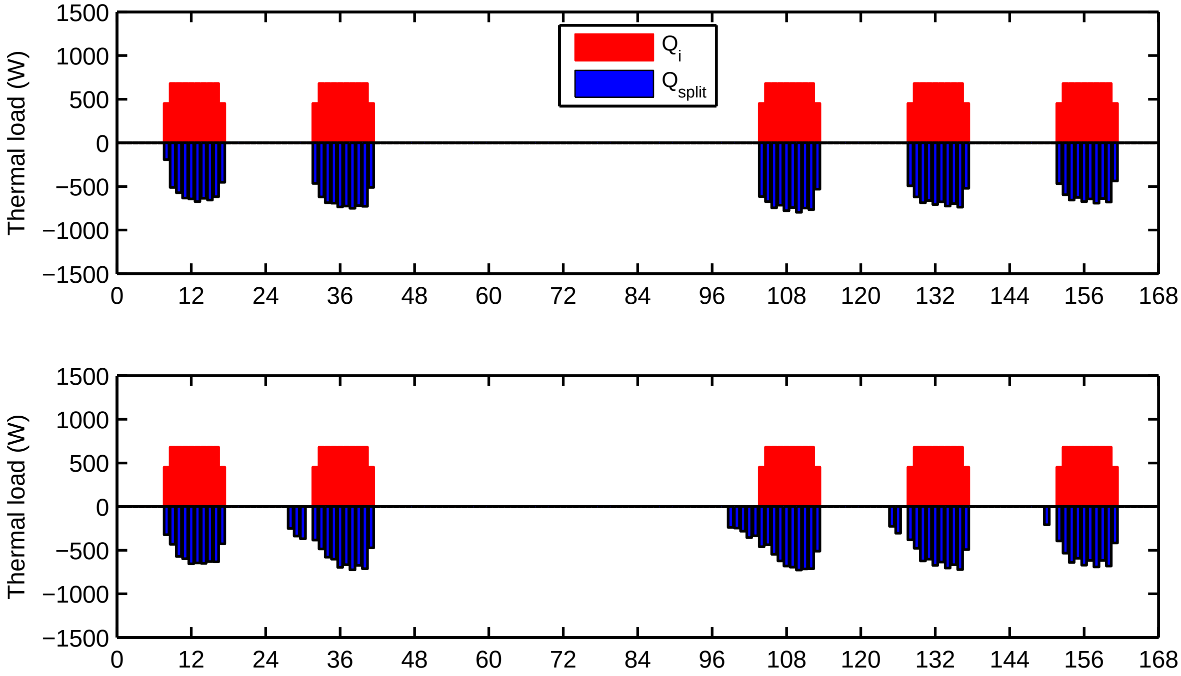

Figure 6.7 – Internal load heat rate Q_i (red) and split-system cooling rate Q_{split} (blue) for Atlanta climate. Top graph shows case without precooling and with daily temperature setpont 23°C; bottom graph shows case with precooling allowed, and with daily temperature limits 19–23 °C.

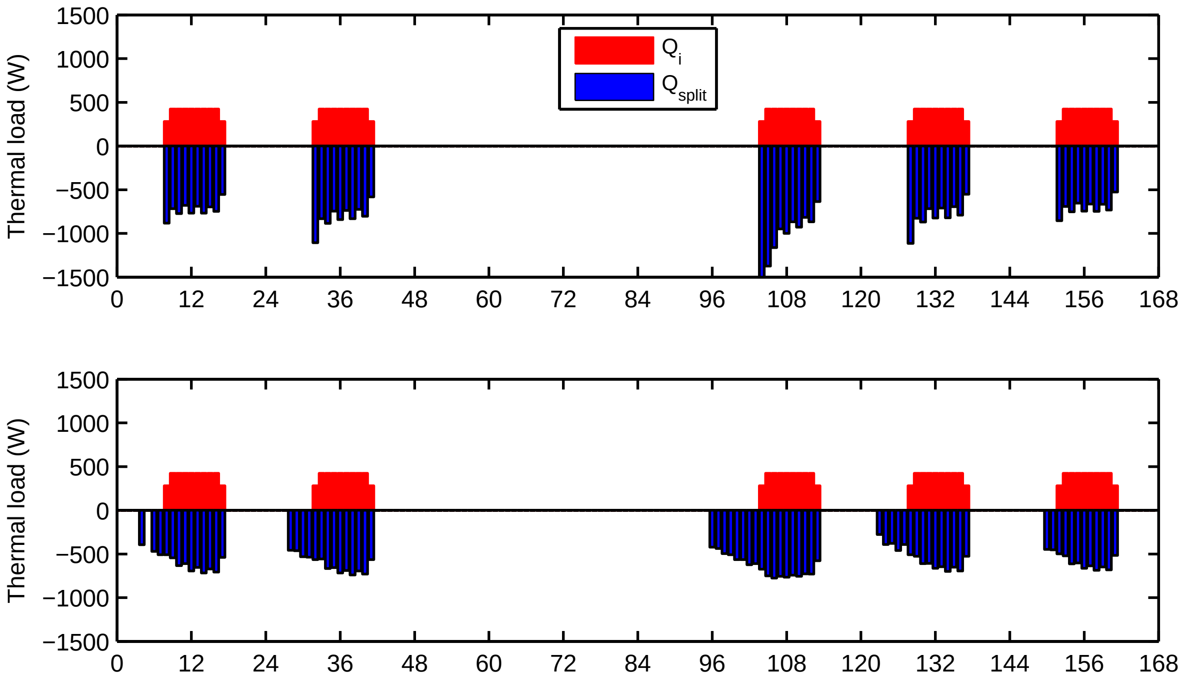

Figure 6.8 – Internal load heat rate Q_i (red) and split-system cooling rate Q_{split} (blue) for Phoenix climate. Top graph shows case without precooling and with daily temperature setpont 23°C; bottom graph shows case with precooling allowed, and with daily temperature limits 19–23 °C.

Table 6.2 – Electricity consumption savings of LLCS relative to split-system (SS) as a function of daily temperature limits. Setup with 30 cm pipe spacing for TABS, heat pump of capacity Q_{max} = 3 kW, and with optimized SS condenser airflows. Result are shown for a typical summer week with standard internal loads for Atlanta and high-performance loads for Phoenix.

Electricity savings for Atlanta (%)			
		LLCS	
		19–25 °C	**19–23 °C**
SS	**21 °C**	19.4	-12.9
	22 °C	8.9	-27.6
	23 °C	-3.5	-45.0

Electricity savings for Phoenix (%)			
		LLCS	
		19–25 °C	**19–23 °C**
SS	**21 °C**	20.1	-7.6
	22 °C	9.7	-21.6
	23 °C	-1.8	-37.2

Table 6.3 – Electricity consumption savings of LLCS relative to split-system (SS) as a function of daily temperature limits. Setup with 15 cm pipe spacing for TABS, heat pump of capacity Q_{max} = 3 kW, and with optimized SS condenser airflows.

Electricity savings for Atlanta (%)			
		LLCS	
		19–25 °C	**19–23 °C**
SS	**21 °C**	33.5	7.5
	22 °C	24.9	-4.5
	23 °C	14.7	-18.8

Electricity savings for Phoenix (%)			
		LLCS	
		19–25 °C	**19–23 °C**
SS	**21 °C**	33.8	12.4
	22 °C	25.3	1.0
	23 °C	15.7	-11.7

Table 6.4 – Electricity consumption savings of LLCS relative to split-system (SS) as a function of daily temperature limits. Setup with 15 cm pipe spacing for TABS, heat pump of capacity Q_{max} = 3 kW), and with optimized SS evaporator and condenser airflows.

Electricity savings for Atlanta (%)			
		LLCS	
		19–25 °C	**19–23 °C**
SS	**21 °C**	31.4	4.6
	22 °C	21.0	-10.0
	23 °C	7.9	-28.2

Electricity savings for Phoenix (%)			
		LLCS	
		19–25 °C	**19–23 °C**
SS	**21 °C**	31.8	9.7
	22 °C	23.6	-1.2
	23 °C	14.0	-13.9

Table 6.5 – Electricity consumption savings of LLCS relative to split-system (SS) as a function of daily temperature limits. Setup with 15 cm pipe spacing for TABS, heat pump of capacity Q_{max} = 1.5 kW, and with optimized SS evaporator and condenser airflows.

Electricity savings for Atlanta (%)			
		LLCS	
		19–25 °C	**19–23 °C**
SS	**21 °C**	44.3	19.4
	22 °C	33.4	3.7
	23 °C	20.1	-15.6

Electricity savings for Phoenix (%)			
		LLCS	
		19–25 °C	**19–23 °C**
SS	**21 °C**	44.4	23.2
	22 °C	36.0	11.6
	23 °C	25.4	-3.1

Table 6.6 – Electricity consumption savings of LLCS relative to split-system (SS) as a function of maximum internal loads. Setup with 15 cm pipe spacing for TABS, heat pump of capacity Q_{max} = 1.5 kW, and with optimized SS evaporator and condenser airflows. Result are shown for typical summer week with 19–25°C daily operative temperature for LLCS and 22°C for SS.

Electricity savings for Atlanta (%)			
20 W/m^2	**30 W/m^2**	**40 W/m^2**	**50 W/m^2**
53.3	39.4	30.8	25.4

Electricity savings for Phoenix (%)			
20 W/m^2	**30 W/m^2**	**40 W/m^2**	**50 W/m^2**
37.3	31.8	25.0	16.7

Table 6.7 – Electricity consumption savings of LLCS relative to split-system with precooling (SS) as a function of daily temperature limits. Setup with 15 cm pipe spacing for TABS, heat pump of capacity Q_{max} = 1.5 kW, and with optimized SS evaporator and condenser airflows.

Electricity savings for Atlanta (%)			
		LLCS	
		19–25 °C	**19–23 °C**
SS	**19–25 °C**	-18.5	
	19–23 °C		-18.3

Electricity savings for Phoenix (%)			
		LLCS	
		19–25 °C	**19–23 °C**
SS	**19–25 °C**	-10.6	
	19–23 °C		-15.6

6.3 Comparison of VAV system and LLCS for sensible cooling and dehumidification

The previous section compares the performance of the LLCS relative to the split-system taking into account only sensible cooling. This section investigates the performance of the LLCS relative to a VAV system by analyzing sensible cooling and dehumidification. Compared to the LLCS, the VAV system has larger transport power for fans, and a reduced potential to shift cooling toward colder night hours. Furthermore, the VAV system heat pump operates at lower evaporating temperatures than the LLCS heat pump since the air needs to be cooled to a temperature low enough for dehumidification. Even without dehumidification, delivering the VAV air at higher temperatures would result in increased air flows and a related transport power increase. The LLCS on the other hand, needs to deliver more cooling energy than the VAV system due to losses inherent to thermal storage.

The VAV system supplies saturated air at 12.5°C and is controlled based on the zone's temperature sensor. The LLCS consists of TABS for sensible cooling, and a parallel DOAS for ventilation and dehumidification. The DOAS also supplies saturated air at 12.5°C delivering a certain amount of sensible cooling in addition to ventilation and dehumidification. The VAV system airflow is controlled based on the sensible loads, and the DOAS airflow based on ventilation requirements and latent loads. Therefore, it is expected that the LLCS will provide better humidity control, especially in humid climates such as Miami. The VAV heat pump is sized for each climate based on the cooling coil peak loads. The LLCS heat pump is of the same capacity, but will on average operate at lower part-load ratios than the VAV heat pump increasing the average COP. The lower part-load ratios are the result of shifting cooling loads toward the night time, and providing a certain amount of sensible, and a total amount of latent cooling through the parallel system, DOAS. The DOAS heat pump is of a smaller capacity, and is equal for all climates. Due to the use of the enthalpy wheel, and relatively constant ventilation air flow rates, DOAS cooling coil loads do not show large variations across climates.

The first analysis compares the LLCS with different dehumidification configurations against a conventional VAV system. The conventional VAV system (marked in figures as 1) is operated during the occupied hours to maintain the zone operative temperature at 22.5°C. The LLCS employs MPC to optimize cooling rates over the 24-hour planning horizon for the lowest electricity consumption. It allows to precool the building during the night, maintaining the zone's operative temperature between 13–30°C during non-occupied hours and 20–25°C during occupied hours. The temperature limits in the comparison between the LLCS and split-system were 19–25°C replicating conditions Gayeski had during experimental measurements. In this analysis, the temperature limits were tightened, adjusting them more according to ASHRAE comfort standards. The analyzed DOAS configurations (described in details in Chapter 5) are: configuration A with the condenser cooled with the outside air (marked in figures as 2); configuration C with parallel condensers, one cooled with the supply, and the other with the return air (marked in figures as 3); configuration D with parallel condensers, one cooled with the supply, and the other with the outside air (marked in figures as 4); and configuration E with the run-around heat pipe and the condenser cooled with the outside air (marked in figures as 5). Configuration B has not been analyzed due to disadvantages described in Chapter 5.

The cooling energy (Figure 6.9), electricity consumption (Figure 6.10) and total electricity savings (Figure 6.11) are shown for a typical summer week across 16 typical U.S. climates, also used in the PNNL study on the LLCS. The total LLCS cooling energy (bars marked as 2–5) is lower relative to the VAV system (bar marked as 1) for mild climates (Fairbanks, Los Angeles, San Francisco and Seattle) since the LLCS has a wider temperature range than the VAV, allowing temperatures to float up to 25°C during the occupied hours. However, for the climates with higher cooling needs, the total cooling energy is higher than the VAV system due to losses inherent to thermal storage. Although it is using more cooling energy, the LLCS has 18–53% lower electricity consumption than the VAV system (Figure 6.11), depending on a climate and DOAS configuration. The electricity savings come from both the reduction in the electricity for cooling (black and grey bars in Figure 6.10) and electricity for the transport (pink bars).

The intent for the LLCS 3 and LLCS 4 was to improve the DOAS heat pump performance by placing one condenser in the supply stream and cooling it with a cold air exiting the evaporator at 12.5°C. However, the DOAS in the LLCS 2 delivers a certain amount of sensible cooling to the zone (negative green bars), while in the LLCS 3 and LLCS 4, the DOAS causes sensible heating (positive green bars) and the need for an additional sensible cooling thought TABS (Figure 6.9, blue bars). Therefore, although indeed reducing the electricity consumption for the DOAS heat pump (grey bars in Figure 6.10), the LLCS 3 and LLCS 4 increase the electricity for TABS cooling (black bars) and for the transport (pink bars). It is shown in the section 6.2. that the load shifting through the use of TABS generally has a positive impact on the energy consumption. In this case, however, the DOAS still uses electricity to cool/dehumidify the fresh air, and to transport it to the zone. As a result, the total electricity consumption increases across all climates due to an increase in the TABS cooling energy and transport power. For example, in the Phoenix climate DOAS heat pump electricity is reduced by 46 and 42% for the LLCS 3 and LLCS 4 respectively. However, TABS cooling energy increases approximately 48%, and the electricity for the TABS heat pump increases 80% due to higher part-load ratios and more cooling during warm hours (Figure 6.12). The total transport energy also increases by 15% due to more pump-on hours. It can also be seen from Figure 6.12 that the DOAS is turned off during first two nights since the outside humidity is lower than the zone's humidity, and there is no need for night dehumidification.

The LLCS 5 with the run-around heat pipe also reduces the amount of sensible cooling delivered by the DOAS, although not as much as the LLCS 3 and LLCS 4. The electricity for the DOAS heat pump is again reduced due to lower sensible loads on the cooling coil. However, the total electricity consumption is still somewhat higher than for the LLCS 2 due to additional cooling and transport energy used for cooling through TABS.

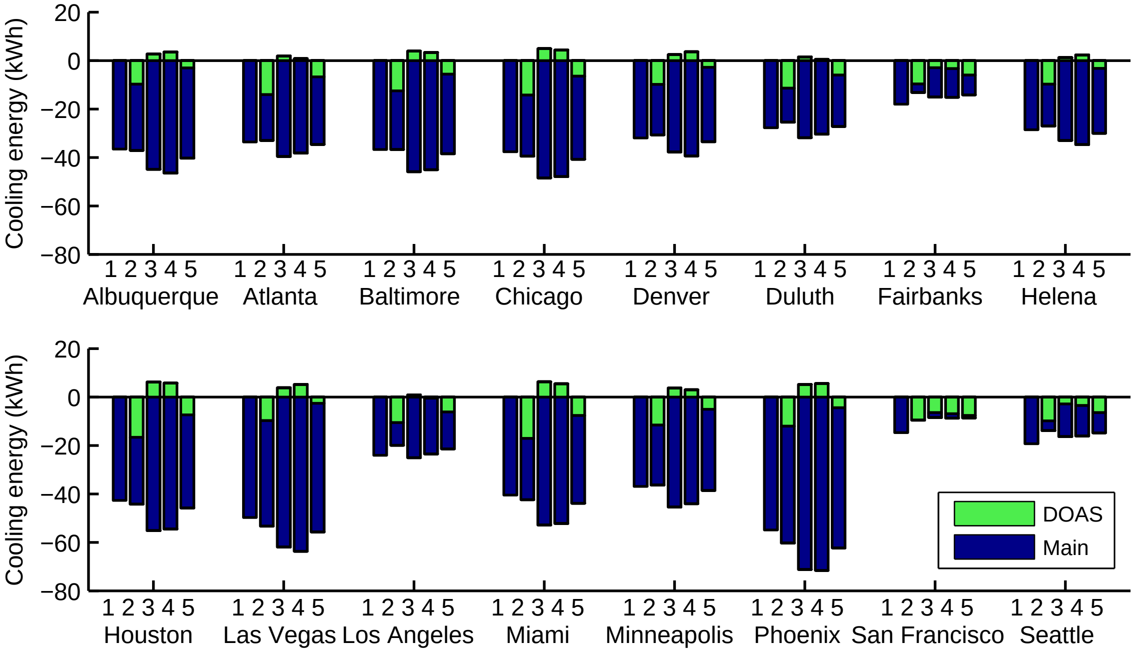

Figure 6.9 – Cooling energy delivered by VAV system (1) and LLCS with different DOAS configurations (2-5) for a typical summer week. TABS and VAV cooling is shown with blue bars, and DOAS cooling with green bars.

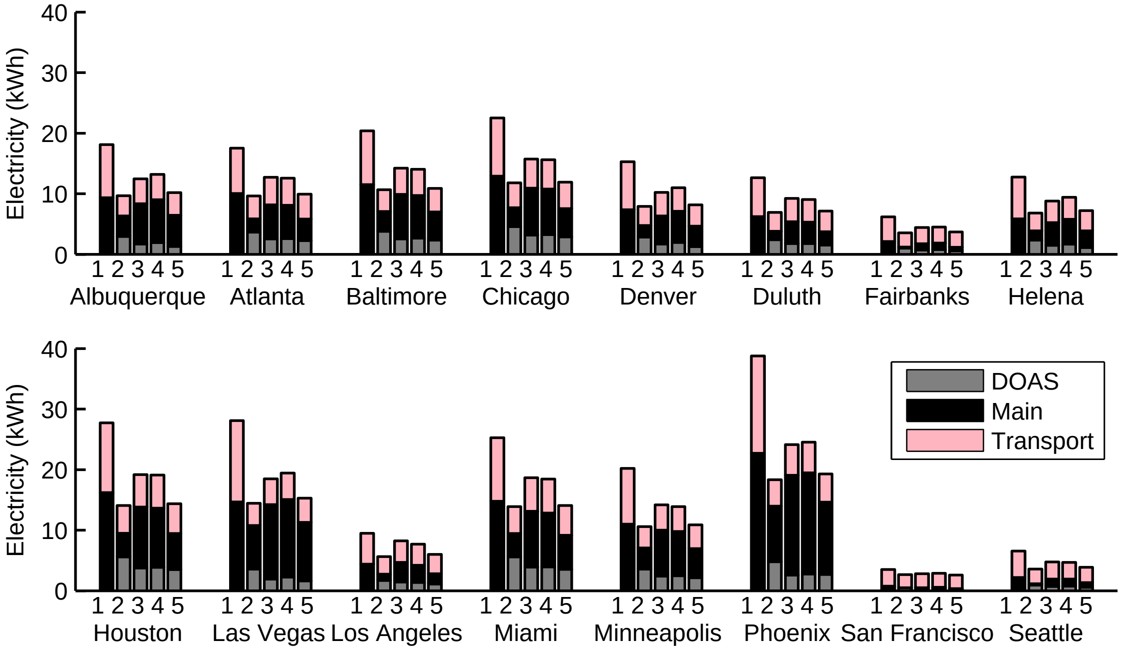

Figure 6.10 – Electricity consumption for VAV system (1) and LLCS with different DOAS configurations (2-5) for a typical summer week. Electricity for TABS and VAV system heat pump is shown with black bars, for DOAS heat pump with grey bars, and for transport energy with pink bars.

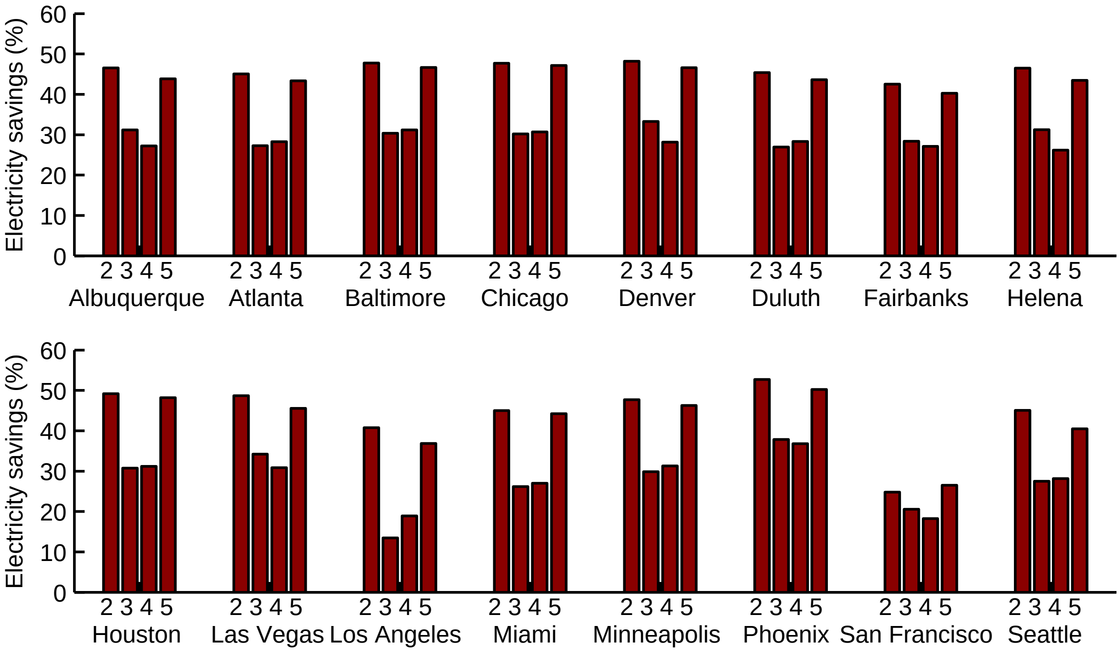

Figure 6.11 – Electricity savings of LLCS system with different DOAS configurations (2-4) relative to conventional VAV system for a typical summer week

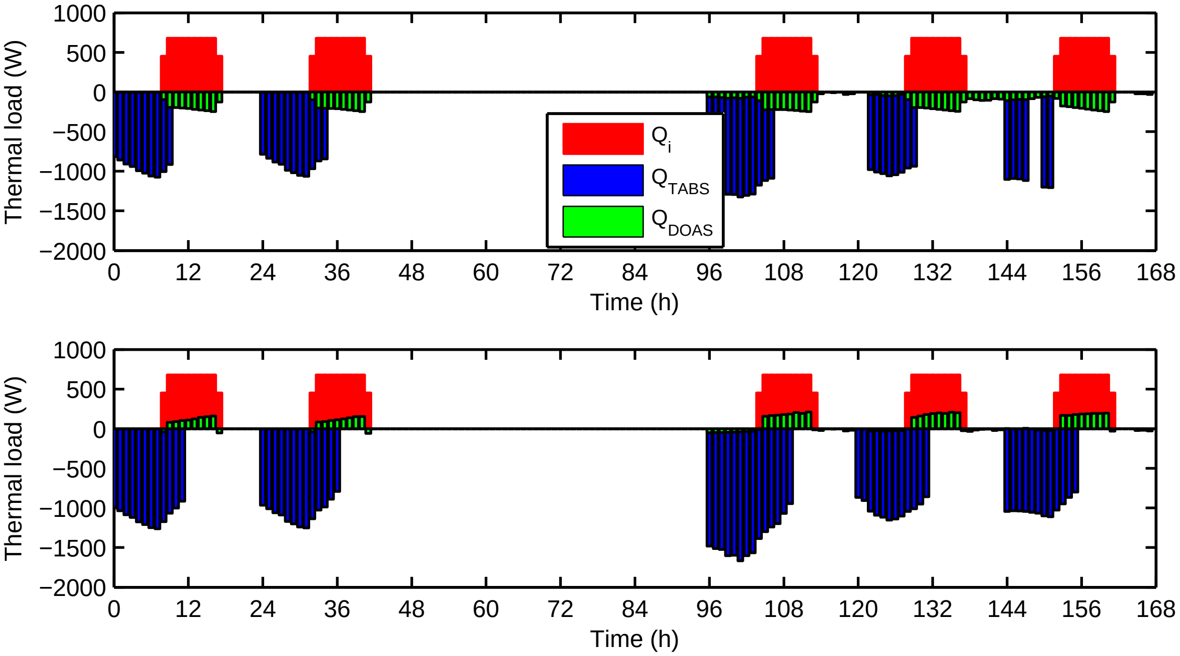

Figure 6.12 – Sensible internal gains (red), TABS cooling rates (blue), and DOAS cooling rates (green) for LLCS with two different DOAS configurations shown for a typical summer week in Phoenix. Top graph is for DOAS with condenser placed outside; bottom graph for condensers placed in supply and return stream.

6.3.1 Effect of temperature limits and precooling

The previous analysis compared the conventionally-controlled VAV system to the LLCS. Beside the technology, the main differences between the two were temperature limits and system controls. The VAV system was operated only during the occupied hours to maintain the zone's operative temperature at 22.5°C. The LLCS utilized MPC, allowing the temperature to float between 20 and 25°C. The following analysis investigates the impact of wider temperature limits and the use of MPC for the VAV system, allowing the operative temperature to float between the same 20–25°C. Furthermore, it also investigates the impact of precooling for both the VAV and LLCS.

The impact of precooling for the VAV system is shown in Figure 6.13 for a typical summer week in 16 U.S. climates. First, MPC is used to optimize the VAV cooling rates only during the occupied hours, allowing a temperature range of 20–25°C. The cooling rates are then optimized for same temperature range, but allowing the system to operate during the non-occupied hours. The comparison between the two cases suggests that VAV system precooling does not have a significant impact on the total electricity consumption, with in increase of savings being less than 3%. As can be seen from the Phoenix example (Figure 6.17), the VAV system with precooling does shift a certain amount of cooling toward early morning hours, but the impact is marginal, resulting in less than 3% difference in the electricity consumption. The temperature profile (Figure 6.19, top) for cooling with VAV also shows that the system was maintaining a relatively constant temperature of 25°C through the day.

The same analysis is shown in Figure 6.14 for the LLCS. First, MPC was only allowed to optimize the TABS cooling rates during the occupied hours. The system started operating one hour before the occupied hours to account for the inertia of the LLCS compared with the VAV system. As can be seen from the results, the impact of precooling for the LLCS is notably more pronounced, especially for hot climates such as Las Vegas (15% difference) and Phoenix (11% difference). The importance of load shifting is demonstrated in the Phoenix example (Figure 6.18). When the cooling rates are optimized only during the occupied hours (top graph), the cooling shifts toward early morning hours to take advantage of lower temperatures. The cooling shifts even more when the system was allowed to precool during the unoccupied hours (bottom graph). Figure 6.19 (bottom graph) shows the effect that LLCS precooling has on the temperature profile. Different than the VAV system, the operative temperature steadily increased from 21 to 25°C during the occupied hours, resulting in a lower average daily temperature compared to the VAV system.

Comparing the electricity consumption of the LLCS with precooling relative to the VAV system with precooling (Figure 6.15), the savings range from -11% for Los Angeles and Seattle to 29% for Phoenix. The total cooling energy for the LLCS is higher than the VAV system due to losses associated to passive thermal storage. However, for most climates higher heat pump efficiency and lower transport power for the LLCS result in lower electricity consumption compared with the VAV system. The only climates where the VAV system seems to perform better than the LLCS are Fairbanks, Los Angeles, Seattle and San Francisco, mild climes with the lowest cooling energy needs. Between a hot, humid climate such Miami and a hot, dry climate such as Phoenix, a humid climate shows notably less savings since more energy is required for dehumidification. In humid climates, the DOAS needs to deliver more air during night to remove latent loads caused by infiltration, resulting in higher transport and cooling energy. Nevertheless, comparing the LLCS and VAV system performance for Miami, the zone's humidity oscillations are lower for the LLCS due to a decoupling between the humidity and temperature control (Figure 6.20).

Finally, the electricity consumption of the VAV system and LLCS (both with precooling) is compared to the conventional VAV system that operates only during the occupied hours maintaining the constant temperature of 22.5°C (Figure 6.16). As expected, allowing larger temperature range results in significant savings, 30–50% for the VAV system and 25–53% for the LLCS. The operative temperatures for the LLCS steadily increase between morning and afternoon hours, resulting in an average daily temperature similar to the conventional system of 22.5°C. The operative temperature for the VAV system, however, stays in the upper limit of 25°C thought the day. The electricity savings for the VAV system relative to the conventional VAV system are primarily caused by the increase in the operative temperature, and only marginally by precooling. LLCS savings are a result of a better heat pump performance achieved through higher evaporating temperatures, lower condensing temperatures and lower part-loads capacity ratios. Also, a notable portion of savings comes from reduced transport energy relative to the VAV system.

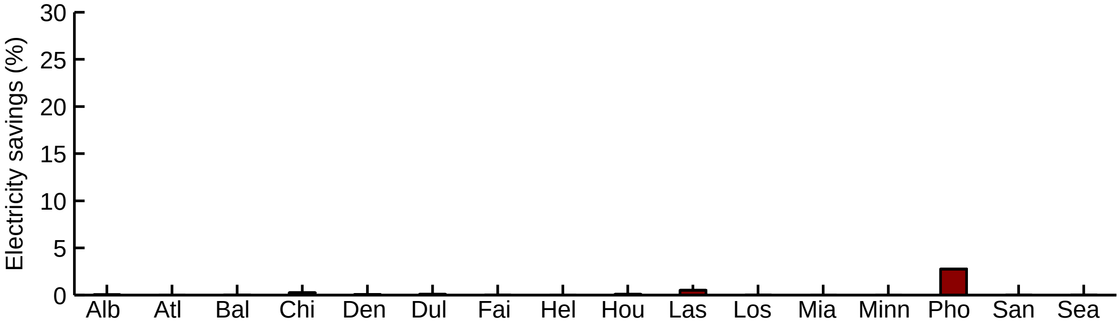

Figure 6.13 – Electricity savings for VAV system with precooling relative to VAV system without precooling for a typical summer week. Both cases utilize model predictive control and temperature limits 20–25°C

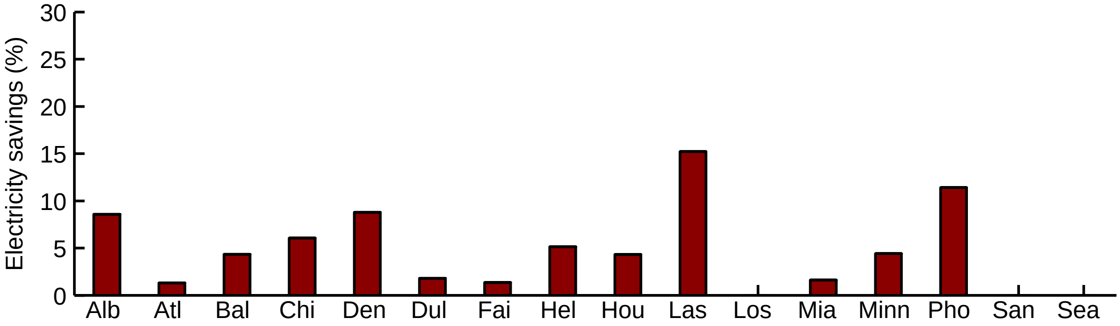

Figure 6.14 – Electricity savings for LLCS with precooling relative to LLCS system without precooling for a typical summer week. Both cases utilize model predictive control and temperature limits 20–25°C

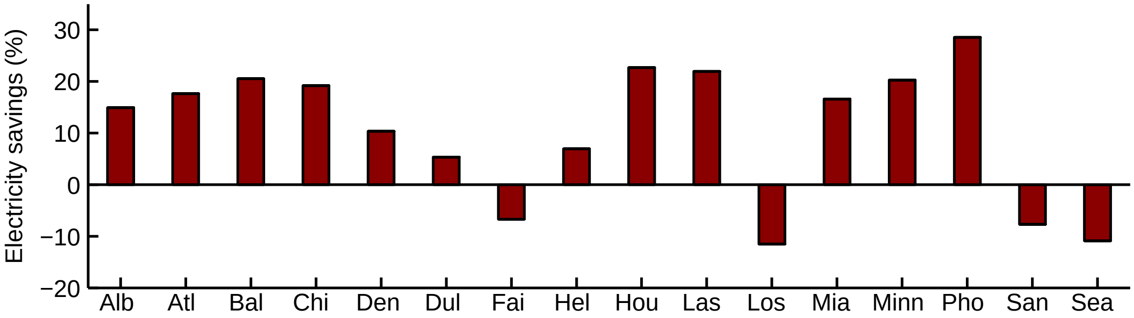

Figure 6.15 – Electricity savings for LLCS with precooling relative to VAV system with precooling for a typical summer week

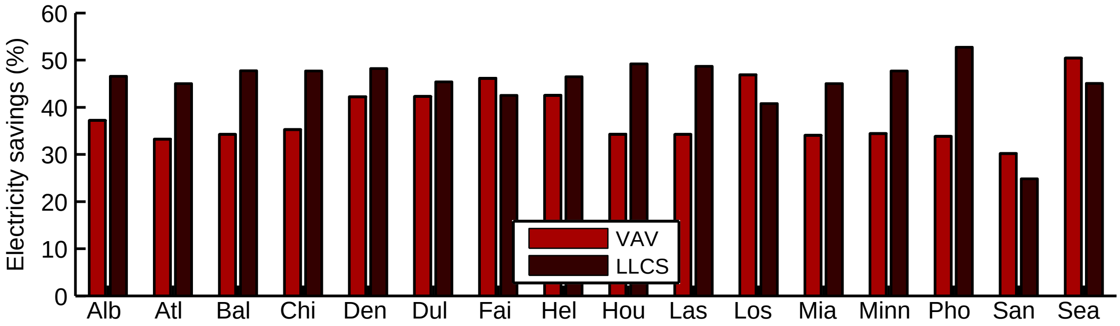

Figure 6.16 – Electricity savings for VAV system with precooling (bright red) and LLCS with precooling (dark red) relative to conventional VAV system (22.5°C setpoint temperature and no preccoling)

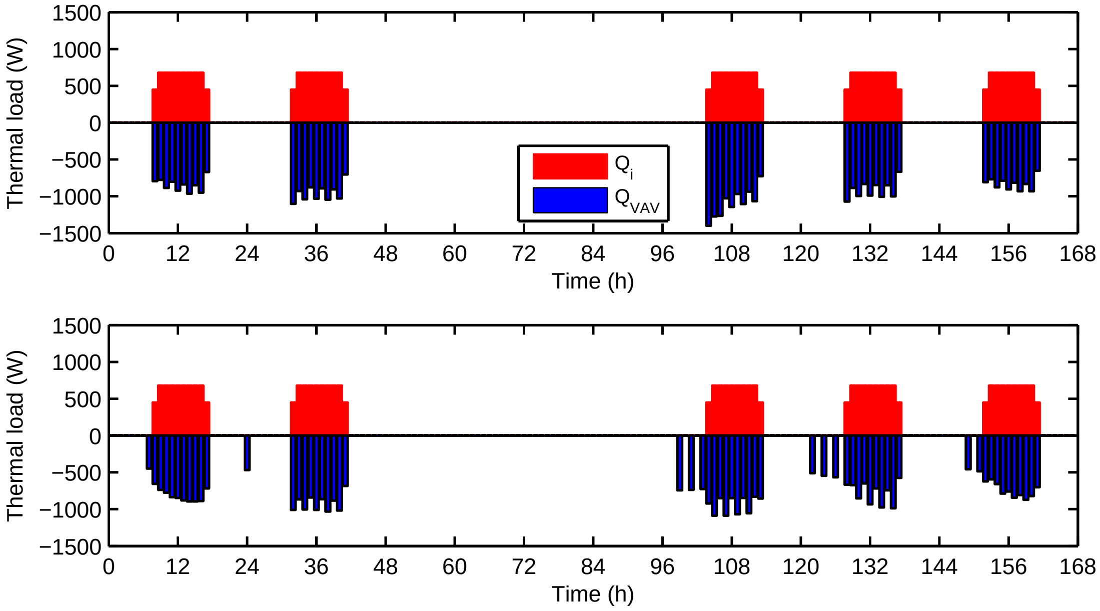

Figure 6.17 – Internal gains (red) and VAV cooling rates (blue) for a typical summer week in Phoenix. Top graph shows the case where MPC was utilized during operating hours; bottom graph shows the case with precooling.

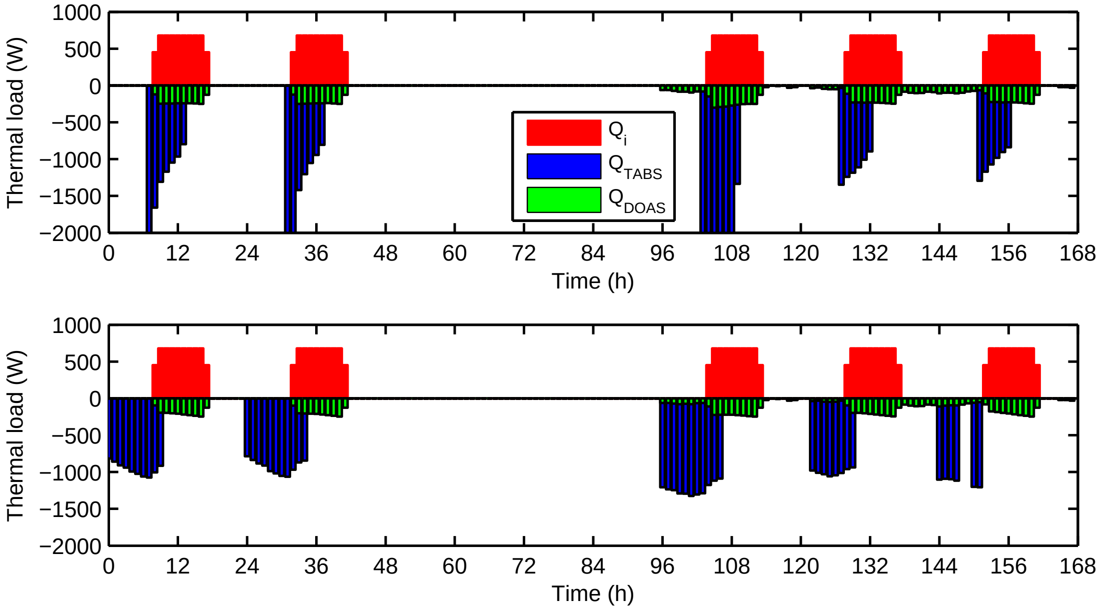

Figure 6.18 – Internal gains (red), TABS cooling rates (blue) and DOAS cooling rates (green) for a typical summer week in Phoenix. Top graph shows the case where MPC was utilized during operating hours; bottom graph shows the case with precooling.

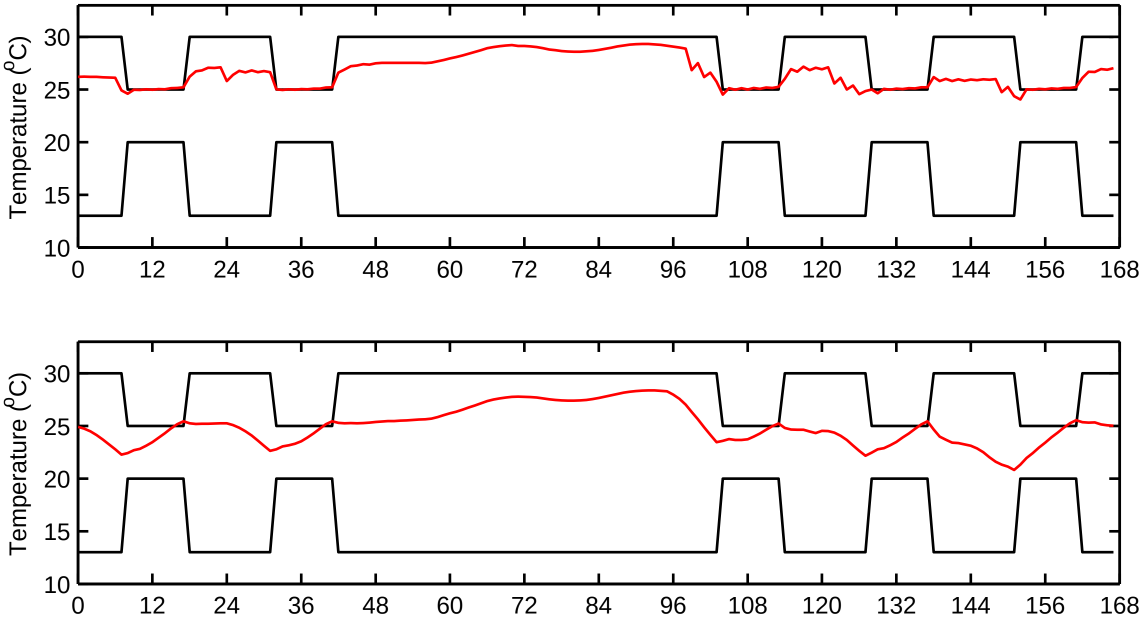

Figure 6.19 – Operative temperatures (red) and temperature limits (black) for a typical summer week in Phoenix. Top graph is for VAV system with precooling; bottom graph is for LLCS with precooling.

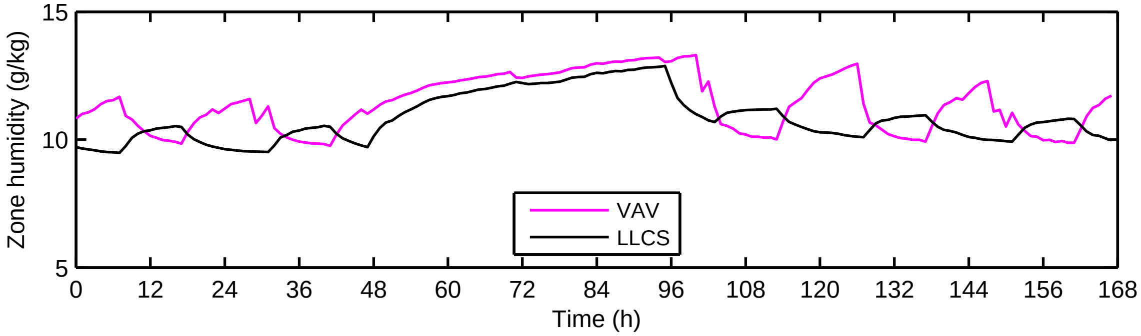

Figure 6.20 – Zone humidity for VAV system (pink) and LLCS (black) for a typical summer week in Miami

6.3.2 Seasonal savings

To estimate how the LLCS would perform relative to the VAV system over the whole spring and summer season, a 22-week period (from May 1 until September 30) is simulated for five climates with large cooling energy needs (Chicago, Houston, Las Vegas, Miami, and Phoenix). Results for the VAV system with and without precooling (Figure 6.21a), and for the LLCS with and without precooling (Figure 6.21b) confirm that the precooling has a significantly higher impact for the LLCS. The LLCS also performs better than the VAV system, with electricity savings 14–22% relative to the VAV system with precooling (Figure 6.21c), and 43–50% relative to the conventional VAV system (Figure 6.21d).

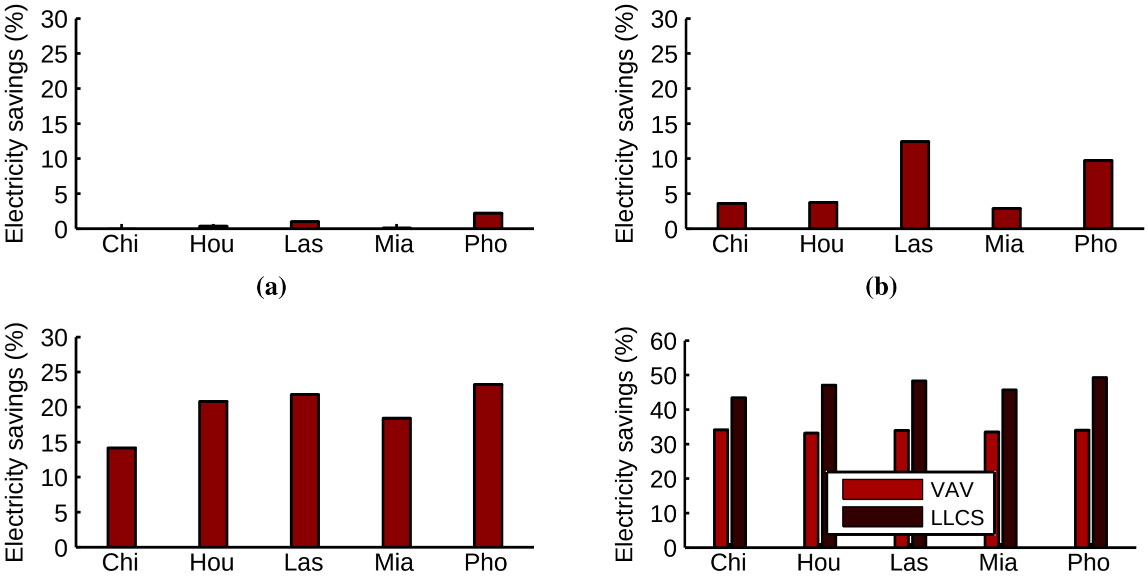

(a) **(b)**

(c) **(d)**

Figure 6.21 – Electricity savings for a period from May 1 until September 30. (a) VAV system with precooling relative to the case with no precooling, (b) LLCS system with precooling relative to the case with no precooling (c) LLCS system with precooling relative to VAV system with precooling (d) VAV system with precooling (bright red) and LLCS system with precooling (dark red) relative to conventional VAV system.

The findings of this analysis are compared to the PNNL study results obtained by Armstrong et al. (2009) and Katipamula et al. (2010). The results of the study are very valuable for an order-of-magnitude comparison, although the PNNL study used somewhat different assumptions. It assumed that an ideal water storage is cooled during night and then used to meet cooling needs during the operating hours. This study utilizes the building mass as the passive thermal storage, precooling it during night. When analyzing the case without precooling, the LLCS operates only during the occupied hours. The PNNL study results show the significant impact of the use of storage (precooling) on both the VAV system and LLCS. For a standard-performance medium office building, the annual electricity savings are 5–24% for the VAV system with storage relative to the system without storage (Figure 6.22, top graph), and 8–28% for the TABS system with storage relative to the system without storage (Figure 6.22, middle graph). Different than the PNNL study, the present study shows a very low effect of precooling on the VAV system electricity consumption. The impact is notable for the LLCS, but still less than the PNNL results.

The differences between the findings are expected since the PNNL study assumes ideal, active thermal storage whose performance does not depend on the building mass, nor storage losses.

Finally, both the PNNL and the current study findings are compared in terms of LLCS savings relative to the VAV system, both systems utilizing thermal storage (Figure 6.21c for the current study and Figure 6.22c for PNNL study). The results give similar order of magnitude for electricity savings, with savings of 17% (PNNL study) and 14% (current study) for Chicago, 8 and 21% for Houston, 35 and 22% for Las Vegas, 10 and 18% for Miami, and 31 and 23% for Phoenix. However, while the PNNL study results show significantly lower savings for hot, humid climates (Houston and Miami) compared to hot, dry climates (Phoenix and Las Vegas), such differences are not as pronounced in this study. A possible reason for this contrast might be an assumptions made for the DOAS. The PNNL analysis assumed that the heat from the DOAS condenser is rejected to the supply stream, hence, does not deliver any sensible cooling to the zone. This study assumes that the DOAS delivers air at a constant temperature of 12.5°C. Therefore, although humid climates require more air for dehumidification, which increases the transport energy, the air is also used to deliver certain amount of sensible cooling to the zone. The optimization between TABS sensible cooling and DOAS sensible cooling is an interesting topic that will be addressed in future research.

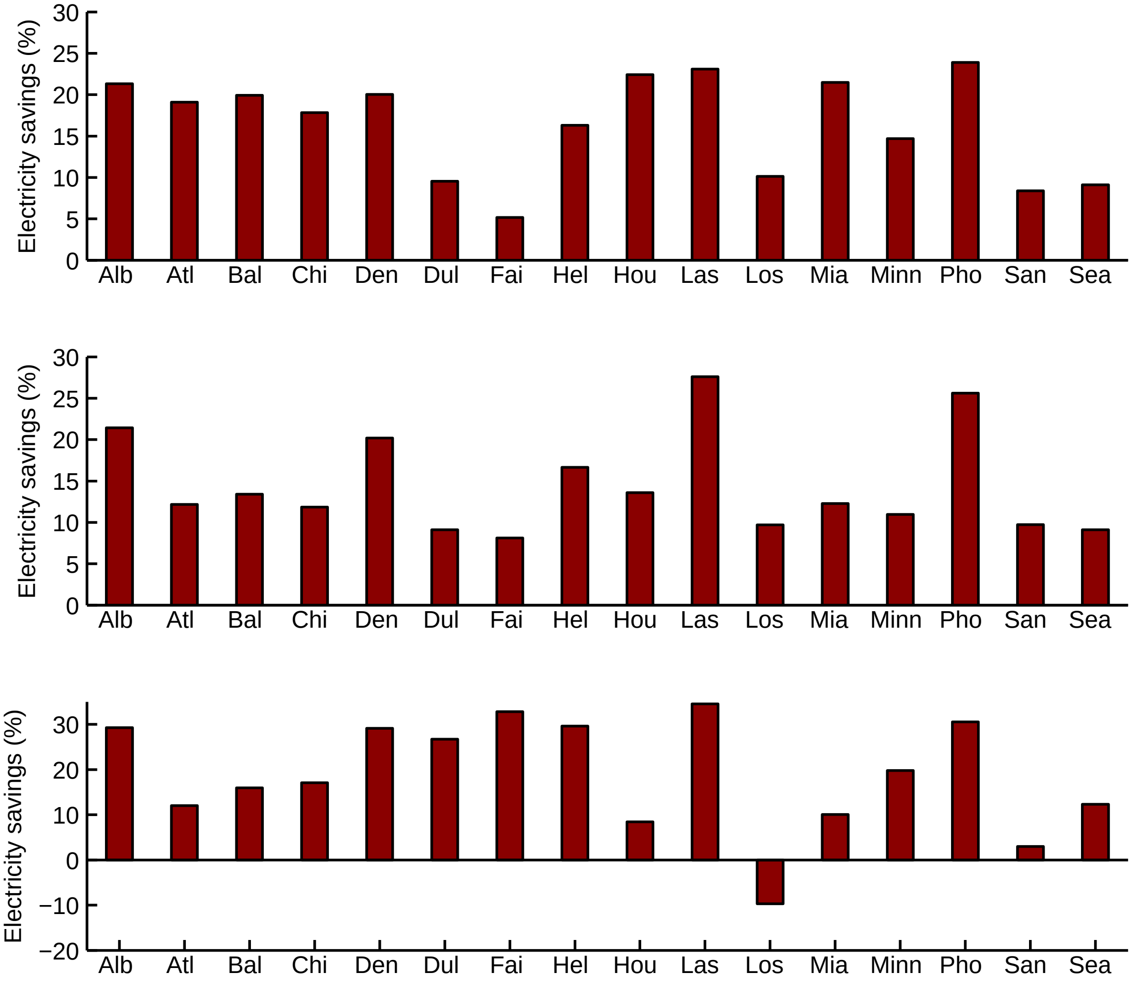

Figure 6.22 – Annual electricity savings from the PNNL study (Katipamula et al., 2010). Top graph shows savings for VAV system with active thermal storage relative to the case without storage; middle graph shows savings for TABS with storage relative to the case without storage; bottom graph shows savings for TABS relative to VAV system, both with storage.

6.3.3 Effect of internal loads

As seen in section 6.2.4, the LLCS electricity savings relative to the split-system are very dependent on the magnitude of the internal loads. While section 6.2.4 compares the systems assuming they provide sensible cooling only, the LLCS and VAV compared here are assumed to provide sensible cooling, dehumidification, and ventilation. The analysis is done for five climates, increasing the sensible internal loads from 20 to 60 W/m^2.

The first two rows in Tables 6.8 – 6.12 show the impact of precooling for the VAV and LLCS as a function of internal loads. Having negligible differences for the VAV system, the significance of precooling increases for the LLCS as the internal loads increase. For low internal loads, a large portion of sensible cooling is still provided through the DOAS. As the loads increase, the TABS cooling becomes predominant, with a greater opportunity for load shifting.

It is interesting to note that the LLCS electricity savings relative to the VAV system (third row of Tables 6.8 – 6.12) show steady growth as the internal load increases. In section 6.2.4 it was seen that the electricity savings for the LLCS relative to the split-system decrease as the internal loads increase. However, the transport energy for the VAV system analyzed here is considerably larger than for the split-system and LLCS. Hence, as the internal loads increase, the VAV system needs to deliver large amounts of air, resulting in the large transport energy. When comparing the LLCS relative to the VAV system, the savings in electricity for cooling (TABS plus DOAS) indeed decrease for larger internal loads (Table 6.13), but the total electricity consumption is still lower due to high fan transport powers of the VAV system. This advantage of the LLCS, however, starts the decay at the certain load (depending on a climate). As can be seen from the Las Vegas example (Table 6.10, third row), the LLCS savings increase up to 40 W/m^2 after which they start to decrease. The same trends are observed comparing the LLCS with the conventional VAV system (fifth row).

Table 6.8 – Electricity savings for a typical summer week in Chicago as a function of internal loads

	Electricity savings for Chicago (%)				
	20 W/m^2	**30 W/m^2**	**40 W/m^2**	**50 W/m^2**	**60 W/m^2**
VAV w versus VAV w/o precooling	0	0	0.3	0.4	0
LLC w versus LLC w/o precooling	1.9	5.5	7.9	9.4	12.4
LLC w versus VAV w precooling	12.8	16.7	19.9	22.6	22.8
VAV w precool. versus conventional VAV	34.7	34.6	30.0	26.1	27.7
LLC w precool. versus conventional VAV	43.0	45.5	44.1	42.8	44.2

Table 6.9 – Electricity savings for a typical summer week in Houston as a function of internal loads

	Electricity savings for Houston (%)				
	20 W/m^2	**30 W/m^2**	**40 W/m^2**	**50 W/m^2**	**60 W/m^2**
VAV w versus VAV w/o precooling	0	0	0.6	1.4	0.4
LLC w versus LLC w/o precooling	0	2.8	4.9	6.7	10.5
LLC w versus VAV w precooling	15.6	20.3	22.3	23.3	22.3
VAV w precool. versus conventional VAV	33.2	33.6	31.0	28.1	29.5
LLC w precool. versus conventional VAV	43.6	47.1	46.4	44.8	45.3

Table 6.10 – Electricity savings for a typical summer week in Las Vegas as a function of internal loads

	Electricity savings for Las Vegas (%)				
	20 W/m^2	**30 W/m^2**	**40 W/m^2**	**50 W/m^2**	**60 W/m^2**
VAV w versus VAV w/o precooling	0.3	0	0.8	1.5	0.2
LLC w versus LLC w/o precooling	10.7	12.9	16.6	17.1	20.0
LLC w versus VAV w precooling	20.2	21.4	23.1	22.0	16.4
VAV w precool. versus conventional VAV	33.9	33.9	31.7	26.5	29.2
LLC w precool. versus conventional VAV	47.3	48.0	47.5	42.5	40.8

Table 6.11 – Electricity savings for a typical summer week in Miami as a function of internal loads

	Electricity savings for Miami (%)				
	20 W/m^2	**30 W/m^2**	**40 W/m^2**	**50 W/m^2**	**60 W/m^2**
VAV w versus VAV w/o precooling	0	0	0	0.6	0
LLC w versus LLC w/o precooling	0	0.8	0.9	2.2	7.3
LLC w versus VAV w precooling	9.9	15.0	16.0	17.5	18.7
VAV w precool. versus conventional VAV	33.5	33.2	30.7	27.8	29.6
LLC w precool. versus conventional VAV	40.1	43.2	41.9	40.4	42.8

Table 6.12 – Electricity savings for a typical summer week in Phoenix as a function of internal loads

	Electricity savings for Phoenix (%)				
	20 W/m^2	**30 W/m^2**	**40 W/m^2**	**50 W/m^2**	**60 W/m^2**
VAV w versus VAV w/o precooling	1.5	2.1	2.7	3.5	1.9
LLC w versus LLC w/o precooling	7.2	9.5	12.9	15.0	17.3
LLC w versus VAV w precooling	26.6	27.6	28.0	26.9	21.6
VAV w precool. versus conventional VAV	33.1	33.6	31.1	26.1	28.7
LLC w precool. versus conventional VAV	50.9	52.0	50.4	45.9	44.2

Table 6.13 – Electricity savings for cooling only (no transport energy) as a function of internal loads. Results are shown for LLCS with precooling relative to VAV system with precooling.

	Electricity savings for cooling (%)				
	20 W/m^2	**30 W/m^2**	**40 W/m^2**	**50 W/m^2**	**60 W/m^2**
Chicago	25.1	23.2	19.0	13.2	5.4
Houston	27.1	25.8	20.6	13.6	5.1
Las Vegas	16.4	11.1	7.5	-3.4	-7.9
Miami	22.4	21.6	13.5	5.4	-0.2
Phoenix	26.4	22.4	18.2	10.3	3.0

6.3.4 Effect of high latent loads

In addition to being used for dehumidification and ventilation, the DOAS can also deliver a certain amount of sensible cooling if the supply temperature is lower than the zone temperature. While comparing different DOAS configurations, it was shown that the reheat and higher supply temperatures of the DOAS air have a negative impact on the total electricity consumption. However, as the latent-to-sensible-load ratio in the zone increases, more DOAS air is required to remove latent loads. For a certain latent load, the DOAS airflow rates required for dehumidification will be sufficiently high to remove all sensible loads as well. The total energy consumption of the DOAS will in that case be higher than the VAV system since the DOAS operates with 100% outside air, while the VAV system mixes fresh and return air. This limiting case is identified for five climates by finding the latent loads for which all latent and sensible cooling is done by the DOAS.

The limiting case is presented in Table 6.14 (assuming standard sensible internal loads of 36 W/m^2) in terms of the maximum latent loads in $\text{kg}_{water}/\text{h}$, equivalent ACH of infiltration, and equivalent number of people. For example, in Chicago climate the latent load at which all latent and sensible loads would be removed solely by the DOAS is 0.4 $\text{kg}_{water}/\text{h}$. That latent load is equivalent to having 1 ACH infiltration rate based on the outside humidity for Chicago, or having 6 people in the room. (In Las Vegas climate, the equivalent ACH is infinite since the outside humidity is lower that the zone set point humidity). For comparison, Emmerich and Persily (2011) recorded the average measured airtightness of 228 buildings commercial building of 0.37 ACH at 4 Pa, and the recommended value by ASHRAE Standard 189.1 for the Design of High-Performance Green Buildings is 0.11 ACH at 4 P. This demonstrates that the limiting case would be difficult to achieve in a typical commercial building with a typical number of people per square meter of floor area and typical leakiness.

Table 6.14 – Latent loads for limiting case when all latent and sensible cooling are provided by DOAS

	$\mathbf{kg}_{water}/\mathbf{h}$	$\mathbf{ACH}_{infiltration}$	**No of people**
Chicago	0.4	1.0	6
Houston	0.5	1.5	7
Las Vegas	0.9	∞	12
Miami	0.5	1.5	7
Phoenix	1.0	4.5	14

6.3.5 Effect of transport power

It was observed by Krarti and Henze (2005) that the fan energy can have a significant influence on the predictive controller decisions and, therefore, should not be neglected. This assumption is tested by excluding the transport power from the objective function. The optimal cooling rates for both the VAV system and LLCS are found only by minimizing the energy for cooling, after which the transport energy is added to the total cost function.

The results in Figure 6.23 show that excluding the transport power from the objective function leads to a somewhat lower electricity consumption for cooling (sum of black and grey bars), but also in higher transport energy (pink bars), increasing the total electricity consumption. The increase for the VAV system ranges from less than 1% (Houston, Las Vegas and Miami, Minneapolis, Phoenix) to 150% for Helena. Similar trends are observed for the LLCS, but with differences being notably smaller. This is expected since the LLCS transport energy accounts for a smaller portion of the total energy. The example of cooling rates for both cases (including and excluding the transport energy from the objective function) is shown for the Helena climate for the VAV system (Figure 6.24) and the LLCS (Figure 6.25). Results confirm findings by Krarti and Henze (2005) that excluding the transport power from the objective function can indeed have a significant impact on the predictive controlled decisions. When the transport power was not included in the objective function, the cooling rates for both the VAV system and the LLCS were more spread out during the day, taking the advantage of lower part-load ratios and lower air temperatures. This resulted in lower electricity for cooling, but also in higher transport energy consumption due to a larger number of fans/pump operating hours.

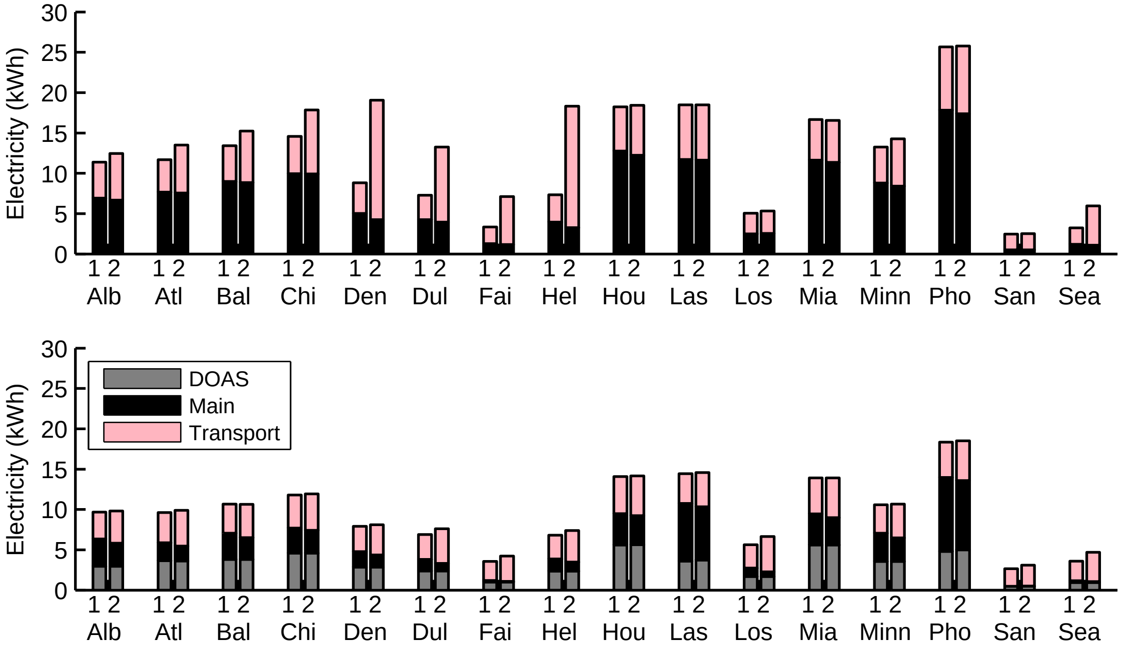

Figure 6.23 – Electricity consumption when transport power is included in objective function (1) and when transport power in not included in objective function (2). Top graph shows results for VAV system; bottom graph shows results for LLCS. Electricity for VAV/TABS heat pump is shown with black bars, for DOAS heat pump with gray bars, and for transport energy with pink bars.

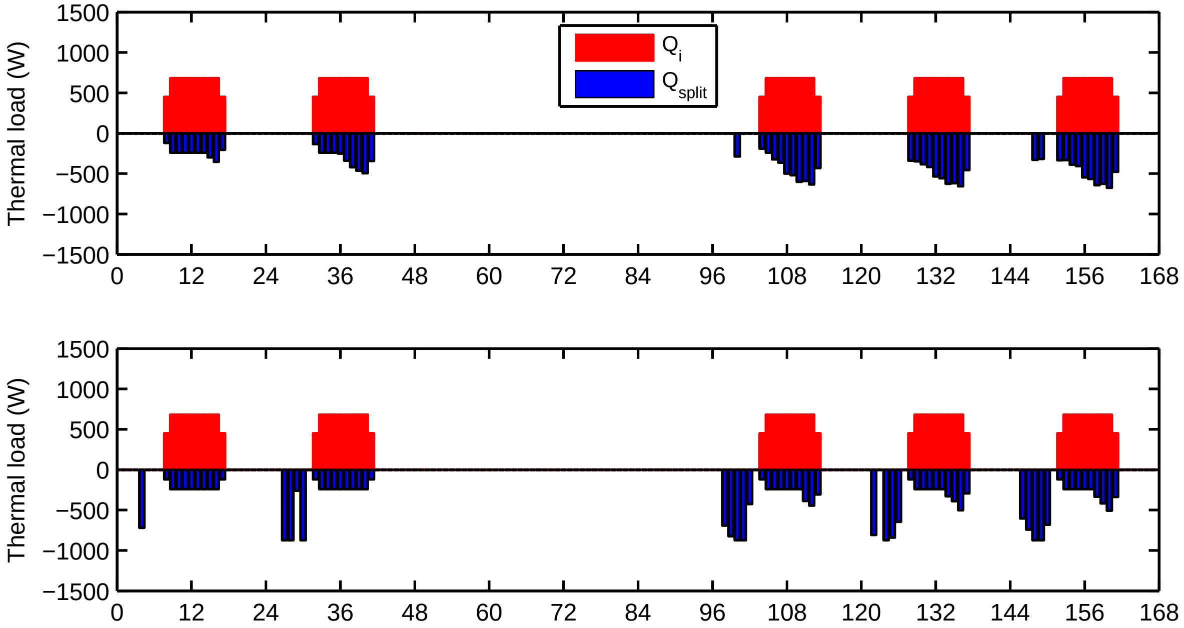

Figure 6.24 – Sensible internal gains (red) and VAV cooling rates (blue) for a typical summer week in Helena. Top graph is for case when transport power is included in objective function; bottom graph for case when transport power is not included in objective function.

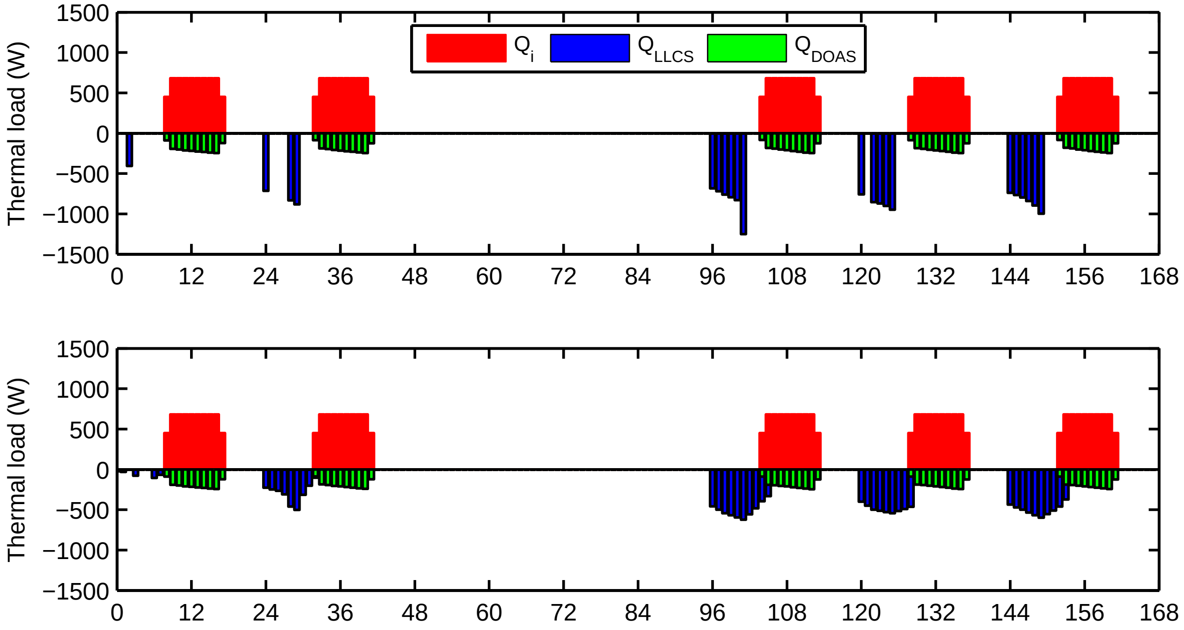

Figure 6.25 – Sensible internal gains (red), TABS cooling rates (blue) and DOAS cooling rates (green) for a typical summer week in Helena. Top graph is for case when transport power is included in objective function; bottom graph for case when transport power is not included in objective function.

6.3.6 Effect of return air flow

The return air flow in the DOAS and VAV system will be somewhat lower than the supply air flow due to building pressurization. Mumma (2010) showed that for an office building with a leakage rate of 5 $m^3/(hm^2)$ at 50 Pa, and with ASHRAE Standard 62.1 ventilation requirements, the ratio of the pressurization flow to the total ventilation flow rate should be around 0.7 to achieve adequate pressurization. Mumma (2010) also noted that the recovery wheel needs to work with balanced air flows, meaning that its efficiency will decrease depending on a return air flow reduction. To assess the impact of the reduced return airflow, the DOAS is tested for 50% of the return airflow relative to the supply.

The results in Figure 6.26 show that the LLCS with 50% return flow consumes between 5% (Chicago) and 11% (Phoenix) more electricity relative to the LLCS with 100% return flow. However, compared with the VAV system with precooling and to the conventional VAV system, the savings still range from 12–20% and 42–47% respectively. For comparison, the LLCS with 100% return air shows savings of 17–23% and 45–53% relative to the VAV system and the conventional VAV system respectively.

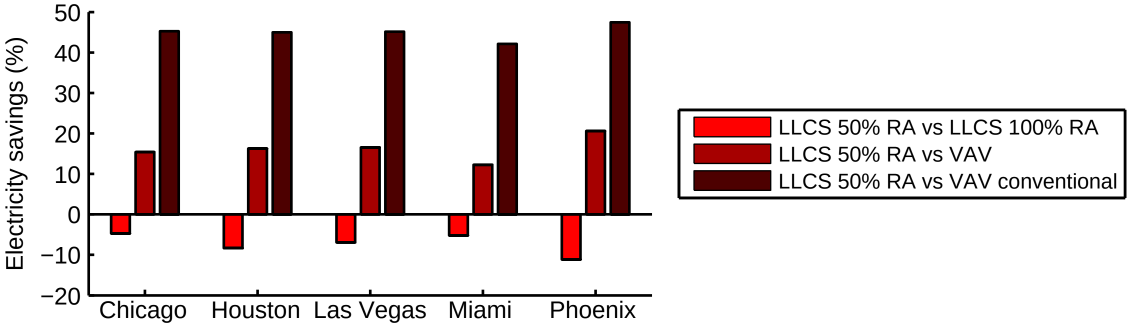

Figure 6.26 – Electricity savings for LLCS with 50% return air relative to LLCS with 100% return air (left bar), VAV system with precooling (middle bar) and conventional VAV system (no precooling and constant temperature of 22.5°C) (right bar)

6.4 Conclusion

This chapter presented the results of the LLCS performance analysis. The LLCS was compared against the split-system for sensible cooling only, and against the VAV system for cooling, dehumidification and ventilation. Several DOAS configurations were considered, evaluating their performance across 16 different climates. The first option was a variable-air-volume DOAS with the enthlapy recovery wheel, and the condenser cooled with the outside air; the second option was the configuration with parallel condensers, one placed in the supply stream, and the other placed in the return stream after the enthalpy wheel; the third option was also the configuration with parallel condensers, one placed in the supply stream, and the other placed outside; the fourth option was a variation of the basic DOAS, with the heat pipe placed before and after the cooling coil.

When the LLCS was compared against the split-system under conventional control the savings were 33% for Atlanta (using standard internal loads) and 36% for Phoenix (using high-performance loads) for a typical summer week. For this comparison the split system was running only during the occupied hours, and maintaining a constant 22°C. The LLCS utilized MPC allowing the building to be precooled during night and zone temperature to float between 19 and 25°C during the occupied hours. The temperature limits were chosen based on conditions Gayeski had during experimental measurements. When the same temperature limits and precooling were allowed for the split-system, the split system showed better performance than the LLCS, with 19% lower electricity consumption for Atlanta and 11% for Phoenix. The sensitivity analysis showed that the results are highly sensitive to a temperature limits for both systems, sensible loads, spacing between the pipes and also heat pump sizing.

When the LLCS was compared against the VAV system under a conventional control, the savings were up to 50% relative to the VAV system. The conventional control for the VAV assumed maintaining the constant 22.5°C during the occupied hours and no precooling, while the LLCS utilized MPC allowing the building to be precooled during night and zone temperature to float between 20 and 25°C during the occupied hours. The temperature limits were tightened to match ASHRAE comfort standards more closely. When allowing both the LLCS and VAV system to precool the building, and for a zone temperature to float between 20 and 25°C, the electricity savings of the LLCS were up to 23%. In addition to achieving electricity savings, the LLCS resulted in lower average daily temperatures than the VAV system and for humid climates, such as Miami, it also showed lower oscillations in zone's humidity. The LLCS performed worse than the VAV only in four climates where the cooling needs were the lowest. When analyzing the influence of precooling for both the VAV system and LLCS, precooling did not have notable effect on the VAV system electricity consumption. It did, however, have notable effect for the LLCS, especially for high internal loads, with differences in the electricity consumption up to 20%. Among different DOAS configurations, the results showed that the basic DOAS with the single condenser cooled with the outside air had the lowest energy consumption across different climates. The analysis of transport power optimization showed that excluding the transport power from the optimization function can significantly influence the decisions of MPC, and also notably increase the total electricity consumption. Finally, the analysis was done for very high latent loads, for which the whole sensible and latent cooling would be delivered by the DOAS, eliminating the need for the use of TABS. The results showed that such high latent loads are not very likely to occur in real office buildings, based on a measured average infiltration and typical number of people per m^2.

Chapter 7

Conclusion

The presented research significantly advances the knowledge about the simulation and performance of the novel energy efficient cooling system, termed the low-lift cooling system (LLCS). The specific LLCS configuration comprises thermally activated building surfaces (TABS) for sensible cooling, and a parallel dedicated outdoor air system (DOAS) for dehumidification and ventilation. The TABS and DOAS are served by a water-to-air and air-to-air heat pump respectively, with a variable speed drive for compressors, fans and pumps. The LLCS is operated under model predictive control (MPC) that optimizes its performance for the lowest energy consumption, although other objectives, such as price of electricity, are possible. The LLCS could also be used for heating, but this was not considered in this research.

This chapter describes the main contributions in the development of the computer algorithm for the LLCS analysis. It also gives the main conclusions about the LLCS potential based on the simulation results across 16 U.S. climates. Finally, it gives suggestions for the future work, mainly oriented toward the improvements required for a real-building implementation, and the analysis of technologies that could be complementary to the LLCS.

7.1 Original contributions

This research included the development of the computer algorithm for the LLCS analysis, but also the analysis of other cooling systems operated under MPC. It analyzed potential savings of the LLCS across different climates with and without dehumidification. Furthermore, it analyzed both the VAV and TABS system with and without MPC to determine savings achieved through the use of TABS alone, and savings achieved through the use of MPC. The advancements were also made in the analysis of a dehumidification strategy for the LLCS. The following achievements are considered important original contributions.

First, the MPC algorithm was developed by combining a simplified (inverse) building model, and results of the heat pump static optimization. The optimization was performed in MATLAB, and used to find the optimal cooling rates over 24 hours, based on a predicted weather and internal gain forecast. The objective was to minimize the daily cooling and transport energy consumption, while maintaining the comfort for the occupants. It was shown that the inverse building model (that predicts temperatures based on previous temperatures and current and previous loads) can be very successful in replacing the more complex TRNSYS model. This significantly reduced computational time, enabling a typical day to be optimized in 30-60 seconds on the Windows 7 platform operated on Intel i5, 2.3GHz processor. After the optimization, the optimal values were sent to the "virtual building," modeled in TRNSYS. Although slower than the inverse model, the TRNSYS model allowed the prediction of the building's response to optimal values with better accuracy. In a real building, the TRNSYS model would be replaced with the response from the building automation system (BAS). The MPC algorithm enables a systematic study of primary factors influencing the dynamic control and savings potential for an individual building. These factors include building thermal mass, TABS pipe spacing, temperature limits, heat pump performance, and equipment control. The algorithm is highly modular, enabling an easy future expansion, and sufficiently fast and robust for an implementation in a real building.

Second, using the heat pump model developed from first principles, the optimal heat pump performance was mapped as a function of the capacity and indoor and outdoor temperatures. The heat pump static optimization was decoupled from the building optimization, and the optimized data were used in MPC by fitting the polynomials to the heat pump optimization results. The adaptive grid search technique was used to find the optimal condenser and evaporator airflows and optimal subcooling at each operating point. The heat pump performance was also optimized for the economizer mode when the outside temperature was lower than the water temperature. It was shown that the airflow optimization has more significance than the subcooling optimization. It was also shown that the the heat pump designed for both sensible and latent cooling can under-perform when used for sensible cooling only, due to a low designed evaporator airflow compared to the optimal. The specific power at optimal fan speeds, as a function of capacity and indoor-outdoor temperature, was compared for R410A, propane, and ammonia-charged machines. Finally, the question of optimal sizing of a heat pump was explored, showing that modest oversizing can be desirable. These findings suggest that the relative sizing of heat pump components (compressor, compressor motor, condenser and evaporator), as well as the sizing of the heat pump itself relative to a design load, may benefit from a thorough reassessment of the current practice.

Third, five different DOAS configurations were considered for dehumidification and ventilation purposes. The basic variable-air-volume DOAS assumed the enthlapy recovery wheel, and the heat pump cooled with the outside air. Other options considered more complex configurations with the goal of improving the DOAS heat pump performance. The second option was a configuration with the condenser placed in the supply stream; the third option was a configuration with parallel condensers, one placed in the supply stream, and the other placed in the return stream after the enthalpy wheel; the fourth option was also a configuration with parallel condensers, one placed in the supply stream, and the other placed outside; the fifth option was a variation of the basic DOAS, with the heat pipe placed before and after the cooling coil. It was shown that the second option, a configuration with the condenser placed in the supply stream, was unable to reject all the condenser heat for high loads due to limited condenser airflows. It was also shown that among the remaining four options, the basic DOAS had the lowest energy consumption across different climates. This suggests that the DOAS air reheat can significantly increase the energy consumption, and that the LLCS system can benefit from the DOAS delivering a certain amount of sensible cooling.

Fourth, the LLCS was compared against the split-system for a sensible cooling of a typical office. The LLCS utilized MPC, and was allowed to precool the building at night with the zone temperature floating between 19 and 25°C during the occupied hours. The split system was running under conventional control, only during the occupied hours, and maintaining a constant 22°C. The LLCS showed savings of 33% for Atlanta (using standard internal loads) and 36% for Phoenix (using high-performance loads) for a typical summer week. Compared to the results of the experimental measurement by Gayeski et al. (2012), the simulations showed lower savings under the similar conditions since the heat pump evaporating temperatures were significantly lower in the measurements than the simulation, resulting in a lower average COP. Additional parametric studies were done to analyze the sensitivity of predicted savings. The sensitivity analysis showed that the results are highly sensitive to the temperature limits for both systems, sensible loads, spacing between the pipes and also heat pump sizing. Increasing the internal loads from 20 W/m^2 to 50 W/m^2 reduced the LLCS savings relative to the split-system from 53 to 25% for Atlanta and from 37 to 17% for Phoenix. When the same temperature limits and precooling were allowed for the split-system, the split-system showed a better performance than the LLCS, with 19% lower electricity consumption for Atlanta and 11% for Phoenix relative to the LLCS. However, some possible disadvantages of the split-system over the LLCS are noise, and the high velocities of cold air entering the room. Also, many grid operators offer utility rates that favor night operation, which can be better exploited with the LLCS since it allows for more efficient precooling of the building mass. On the other hand, the split-system might be a better solution for retrofits since it does not require a special floor assembly with embedded pipes.

Finally, the LLCS was analyzed against the VAV system for sensible cooling, ventilation and dehumidification. The analysis was done for a typical office, across 16 U.S. climates for a typical summer week and also for a 22-week spring and summer period. The LLCS was running under MPC, allowing the zone temperature to float between 20 and 25°C during the occupied hours. The VAV system was tested for both MPC and the conventional control, where the conventional control assumed maintaining the constant 22.5°C during the occupied hours and no precooling. LLCS electricity savings were up to 23% relative to the VAV system under the MPC, and up to 50% relative to the conventional VAV system. The savings were achieved through a lower transport energy and a higher average COP, the result of higher evaporating temperatures, lower condensing temperatures, and lower part-load ratios. The LLCS performed worse than the VAV only in the four climates with the lowest cooling needs. The LLCS savings were of the similar order of magnitude as the savings shown previously by Pacific Northwest National Laboratory (PNNL) study. The complete agreement between the result of the two studies was not expected since the PNNL study used somewhat different assumptions, modeling an ideal active thermal storage with water, using a different heat pump performance map, and also performing annual simulations. In addition to achieving electricity savings, the LLCS resulted in lower average daily temperatures than the VAV system. Moreover, for humid climates such as Miami, the LLCS also showed lower oscillations in zone humidity. When analyzing the influence of precooling for both the VAV system and LLCS, precooling did not have a notable effect on the VAV system electricity consumption. It did, however, have a notable effect for the LLCS, especially for high internal loads, with differences in the electricity consumption up to 20%. An additional analysis was performed to analyze the impact of neglecting the transport power for fan and pumps during the optimization. The analysis showed that excluding the transport power from the optimization function can significantly influence the decisions of MPC, and also notably increase the total electricity consumption. Finally, the limiting latent loads were defined, for which the whole sensible and latent cooling would be delivered by the DOAS, eliminating the need for the use of TABS. The latent load limit was defined as the equivalent air changes per hour of infiltration (based on outside absolute humidity for a specific climate), and equivalent number of people in the room that would cause such high latent loads. The results showed that these values are not very likely to occur in real office buildings, based on a measured average infiltration and typical number of people per m^2. The places where such high latent loads could occur are spaces with very large number of people per m^2, such as conference rooms or schools.

This research confirmed the high potential of the LLCS for electricity savings, shown previously by the PNNL study and Gayeski's experimental measurements. Savings would be even higher when replacing the VAV direct-expansion unit (air-to-air heat pump) used in this research with the water-to-air heat pump. While the direct-expansion units would be appropriate for the medium-size commercial buildings, large commercial buildings would typically use the water-to-air heat pump. The use of water-to-air heat pump for VAV requires an additional heat exchanger, and introduces the penalty associated with lower evaporating temperatures.

The cost estimate (Katipamula et al., 2010), performed for several building types, showed that office buildings represent ideal first candidates for the implementation of the novel system. Compared to a conventional system, an estimated incremental cost for a large office building was approximately 7.5 $\$/m^2$, while a medium office building even had a negative incremental cost of -6 $\$/m^2$. Furthermore, the same study showed that the potential customers were somewhat discouraged by the use of active thermal storage, which in general takes useful space and has shown to be challenging to control. It was demonstrated in this research that the use of building mass can be feasible and efficient method of avoiding active thermal storage. However, while the LLCS showed to effectively use building mass to shift cooling to the night period, the VAV system showed only marginal electricity savings from the use of precooling.

There are some additional considerations when planning for a LLCS implementation in real buildings. Relative to the VAV, the LLCS is more complex system that will require communication and combined efforts between an architect, engineer, owner and developers. Facility managers will also need to be trained for a novel and more complex control than a traditionally used VAV system control. Furthermore, while already wide-spreed in Europe, TABS with pipes embedded in concrete are relatively new technology in the U.S. and, therefore, require more skilled personnel for installation and maintenance. The use of TABS also makes the LLCS somewhat challenging to implement in existing buildings. Finally, for humid climates the humidity in the room needs to be carefully controlled to prevent condensation issues.

7.2 Future work

The future work will extend the analysis presented here by exploring improvements and complementary technologies to the LLCS. Also, the LLCS will be tested in a real building in Masdar City, UAE, to confirm the findings of this and previous LLCS studies, and also to additionally calibrate the simulation model.

1. Extension to multi-zone building. Before a real building implementation, it would be beneficial to

perform an analysis on a multi-zone building in addition to a single-zone analysis presented here. The analysis should also include solar gains, which were not considered in this research. While the TRNSYS model can easily be expanded to account for more zones, the challenging and important aspect will be building zoning, the optimization of critical zones, and coordination of control procedures between them.

2. Optimal split between cooling through the TABS and DOAS. The results suggest that the LLCS can benefit if a certain amount of cooling is delivered though the DOAS or some other direct cooling system. Moreover, in a case of unexpected internal load variations, a direct system could react more quickly than the inert TABS, improving the overall LLCS flexibility. The future work will address the DOAS system sizing and the optimal split between the direct cooling through DOAS and indirect cooling through TABS.

3. Implementation of a heat pump with an improved performance. A prototype of a chiller for a small temperature lift was recently developed by Wyssen et al. (2010). It was suggested based on the example of an office building that for the same operating conditions, the new prototype would result in an approximately 1.6 times higher COP relative to the existing chillers. This advancement in chiller industry could be a huge advantage for the LLCS, which on average operates at smaller lifts than the VAV system. It would, therefore, be useful to access the LLCS savings potential based on the improved heat pump performance.

4. Optimal heat pump sizing. The proper sizing of the heat pump also needs to be addressed. In this study the heat pump was sized for the conventional VAV system, and the LLCS heat pump was of the same size. However, the LLCS operates at lower cooling rates relative to the air system and could potentially use a heat pump of a smaller capacity. This downsizing would reduce the initial cost for the LLCS equipment, but would also result in somewhat higher operating cost since the heat pump would operate at higher part-load ratios, meaning lower efficiency. The algorithm presented in this research can be used to predict the annual cooling loads and to optimize the heat-pump size taking into account trade-offs between the capital and operating cost.

5. Analysis of desiccant dehumidification. An interesting dehumidification strategy that has not been analyzed in this work is desiccant dehumidification. After passing through a desiccant material, the air exits with a lower absolute humidity, but higher temperatures. Although it would result in an increased sensible load for TABS, this configuration would eliminate the need for a separate DOAS heat pump and could potentially significantly reduce DOAS energy. It would be especially interesting to analyze desiccant dehumidification for very hot climates where solar energy can be used for the dessicant regeneration.

6. Implementation of complementary technologies. Two complementary technologies that could additionally improve the performance of the LLCS and will be addressed in the future work are a cooling tower and a ground-source heat pump. In dry climates, the cooling tower can cool water to temperatures 8–10°C lower than air dry-bulb temperatures, resulting in lower condensing temperatures and an improved heat pump performance. The ground heat pumps are another way of reducing condensing temperatures by taking advantage of moderate ground temperatures. Ground-source heat pumps are becoming especially popular in China, the highest-growing construction market in the world. The importance of energy efficiency in China's building sector is expected to become even more important in

the coming decade. According to The World Bank, by the year 2015, half of the world's new building construction will take place in China, with the vast majority of these projects being very large projects such as commercial office buildings and large residential developments. In its most recent report, The World Bank (2013) proposes the strategic reforms that China should embed into a policy framework toward its vision for 2030. Among the six main proposed reforms, one is the green reform advocating improved energy efficiency that will help China reduce its dependence on imported oil and gas, and also reduce the gas emissions. With unchanged policies, China may have to import 75% of its oil (making it the world's largest oil importer) and 50 percent of its natural gas by 2030. Its annual per capita emissions have already exceeded the world average and are still rising rapidly. China's attempts to address these challenges will offer a great opportunity for the LLCS scaling on a new building market, and further performance improvements through the use of ground-source heat pumps.

7. Use of the LLCS for ancillary services. Another topic worth exploring is the use of a building with TABS for ancillary services to electricity grid operators. A building can provide the ancillary service by shredding its electricity consumption. The second largest consumer of electricity in commercial buildings (after lights) is cooling and ventilation equipment, especially electricity for heat pumps. This offers a great opportunity for load shredding by reducing, or completely turning off the heat pump operation for a certain period of time. The known TABS disadvantage of being inert here becomes an advantage over the VAV system. Because TABS have a large time constant, turning off the chiller will not result is such fast changes in internal temperature relative to a building with a VAV system. This suggests that a building with TABS could provide ancillary services for longer period of time than a building with VAV.

8. Analysis of chilled ceilings. Future work will analyze how the technology with exposed pipes, rather than embedded in the building mass, performs compared to the LLCS and conventional systems. Although it is not expected that the chilled ceilings will precool the building mass as effectively as TABS, this technology could be more practical for implementation in existing buildings, while still providing some of the benefits of the system with TABS.

9. Real building implementation. The LLCS is currently being implemented in a building in Masdar City. This real scale project will offer a platform to test the concepts presented in this research and also presented on a smaller scale in the experimental work by Gayeski. The LLCS implementation and testing in a real building will have important role in future simplification of MPC control and scaling of this novel technology.

Bibliography

Abadie, M. and N. Mendes (2006). Comparative analysis of response-factor and finite-volume based methods for predicting heat and moisture transfer through porous building materials. *Journal of Building Physics 30*(1), 7–37. 48, 49, 52, 55

ADL (2000). Energy efficient rooftop air conditioner: continuation application technical progress statement. Technical Report for Project DE-FC26-99FT40640, Arthur D. Little, Inc., Cambridge, MA. 44

Armstrong, P. R., W. Jiang, D. Winiarski, S. Katipamula, and L. K. Norford (2009). Efficient low-lift cooling with radiant distribution, thermal storage, and variable-speed chiller controls - Part 2: Annual use and energy savings. *HVAC&R Research 15*(2), 402–432. 23, 41, 80, 131

Armstrong, P. R., W. Jiang, D. Winiarski, S. Katipamula, L. K. Norford, and R. A. Willingham (2009). Efficient low-lift cooling with radiant distribution, thermal storage, and variable-speed chiller controls - Part 1: Component and subsystem models. *HVAC&R Research 15*(2), 366–401. 23, 24, 27, 42, 80, 109

Armstrong, P. R., S. B. Leeb, and L. K. Norford (2006). Control with building mass - Part 1: Thermal response model. *ASHRAE Transactions 112*(1), 449. 57

ASHRAE (2004). Standard 90.1-2004: Energy standard for buildings except low-rise residential buildings. 90

ASHRAE (2009). *ASHRAE Handbook-Fundamentals*. Atlanta, GA: American Society of Heating, Refrigerating and Air-conditioning Engineers, Inc. 40, 111

ASHRAE (2011). *ASHRAE Handbook-Applications*. Atlanta, GA: American Society of Heating, Refrigerating and Air-conditioning Engineers, Inc. 27

Blum, D. H. (2013). *Analysis and Characterization of Ancillary Service Demand Response Strategies for Variable Air Volume HVAC Systems*. MS thesis, Massachusetts Institute of Technology. 90, 91

Braun, J. E. (1990). Reducing energy costs and peak electrical demand through optimal control of building thermal storage. *ASHRAE Transactions 96*(2), 876–888. 77

Braun, J. E. (2007). Near-optimal control strategies for hybrid cooling plants. *HVAC&R Research 13*(4), 599–622. 28

Braun, J. E., S. A. Klein, W. A. Beckman, and J. W. Mitchell (1989). Methodologies for optimal control of chilled water systems without storage. *ASHRAE Transactions 95*(1), 652–662. 28

Braun, J. E., J. W. Mitchell, S. A. Klein, and W. A. Beckman (1987a). Models for variable-speed centrifugal chillers. *ASHRAE Transactions 93*(1), 1794–1813. 33

Braun, J. E., J. W. Mitchell, S. A. Klein, and W. A. Beckman (1987b). Performance and control characteristics of a large cooling system. *ASHRAE Transactions 93*(1), 1830–1852. 28

California Public Utilities Commission (2007). Decision 07-10-032. 19

Chaturvedi, N. and J. E. Braun (2002). An inverse grey-box model for transient buidling load predicitons. *HVAC&R Research 8*(1), 73–100. 78

Coad, W. J. (1999). Conditioning ventilation air for improved performance and air quality. *Heating/piping/air Conditioning Engineering 71*(9), 49–56. 95

Coffey, B., F. Haghighat, E. Morofsky, and E. Kutrowski (2010). A software framework for model predictive control with GenOpt. *Energy and Buildings 42*(7), 1084–1092. 79

Corbin, C. D., G. P. Henze, and P. May-Ostendorp (2012). A model predictive control optimization environment for real-time commercial building application. *Journal of Building Performance Simulation*, 1–16. 79

Crawley, D., L. Lawrie, C. Pedersen, R. Liesen, D. Fisher, R. Strand, R. Taylor, R. Winkelmann, W. Buhl, Y. Huang, and A. Erdem (1999). EnergyPlus, a new-generation building energy simulati on program. In *Proceedings of Building Simulation '99*, Volume 1, pp. 81–88. 48

Crawley, D., S. Pless, and P. Torcellini (2009). Getting to net zero. *ASHRAE Journal* (September). 19

DOE. Building energy data book. http://buildingsdatabook.eren.doe.gov/. Accessed April 2013. 19

Domanski, P. A. (1997). Minimizing throttling losses in the refrigeration cycle. In *Fuel and Energy Abstracts*, Volume 38, pp. 435–435. 40

EERE. DOE energy efficiency and renewable energy: Building energy software tools directory. http://apps1.eere.energy.gov/buildings/tools_directory. Accessed April 2013. 47

EIA (2012). *Annual energy review*. Energy Information Administration, U.S. Department of Energy. 19, 20, 21

EIA (2013). *Annual Energy Outlook 2013*. Energy Information Administration, U.S. Department of Energy. 21

Ellison, R. and F. Creswick (1978). A computer simulation of the steady-state performance of air-to-air heat pump. Technical Report Report No. ORNL/CON-16, Oak Ridge National Laboratory, USA. 27

Emmerich, S. J. and T. P. McDowell (2005). Initial evaluation of displacement ventilation and dedicated outdoor air systems of US commercial buildings. Technical Report NISTIR 7244, National Institute of Standards and Technology. 96

Emmerich, S. J. and A. Persily (2011). U.S. commercial building airtightness requirements and measurements. In *AIVC Conference Proceedings*, Brussels, Belgium, pp. 134 –137. 111, 136

Englander, S. L. and L. K. Norford (1992). Variable speed drives: improving energy consumption modeling and savings analysis techniques. In *Proceedings of American Council for an Energy-Efficient Economy*, Washington, DC. 91, 93

European Parliament (2002). Directive 2002/91/EC on the energy performance of buildings. http://eur-lex.europa.eu/LexUriServ/LexUriServ.do?uri=OJ:L:2003:001:0065:0071:EN:PDF. 19

European Parliament (2009). Press relese. http://www.europarl.europa.eu/sides/getDoc.do?pubRef=-//EP//TEXT+IM-PRESS+20090330IPR52892+0+DOC+XML+V0//EN&language=EN. Accessed April 2013. 19

Fischer, J. C. and C. W. Bayer (2003). Humidity control in school facilities. *Energy 30*, 35. 95

Fritzson, P., H. Olsson, and M. Otter (2013). Modelica - a unified object-oriented language for physical systems modeling (version 3.3). 48

Gatley, D. P. (2000). Dehumidification enhancements. *HVAC Engineering 72*(9), 27–35. 95, 96

Gayeski, N., T. Zakula, P. R. Armstrong, and L. K. Norford (2011). Empirical modeling of a rolling-piston compressor heat pump for predictive control in low-lift cooling. *ASHRAE Transaction 117*(2). 27, 81

Gayeski, N. T. (2010). *Predictive Pre-Cooling Control for Low-Lift Radiant Cooling using Building Thermal Mass*. Ph. D. thesis, Massachusetts Institute of Technology. 52, 53, 57, 86, 155

Gayeski, N. T., P. R. Armstrong, and L. K. Norford (2012). Predictive pre-cooling of thermo-active building systems with low-lift chillers. *HVAC&R Research 18*(5), 858–873. 23, 25, 81, 84, 109, 112, 143

Gwerder, M., J. Todtli, B. Lehmann, V. Dorer, W. Guntensperger, and F. Renggli (2009). Control of thermally activated building systems (TABS) in intermittent operation with pulse width modulation. *Applied Energy 86*(9), 1606–1616. 77

Gwerder, M., J. Todtli, B. Lehmann, F. Renggli, and V. Dorer (2007). Control of thermally activated building systems. In *Proceeding of International Conference Clima 2007 - REHVA World Congress*, Helsinki, Finland. 76

Henze, G. P. (2012). Personal communication in April 2012. 78

Henze, G. P., R. H. Dodier, and M. Krarti (1997). Development of a predictive optimal controller for thermal energy storage systems. *HVAC&R Research 3*(3), 233–264. 78, 81

Henze, G. P., C. Felsmann, D. E. Kalz, and S. Herkel (2008). Primary energy and comfort performance of ventilation assisted thermo-active building systems in continental climates. *Energy and Buildings 40*(2), 99–111. 77

Henze, G. P., A. R. Florita, M. J. Brandemuehl, C. Felsmann, and H. Cheng (2010). Advances in near-optimal control of passive building thermal storage. *Journal of Solar Energy Engineering 132*(2). 79, 118

Imanari, T., T. Omori, and K. Bogaki (1999). Thermal comfort and energy consumption of the radiant ceiling panel system.: Comparison with the conventional all-air system. *Energy and Buildings 30*(2), 167–175. 76

Jeong, J. W. and S. A. Mumma (2003). Impact of mixed convection on ceiling radiant cooling panel capacity. *HVAC&R Research 9*(3), 251–257. 96

Jeong, J. W., S. A. Mumma, and W. P. Bahnfleth (2003). Energy conservation benefits of a dedicated outdoor air system with parallel sensible cooling by ceiling radiant panels. *ASHRAE Transactions 109*(2), 627–636. 96

Jiang, W. and T. A. Reddy (2007). General methodology combining engineering optimization of primary HVAC&R plants with decision analysis methods - Part 1: Deterministic analysis. *HVAC&R Research 13*(1), 93–117. 28

Jiang, W., D. Winiarski, S. Katipamula, and P. R. Armstrong (2007). Cost-effective integration of efficient low-lift base load cooling equipment. Technical Report PNNL-17157, Pacific Northwest National Laboratory, Richland, WA. 23, 27, 80, 109

Karagiozis, A. and L. Gu (2004). The EMPD model. In *IEA/ECBCS Annex 41 Meeting*, Glasgow, Scotland. 51

Katipamula, S., P. R. Armstrong, W. Wang, N. Fernandez, H. Cho, W. Goetzler, J. Burgos, R. Radhakrishnan, and C. Ahlfeldt (2010). Cost-effective integration of efficient low-lift baseload cooling equipment. Technical Report FY08, Pacific Northwest National Laboratory, Richland, WA. 23, 81, 109, 131, 133, 144

Kerestecioglu, A., M. Swami, and A. Kamel (1990). Theoretical and computational investigation of simultaneous heat and moisture transfer in buildings: "effective penetration depth" theory. *ASHRAE Transactions 96*(1), 447–454. 49

Khattar, M., D. Shirey, and R. Raustad (2003). Cool & dry: Dual-path approach for a florida school. *ASHRAE Journal 45*(5), 58–60. 97

King, D. J. and R. A. J. Potter (1998). Description of a steady-state cooling plant model developed for use in evaluating optimal control of ice thermal energy storage systems. *ASHRAE Transactions 104*(1), 42–53. 28

Klein, S.A. et al. (2010). *TRNSYS 17: A Transient System Simulation Program, Solar Energy Laboratory*. Solar Energy Laboratory, University of Wisconsin, Madison, WI. 28, 48

Koschenz, M., B. Lehmann, and S. Holst (2000). Thermoaktive bauteilsysteme TABS - eine einfache und trotzdem genaue methode zur modellierung. Technical report, EMPA, Abteilung Energiesysteme/Haustechnik, Dubendorf and TRANSSOLAR, Energietechnik GmbH, Stuttgart. 50

Krarti, M., M. J. Brandemuehl, and G. P. Henze (1995). Evaluation of optimal control for ice storage systems. Final project report for ASHRAE 809-RP. 78

Krarti, M. and G. P. Henze (2005). Real-time predictive optimal control of active and passive building thermal storage inventory. Technical report, State Technology Advancement Collaborative. 78, 90, 136, 137

Kummert, M. (2007). *Using GenOpt with Trnsys 16 and Type 56*. ESRU University of Strathclyde. 83

Kummert, M. and P. Andre (2005). Simulation of a model-based optimal controller for heating systems under realistic hypotheses. In *Proceedings of the 9th International IBPSA Conference*, Montreal, Canada. 77

Lau, A., W. Beckman, and J. W. Mitchell (1985). Development of computer control routines for a large chilled water plant. *ASHRAE Transactions 91*(1), 780–791. 28

Lee, K. and J. E. Braun (2004). Development and application of an inverse building model for demand response in small commercial buildings. In *Proceedings of SimBuild*, pp. 1–12. 78

Lee, K. and J. E. Braun (2008a). Development of methods for determining demand-limiting setpoint trajectories in buildings using short-term measurements. *Building and Environment 43*(10), 1755–1768. 78

Lee, K. H. and J. E. Braun (2008b). Evaluation of methods for determining demand-limiting setpoint trajectories in buildings using short-term measurements. *Building and Environment 43*(10), 1769–1783. 78

Levins, W., C. Rice, and V. Baxter (1997). Modeled and measured effects of compressor downsizing in an existing air conditioner/heat pump in the cooling mode. *ASHRAE Transactions 192*(2), 22–33. 44

May-Ostendorp, P., G. P. Henze, C. D. Corbin, B. Rajagopalan, and C. Felsmann (2011). Model-predictive control of mixed-mode buildings with rule extraction. *Building and Environment 46*(2), 428–437. 79

Moore, T. (2008). Potential and limitations for hydronic radiant slabs using waterside free cooling and dedicated outside air systems. In *3rd National Conference of IBPSA-USA Proceedings*, Berkeley, California. 97

Mumma, S. (2002). Chilled ceilings in parallel with dedicated outdoor air systems: addressing the concerns of condensation, capacity, and cost. *ASHRAE Transactions 108*(2), 220–231. 96

Mumma, S. A. (2001). Overview of integrating dedicated outdoor air systems with parallel therminal systems. *ASHRAE Transactions 107*(1), 545–552. 95

Mumma, S. A. (2010). DOAS & building pressurization. *ASHRAE Journal 52*(8), 42. 96, 98, 139

Mumma, S. A. and J. Jeong (2005a). Field experience controlling a dedicated outdoor air system. *ASHRAE Transaction 111*(2), 433. 96

Mumma, S. A. and J. W. Jeong (2005b). Direct digital temperature, humidity, and condensate control for a dedicated outdoor air-ceiling radiant cooling panel system. *ASHRAE Transactions 111*(1), 547–558. 96

Mumma, S. A. and K. M. Shank (2001). Achieving dry outside air in an energy-efficient manner. *ASHRAE Transactions 107*(1), 553–561. 96

Niu, J., J. V. D. Kooi, and H. Rhee (1995). Energy saving possibilities with cooled-ceiling systems. *Energy and Buildings 23*(2), 147–158. 76, 97

NTDP (1994). Federal technology alert: liquid refrigerant pumping. New Technology Demonstration Program Report PNL-10232, Pacific Northwest National Laboratory, Richland, WA. 38

Olesen, B. W. (2007). Operation and control of thermally activated slab heating and cooling systems. In *6th International Conference on Indoor Air Quality, Ventilation & Energy Conservation in Buildings Proceedings*, pp. 28–31. 79

Olesen, B. W., K. Sommer, and B. Duchting (2002). Control of slab heating and cooling systems studied by dynamic computer simulations. *ASHRAE Transactions 108*(2), 698–707. 76

Rabl, A. and L. K. Norford (1991). Peak load reduction by preconditioning buildings at night. *International Journal of Energy Research 15*(9), 781–798. 76

Rice, K. (2006). DOE/ORNL heat pump design model, MarkVI version. http://www.ornl.gov/~wlj/hpdm/MarkVI.shtml. 27

Rode, C. and M. Woloszyn (2007). Whole-building hygrothermal modeling in IEA annex 41. *Thermal Performance of Exterior Envelopes of Whole Buildings, ASHRAE*, 1–15. 48

Seem, J. E. (1987). *Modeling of Heat Transfer in Buildings*. Ph. D. thesis, Wisconsin University, Madison (USA). 57, 78

Shank, K. M. and S. A. Mumma (2001). Selecting the supply air conditions for a dedicated outdoor air system working in parallel with distributed sensible cooling terminal equipment. *ASHRAE Transactions 107*(1), 562–571. 96, 98

Shapiro, M., A. Yager, and T. Ngan (1988). Test hut validation of a microcomputer predictive HVAC control. *ASHRAE Transactions 94*(1). 76

Sourbron, M., R. De Herdt, T. Van Reet, W. Van Passel, M. Baelmans, and L. Helsen (2009). Efficiently produced heat and cold is squandered by inappropriate control strategies: A case study. *Energy and Buildings 41*(10), 1091–1098. 77

Sourbron, M. and L. Helsen (2010). Thermally activated building systems in office buildings: impact of controller settings on energy performance and thermal comfort. In *Proceedings of the 8th International Conference on System Simulation in Buildings*, Liege, Belgium. 77

Spindler, H. C. and L. K. Norford (2009). Naturally ventilated and mixed-mode buildings - Part 2: Optimal control. *Building and Environment 44*(4), 750–761. 79

Spratt, D., G. Sadler, and K. Moodie (1989). Dynamic control - a case study. *ASHRAE Transactions 95*(2), 193–200. 76

Steeman, M., K. Goethals, J. Laverge, A. Janssens, and M. De Paepe (2009). On modelling moisture buffering when evaluating humidity controlled HVAC systems. In *11th International IBPSA Conference Proceedings*, Glasgow, Scotland. 49

Stephenson, D. and G. Mitalas (1971). Calculation of heat conduction transfer functions for muli-layer slabs. In *ASHRAE Annual Meeting*, Washington, DC. 48, 49

Stetiu, C. (1999). Energy and peak power savings potential of radiant cooling systems in US commercial buildings. *Energy and Buildings 30*(2), 127–138. 97

Stoecker, W. F., R. R. Crawford, S. Ikeda, W. H. Dolan, and D. J. Leverenz (1981). Reducing the peaks of internal air-conditioning loads by use of temperature swings. *ASHRAE Transactions 87*(2), 599–608. 76

The World Bank. Primary energy use. http://data.worldbank.org/indicator/. Accessed April 2013. 20

The World Bank (2013). *China 2030: Building a Modern, Harmonious, and Creative High-Income Society*. 146

Threlkeld, J. (1970). *Thermal Environmental Engineering*. Englewood Cliffs, NJ: Prentice-Hall. 88

Tian, Z. and J. A. Love (2009a). Application of radiant cooling in different climates: assessment of office buildings through simulation. In *11th International IBPSA Conference Proceedings*, Glasgow, Scotland, pp. 2220–2227. 97

Tian, Z. and J. A. Love (2009b). Energy performance optimization of radiant slab cooling using building simulation and field measurements. *Energy and Buildings 41*(3), 320–330. 98

Todtli, J., M. Gwerder, B. Lehmann, F. Renggli, and V. Dorer (2007). Integrated design of thermally activated building systems and of their control. In *Proceeding of International Conference Clima 2007 - REHVA World Congress*, Helsinki, Finland. 77

Verhelst, C., F. Logist, J. Van Impe, and L. Helsen (2012). Study of the optimal control problem formulation for modulating air-to-water heat pumps connected to a residential floor heating system. *Energy and Buildings 45*, 43–53. 27, 80

Wallin, J., H. Madani, and J. Claesson (2012). Run-around coil ventilation heat recovery system: A comparative study between different system configurations. *Applied Energy 90*(1), 258–265. 99

Wetter, M. (2008). *GenOpt Manual: Generic Optimization Program, Version 2.1. 0*. University of California (through Lawrence Berkeley National Laboratory), Berkeley. 82, 83

Wyssen, I., L. Gasser, B. Wellig, and M. Meier (2010). Chiller with small temperature lift for efficient building cooling. In *Proceeding of International Conference Clima 2010 - REHVA World Congress*, Antalya, Turkey. 23, 145

Zakula, T. (2010). *Heat Pump Simulation Model and Optimal Variable-Speed Control for a Wide Range of Cooling Conditions*. MS thesis, Massachusetts Institute of Technology. 28

Zakula, T., P. Armstrong, and L. Norford (2012). Optimal coordination of heat pump compressor and fan speeds and subcooling over a wide range of loads and conditions. *HVAC&R Research 18*(06), 1153–1167. 27, 87, 102

Zakula, T., N. T. Gayeski, P. R. Armstrong, and L. K. Norford (2011). Variable-speed heat pump model for a wide range of cooling conditions and loads. *HVAC&R Research 17*(5), 670–691. 27, 28, 103

Appendix A

Experimental room description

The room used for analyses in Chapter 6 is the room shown in Figure A.1 and with construction details given in Table A.1. This room was also used in experimental measurements by Gayeski (2010).

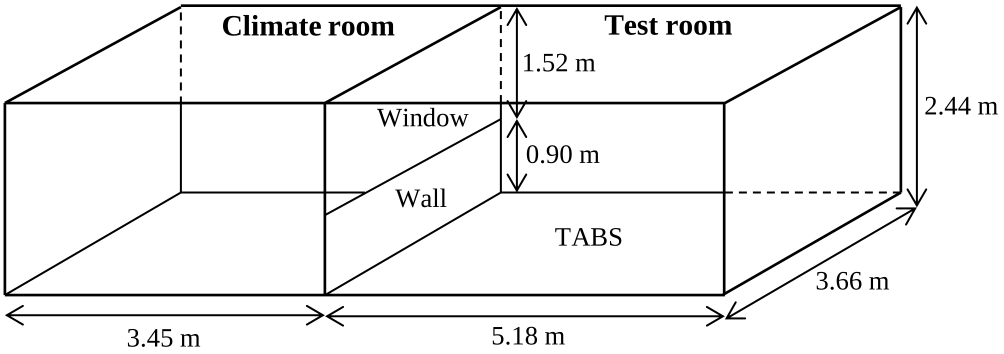

Figure A.1 – Experimental room setup

Table A.1 – Experimental room construction

	Construction layers (inside to outside)
A. Wall	0.016 m gypsum board 0.089 m air gap and 0.05 × 0.1 m stud wall 0.11 m polyisocyanurate foam R-30 0.016 m gypsum board
B. Ceiling	0.016 m gypsum board 0.140 m air gap and 0.05 × 0.15 m joists 0.11 m polyisocyanurate foam R-30 0.013 m plywood
C. Window	Three 1.12 × 1.17 m double pain windows separated by 0.09 m frames
D. Floor	Vinyl tile floor 0.025 m plywood 0.09 m floor joists with 0.076 m polyisocyanurate foam R-20 Existing concrete floor
E. TABS	Three layers of 0.044 m concrete pavers 0.00076 m aluminum 0.04 m plywood subfloor with 0.013 m PEX pipes (0.3 m center-to-center spacing) D. Floor

Appendix B

TRNSYS model parameters

The TRNSYS model parameters were all based on the experimental room parameters, except for the hygric response. Since the hygric response of the experimental room was not measured, parameters used in the TRNSYS buffer storage model were those given in the TRNSYS manual example for a typical office. The office is approximately of the same volume as the MIT's experimental room, with walls made of 12 mm gypsum and 100 mm mineral wool, and the floor and ceiling made of concrete. First 6 mm of gypsum are assumed to act as the surface layer, while the rest of the construction is considered the deep layer. Furthermore, for the comparison of the VAV system and low-lift cooling system, the TABS pipe spacing was reduced from 0.3 m to 0.15 m.

B.1 Construction parameters

Concrete

- k = 1 W/mK
- c = 900 J/kgK
- $\rho = 1850 kg/m^3$

Active layer

- Outside pipe diameter = 0.016 m
- Pipe wall thickness = 0.002 m
- Pipe center-to-center spacing = 0.3 m and 0.15 m

- k = 0.45 W/mK
- Water mass flow rate = 0.13 kg/s

Plywood

- k = 0.13 W/mK
- c = 2000 J/kgK
- $\rho = 550 kg/m^3$

Insulation

- k = 0.03 W/mK
- c = 1400 J/kgK
- $\rho = 40 kg/m^3$

Table B.1 – Construction parameters for TRNSYS model

	Construction layers (inside to outside)
A. Wall	0.016 m gypsum 0.089 m air gap 0.11 m insulation 0.016 m gypsum
B. Ceiling	0.016 m gypsum 0.140 m air gap 0.11 m insulation 0.013 m plywood
C. Window	4 m^2 double pain window with 10% framing-to-glazing ratio
D. Floor	0.025 m plywood 0.076 m insulation 0.008 m concrete
E. TABS	0.122 m concrete Active layer 0.01 m concrete 0.076 m insulation 0.008 m concrete

B.2 TRNSYS buffer storage model parameters

Surface buffer storage

- Gradient of sorptive isothermal line = 0.015 $\mathrm{kg}_{H_20}/\mathrm{kg}_{material}$/rel.humidity
- Mass = 270 $\mathrm{kg}_{material}$
- Exchange coefficient = 150 kg_{air}/h

Deep buffer storage

- Gradient of sorptive isothermal line = 1 $\mathrm{kg}_{H_20}/\mathrm{kg}_{material}$/rel.humidity
- Mass = 16 $\mathrm{kg}_{material}$
- Exchange coefficient = 50 kg_{air}/h

B.3 Other parameters

- Convective heat transfer coefficient was set as constant 5 $\mathrm{W/m^2K}$
- The internal loads that account for combined loads from people, light and equipment were modeled as 50% convective and 50% radiative.
- The air temperature outside the test room (T_{adj}) was set to constant 23°C, except in the climate room (climate room temperature changes depending on a climate).

Appendix C

Inverse model coefficients

Two inverse models that predict a thermal response of the experimental room were implemented for optimization. The inverse model A was appropriate when cooling is delivered only through TABS, while the inverse model B was used when cooling is delivered though both TABS and solely convective source of cooling. An additional inverse model was implemented for a hygric response of the experimental room.

C.1 Coefficients of inverse model A

The zone, operating, floor and water return temperature in the inverse model A were calculated using Equations C.1 – C.4, with coefficients of transfer functions shown in Tables C.1 and C.2. Internal sensible loads (Q_i) represent loads from people, lights and equipment.

$$T_z = \sum_{t=1}^{n} a_z^t T_z^t + \sum_{t=0}^{n} b_z^t T_{adj}^t + \sum_{t=0}^{n} c_z^t T_x^t + \sum_{t=0}^{n} d_z^t Q_{TABS}^t + \sum_{t=0}^{n} e_z^t {Q_i}^t \tag{C.1}$$

$$T_o = \sum_{t=1}^{n} a_o^t T_o^t + \sum_{t=0}^{n} b_o^t T_{adj}^t + \sum_{t=0}^{n} c_o^t T_x^t + \sum_{t=0}^{n} d_o^t Q_{TABS}^t + \sum_{t=0}^{n} e_o^t {Q_i}^t \tag{C.2}$$

$$T_{floor} = \sum_{t=1}^{n} a_f^t T_{floor}^t + \sum_{t=0}^{n} b_f^t T_{adj}^t + \sum_{t=0}^{n} c_f^t T_x^t + \sum_{t=0}^{n} d_f^t Q_{TABS}^t + \sum_{t=0}^{n} e_f^t {Q_i}^t \tag{C.3}$$

$$T_{w,return} = \sum_{t=1}^{n} a_w^t T_{w,return}^t + \sum_{t=0}^{n} b_w^t T_{floor}^t + \sum_{t=0}^{n} c_w^t Q_{TABS}^t \tag{C.4}$$

Table C.1 – Coefficients of inverse model A with 0.3 m pipe spacing

Term	$\mathbf{T}_z$	$\mathbf{T}_o$	$\mathbf{T}_{floor}$	$\mathbf{T}_{w,return}$
a(t-3)	-5.10×10^{-1}	-5.12×10^{-1}	1.03×10^{-1}	2.34×10^{-2}
a(t-2)	6.89×10^{-1}	6.94×10^{-1}	-8.97×10^{-1}	2.16×10^{-2}
a(t-1)	8.10×10^{-1}	8.07×10^{-1}	1.79×10^{0}	9.04×10^{-1}
b(t-3)	1.09×10^{-3}	1.12×10^{-3}	5.24×10^{-4}	6.14×10^{-2}
b(t-2)	1.09×10^{-3}	1.12×10^{-3}	5.23×10^{-4}	-2.29×10^{-1}
b(t-1)	1.09×10^{-3}	1.12×10^{-3}	5.23×10^{-4}	-7.27×10^{-1}
b(t)	1.09×10^{-3}	1.12×10^{-3}	5.23×10^{-4}	9.46×10^{-1}
c(t-3)	-9.22×10^{-3}	-8.89×10^{-3}	1.05×10^{-3}	2.59×10^{-4}
c(t-2)	-1.08×10^{-2}	-1.21×10^{-2}	4.18×10^{-4}	-1.80×10^{-5}
c(t-1)	1.35×10^{-2}	1.33×10^{-2}	1.47×10^{-3}	8.58×10^{-3}
c(t)	1.32×10^{-2}	1.44×10^{-2}	-1.26×10^{-4}	-9.30×10^{-3}
d(t-3)	-3.10×10^{-5}	-3.12×10^{-5}	-1.60×10^{-5}	
d(t-2)	-1.41×10^{-4}	-1.38×10^{-4}	-4.49×10^{-4}	
d(t-1)	-1.63×10^{-4}	-1.65×10^{-4}	2.05×10^{-3}	
d(t)	-4.28×10^{-5}	-4.32×10^{-5}	-1.80×10^{-3}	
e(t-3)	7.55×10^{-4}	4.06×10^{-4}	6.58×10^{-7}	
e(t-2)	-2.40×10^{-3}	-1.82×10^{-3}	1.40×10^{-5}	
e(t-1)	-5.41×10^{-4}	-2.49×10^{-4}	1.27×10^{-4}	
e(t)	2.59×10^{-3}	2.06×10^{-3}	4.11×10^{-5}	

Table C.2 – Coefficients of inverse model A with 0.15 m pipe spacing

Term	$\mathbf{T}_z$	$\mathbf{T}_o$	$\mathbf{T}_{floor}$	$\mathbf{T}_{w,return}$
a(t-3)	-5.10×10^{-1}	-5.11×10^{-1}	1.02×10^{-1}	4.30×10^{-2}
a(t-2)	6.87×10^{-1}	6.91×10^{-1}	-8.89×10^{-1}	3.96×10^{-2}
a(t-1)	8.12×10^{-1}	8.09×10^{-1}	1.78×10^{0}	8.09×10^{-1}
b(t-3)	1.09×10^{-3}	1.11×10^{-3}	5.54×10^{-4}	1.80×10^{-2}
b(t-2)	1.09×10^{-3}	1.11×10^{-3}	5.53×10^{-4}	-2.45×10^{-1}
b(t-1)	1.09×10^{-3}	1.11×10^{-3}	5.53×10^{-4}	-5.71×10^{-1}
b(t)	1.094×10^{-3}	1.11×10^{-3}	5.53×10^{-4}	9.06×10^{-1}
c(t-3)	-9.27×10^{-3}	-8.88×10^{-3}	1.18×10^{-3}	1.39×10^{-4}
c(t-2)	-1.07×10^{-2}	-1.21×10^{-2}	4.22×10^{-4}	-6.72×10^{-5}
c(t-1)	1.36×10^{-2}	1.33×10^{-2}	1.40×10^{-3}	2.52×10^{-3}
c(t)	1.31×10^{-2}	1.44×10^{-2}	-1.09×10^{-4}	-2.90×10^{-3}
d(t-3)	-3.11×10^{-5}	-3.11×10^{-5}	-1.47×10^{-5}	
d(t-2)	-1.43×10^{-4}	-1.39×10^{-4}	-4.43×10^{-4}	
d(t-1)	-1.61×10^{-4}	-1.64×10^{-4}	2.03×10^{-3}	
d(t)	-4.24×10^{-5}	-4.32×10^{-5}	-1.80×10^{-3}	
e(t-3)	7.56×10^{-4}	4.074×10^{-4}	5.19×10^{-6}	
e(t-2)	-2.40×10^{-3}	-1.82×10^{-3}	1.13×10^{-5}	
e(t-1)	-5.46×10^{-4}	-2.54×10^{-4}	1.30×10^{-4}	
e(t)	2.60×10^{-3}	2.065×10^{-3}	3.94×10^{-5}	

C.2 Coefficients of inverse model B

The zone, operating, floor and water return temperature in the inverse model B were calculated using Equations C.5 – C.8, with coefficients of transfer functions shown in Tables C.3 and C.4. Convective loads (Q$_{conv}$) are the sum of 50% loads from people, lights and equipment and 100% cooling rates from convective cooling system (e.g. a VAV system, DOAS, direct expansion system). Radiative loads (Q$_{rad}$) account for other 50% of loads from people, lights and equipment.

$$T_z = \sum_{t=1}^{n} a_z^t T_z^t + \sum_{t=0}^{n} b_z^t T_{adj}^t + \sum_{t=0}^{n} c_z^t T_x^t + \sum_{t=0}^{n} d_z^t Q_{TABS}^t + \sum_{t=0}^{n} e_z^t Q_{conv}^t + \sum_{t=0}^{n} f_z^t Q_{rad}^t \tag{C.5}$$

$$T_o = \sum_{t=1}^{n} a_o^t T_o^t + \sum_{t=0}^{n} b_o^t T_{adj}^t + \sum_{t=0}^{n} c_o^t T_x^t + \sum_{t=0}^{n} d_o^t Q_{TABS}^t + \sum_{t=0}^{n} e_o^t Q_{conv}^t + \sum_{t=0}^{n} f_o^t Q_{rad}^t \tag{C.6}$$

$$T_{floor} = \sum_{t=1}^{n} a_f^t T_{floor}^t + \sum_{t=0}^{n} b_f^t T_{adj}^t + \sum_{t=0}^{n} c_f^t T_x^t + \sum_{t=0}^{n} d_f^t Q_{TABS}^t + \sum_{t=0}^{n} e_f^t Q_{conv}^t + \sum_{t=0}^{n} f_f^t Q_{rad}^t \tag{C.7}$$

$$T_{w,return} = \sum_{t=1}^{n} a_w^t T_{w,return}^t + \sum_{t=0}^{n} b_w^t T_{floor}^t + \sum_{t=0}^{n} c_w^t Q_{TABS}^t \tag{C.8}$$

Table C.3 – Coefficients of inverse model B with 0.3 m pipe spacing

Term	$\mathbf{T}_z$	$\mathbf{T}_o$	$\mathbf{T}_{floor}$	$\mathbf{T}_{w,return}$
a(t-3)	-5.08×10^{-1}	-5.08×10^{-1}	8.53×10^{-2}	6.16×10^{-3}
a(t-2)	6.84×10^{-1}	6.84×10^{-1}	-8.56×10^{-1}	1.86×10^{-2}
a(t-1)	8.13×10^{-1}	8.13×10^{-1}	1.77×10^{0}	9.09×10^{-1}
b(t-3)	1.07×10^{-3}	1.10×10^{-3}	5.94×10^{-4}	8.17×10^{-2}
b(t-2)	1.07×10^{-3}	1.10×10^{-3}	5.95×10^{-4}	-1.79×10^{-1}
b(t-1)	1.07×10^{-3}	1.10×10^{-3}	5.95×10^{-4}	-8.02×10^{-1}
b(t)	1.07×10^{-3}	1.10×10^{-3}	5.95×10^{-4}	9.66×10^{-1}
c(t-3)	-9.31×10^{-3}	-8.85×10^{-3}	1.05×10^{-3}	1.11×10^{-4}
c(t-2)	-1.06×10^{-2}	-1.20×10^{-2}	4.04×10^{-4}	-2.69×10^{-5}
c(t-1)	1.34×10^{-2}	1.32×10^{-2}	1.42×10^{-3}	8.42×10^{-3}
c(t)	1.32×10^{-2}	1.44×10^{-2}	-1.01×10^{-4}	-9.16×10^{-3}
d(t-3)	-3.06×10^{-5}	-3.09×10^{-5}	-2.37×10^{-5}	
d(t-2)	-1.42×10^{-4}	-1.38×10^{-4}	-4.05×10^{-4}	
d(t-1)	-1.61×10^{-4}	-1.65×10^{-4}	2.01×10^{-3}	
d(t)	-4.41×10^{-5}	-4.43×10^{-5}	-1.80×10^{-3}	
e(t-3)	1.46×10^{-3}	7.59×10^{-4}	-4.72×10^{-6}	
e(t-2)	-3.54×10^{-3}	-2.42×10^{-3}	2.51×10^{-5}	
e(t-1)	-1.25×10^{-3}	-5.52×10^{-4}	1.28×10^{-4}	
e(t)	3.75×10^{-3}	2.62×10^{-3}	4.03×10^{-5}	
f(t-3)	4.08×10^{-5}	4.92×10^{-5}	4.03×10^{-6}	
f(t-2)	-1.24×10^{-3}	-1.20×10^{-3}	1.05×10^{-5}	
f(t-1)	1.49×10^{-4}	2.51×10^{-5}	1.28×10^{-4}	
f(t)	1.44×10^{-3}	1.51×10^{-3}	4.09×10^{-5}	

Table C.4 – Coefficients of inverse model B with 0.15 m pipe spacing

Term	$\mathbf{T}_z$	$\mathbf{T}_o$	$\mathbf{T}_{floor}$	$\mathbf{T}_{w,return}$
a(t-3)	-5.08×10^{-1}	-5.08×10^{-1}	1.24×10^{-1}	2.99×10^{-2}
a(t-2)	6.83×10^{-1}	6.84×10^{-1}	-9.49×10^{-1}	4.09×10^{-2}
a(t-1)	8.14×10^{-1}	8.13×10^{-1}	1.82×10^{0}	8.08×10^{-1}
b(t-3)	1.07×10^{-3}	1.09×10^{-3}	5.55×10^{-4}	-2.82×10^{-3}
b(t-2)	1.070×10^{-3}	1.09×10^{-3}	5.55×10^{-4}	-8.67×10^{-2}
b(t-1)	1.07×10^{-3}	1.09×10^{-3}	5.55×10^{-4}	-7.51×10^{-1}
b(t)	1.07×10^{-3}	1.09×10^{-3}	5.55×10^{-4}	9.62×10^{-1}
c(t-3)	-9.26×10^{-3}	-8.83×10^{-3}	8.97×10^{-4}	1.04×10^{-4}
c(t-2)	-1.066×10^{-2}	-1.21×10^{-2}	5.05×10^{-4}	5.93×10^{-5}
c(t-1)	1.35×10^{-2}	1.32×10^{-2}	1.29×10^{-3}	2.21×10^{-3}
c(t)	1.32×10^{-2}	1.44×10^{-2}	-4.03×10^{-5}	-2.74×10^{-3}
d(t-3)	-3.14×10^{-5}	-3.11×10^{-5}	-1.02×10^{-5}	
d(t-2)	-1.43×10^{-4}	-1.39×10^{-4}	-5.05×10^{-4}	
d(t-1)	-1.61×10^{-4}	-1.64×10^{-4}	2.10×10^{-3}	
d(t)	-4.24×10^{-5}	-4.36×10^{-5}	-1.80×10^{-3}	
e(t-3)	1.46×10^{-3}	7.60×10^{-4}	-6.34×10^{-6}	
e(t-2)	-3.54×10^{-3}	-2.42×10^{-3}	1.83×10^{-5}	
e(t-1)	-1.25×10^{-3}	-5.53×10^{-4}	1.26×10^{-4}	
e(t)	3.75×10^{-3}	2.62×10^{-3}	3.96×10^{-5}	
f(t-3)	4.11×10^{-5}	4.99×10^{-5}	5.37×10^{-6}	
f(t-2)	-1.24×10^{-3}	-1.20×10^{-3}	-9.38×10^{-7}	
f(t-1)	1.48×10^{-4}	2.57×10^{-5}	1.30×10^{-4}	
f(t)	1.44×10^{-3}	1.51×10^{-3}	3.93×10^{-5}	

C.3 Coefficients of inverse model for hygric response

The zone humidity was calculated using Equation C.9 and coefficients of transfer function shown in Table C.5. Internal latent loads (L_{gain}) represent loads from people, infiltration and ventilation.

$$w_z = \sum_{t=1}^{n} g^t w_z^t + \sum_{t=0}^{n} h^t L_{gain}^t \tag{C.9}$$

Table C.5 – Coefficients of inverse model for humidity response

Term	**w$_z$**
g(t-3)	-0.19
g(t-2)	-0.14
g(t-1)	1.33
h(t-3)	2.11
h(t-2)	-5.24
h(t-1)	-11.26
h(t)	16.50

Appendix D

Heat pump curve fits

Separate heat pump performance maps were created using static optimization algorithm for water-to-air heat pump (used by TABS), air-to-air heat pump that cools and dehumidifies the air to constant 12.5°C and saturated condition (used by the VAV system and DOAS) and air-to-air heat pump operating in sensible-cooling-only mode (used by the split-system). The heat pump static optimization data were approximated with polynomial curves to reduce computational time. An additional polynomial of the fourth order was fitted for the water-to-air heat pump operating in an economizer mode. When the outside temperature drops bellow the water supply temperature, the optimization function evaluates the COP for both the compressor-on (Equation D.1) and economizer mode (Equation D.2), and decides which one consumes less power.

For water-to-air heat pump:

$$\begin{aligned} COP = \big(&1.41\times10^{-1} - 3.61\times10^{-1}x_1 + 6.61\times10^{-3}x_2 - 6.04\times10^{-1}x_3 + 6.53\times10^{-1}x_1^2 + 9.47\times10^{-4}x_1\,x_2 \\ &- 3.27\times10^{-5}x_2^2 + 4.50\times10^{-4}x_1\,x_3 - 5.13\times10^{-6}x_2\,x_3 - 3.36\times10^{-5}x_3^2 - 3.15\times10^{-1}x_1^3 \\ &+ 6.04\times10^{-5}x_1\,x_2^2 + 1.85\times10^{-6}x_2^3 - 1.25\times10^{-4}x_1\,x_2\,x_3 - 4.47\times10^{-6}x_2^2\,x_3 + 4.93\times10^{-6}x_2\,x_3^2\big)^{-1} \end{aligned} \tag{D.1}$$

where $x_1 = Q_e / Q_{e,max}$, $x_2 = T_x$ and $x_3 = T_{w,return}$

For water-to-air heat pump operating in economizer mode:

$$\begin{aligned} COP =\,&60.94 - 191.99\,x_1 - 6.62\,x_2 - 1.3557\,x_3 - 195.89\,x_1^2 - 61.03\,x_1x_2 - 2.10\,x_2^2 + 36.02x_1\,x_3 + 2.61x_2\,x_3 \\ &- 3.54\times10^{-2}x_3^2 + 210.17\,x_1^3 + 11.21\,x_1^2\,x_2 - 3.01\,x_1\,x_2^2 - 0.09\,x_2^3 - 9.14\,x_1^2\,x_3 + 5.60\,x_1\,x_2\,x_3 \\ &+ 3.00\times10^{-1}x_2^2\,x_3 - 1.33x_1\,x_3^2 - 2.20\times10^{-1}x_2\,x_3^2 + 3.60\times10^{-3}x_3^3 + 13.58\,x_1^3\,x_2 + 1.10\,x_1^2\,x_2^2 \\ &- 3.55\times10^{-2}x_1\,x_2^3 - 2.65\times10^{-3}x_2^4 - 12.46x_1^3\,x_3 - 2.25\,x_1^2\,x_2\,x_3 + 9.56\times10^{-2}x_1\,x_2^2\,x_3 \\ &+ 7.56\times10^{-3}x_2^3\,x_3 + 1.02\,x_1^2\,x_3^2 - 8.07\times10^{-2}x_1\,x_2\,x_3^2 - 1.04\times10^{-2}x_2^2\,x_3^2 + 5.09\times10^{-3}x_2\,x_3^3 \end{aligned} \tag{D.2}$$

where $x_1 = Q_e / Q_{e,max}$, $x_2 = T_x$ and $x_3 = T_{w,return}$

For air-to-air heat pump with evaporator outlet air being at 12.5°C saturated state:

$$\begin{aligned} COP = \big(& 3.02\times10^{-3} - 3.23\times10^{-1}x_1 + 1.23\times10^{-2}x_2 + 4.76\times10^{-1}x_1^2 - 2.38\times10^{-4}x_1\,x_2 - 2.86\times10^{-4}x_2^2 \\ & -2.02\times10^{-1}x_1^3 + 6.77\times10^{-4}x_1^2\,x_2 + 3.71\times10^{-5}x_1\,x_2^2 + 4.25\times10^{-6}x_2^3\big)^{-1} \end{aligned} \tag{D.3}$$

where $x_1 = Q_e\,/\,Q_{e,max}$ and $x_2 = T_x$

For air-to-air heat pump operating only to remove sensible heat:

$$\begin{aligned} COP = & 12.84 + 11.12\,x_1 - 5.14\times10^{-1}x_2 - 1.82\times10^{-1}\,x_3 - 29.01\,x_1^2 + 1.56\times10^{-1}x_1\,x_2 + 1.99\times10^{-2}x_2^2 \\ & - 1.10\times10^{-1}x_1\,x_3 - 4.02\times10^{-2}x_2\,x_3 + 4.90\times10^{-2}x_3^2 + 14.13\,x_1^3 + 1.72\times10^{-1}x_1^2\,x_2 \\ & - 1.05\times10^{-2}\,x_1\,x_2^2 - 2.78\times10^{-4}x_2^3 - 1.21\times10^{-1}x_1^2\,x_3 + 2.24\times10^{-2}x_1\,x_2\,x_3 + 8.66\times10^{-4}x_2^2\,x_3 \\ & - 1.47\times10^{-2}x_1\,x_3^2 - 9.49\times10^{-4}x_2\,x_3^2 \end{aligned} \tag{D.4}$$

where $x_1 = Q_e\,/\,Q_{e,max}$, $x_2 = T_x$ and $x_3 = T_z$